JOURNAL OF PETROLOGY | VOLUME 52 | NUMBER 12 | PAGES 2293–2334 | 2011 | doi:10.1093/petrology/egr043

Correlation of Growth and Breakdown of Major and Accessory Minerals in Metapelites from Campolungo, Central Alps

RETO GIERÉ[1]*, DOUGLAS RUMBLE[2], DETLEF GÜNTHER[3], JAMES CONNOLLY[4] AND MARK J. CADDICK[4]

[1]INSTITUT FÜR GEOWISSENSCHAFTEN, ALBERT-LUDWIGS-UNIVERSITÄT, ALBERTSTRASSE 23B, D-79104 FREIBURG, GERMANY

[2]GEOPHYSICAL LABORATORY, CARNEGIE INSTITUTION OF WASHINGTON, 5251 BROAD BRANCH ROAD, WASHINGTON, DC 20015, USA

[3]DEPARTMENT OF INORGANIC CHEMISTRY, ETH-ZENTRUM, CH-8092 ZÜRICH, SWITZERLAND

[4]DEPARTMENT OF EARTH SCIENCES, ETH-ZENTRUM, CH-8092 ZÜRICH, SWITZERLAND

RECEIVED NOVEMBER 08, 2009; ACCEPTED AUGUST 31, 2011

Regionally metamorphosed pelitic rocks at Campolungo, Central Alps, contain biotite, muscovite, garnet, staurolite, kyanite, and quartz, and the minor minerals tourmaline, plagioclase, chlorite, rutile, and ilmenite. Accessory allanite, apatite, monazite, potassium feldspar, xenotime, and zircon have also been identified. The bulk-rock chemical composition is similar to that of shales, and indicates that the protolith was deposited in an active continental margin setting. Element distribution maps, electron microprobe analyses and in situ *UV–laser ablation inductively coupled plasma mass spectrometry data document a pronounced zoning in garnet and tourmaline porphyroblasts. Garnet displays a typical bell-shaped MnO zoning profile, with a maximum (~3 wt %) in the euhedral core. Cores are also rich in Y and heavy rare earth elements (HREE; e.g. 2150 ppm Y). In their broad rim, all garnet crystals display a subhedral annulus (10–15 μm wide), which is distinctly enriched in Ca, Sr, Y, and HREE, and which probably resulted from the breakdown of allanite (at ~550°C, ~6·4 kbar). Another characteristic feature of garnet rims is their sinusoidal chondrite-normalized REE pattern, which may represent partial equilibration with a light REE-enriched medium, probably generated through the breakdown of metamorphic allanite. Similar REE patterns are exhibited by a Ca-poor internal zone (inside the annulus), which may represent an earlier partial equilibration following the breakdown of detrital monazite. The large tourmaline crystals exhibit an optically visible three-stage zoning, which comprises: a euhedral core; a continuously zoned inner rim with a prominent euhedral Ca-rich annulus; and an outer rim, which also displays a distinct Ca-rich annulus and is separated from the inner rim by a sutured boundary. This boundary represents a marked chemical discontinuity, characterized for example by a decrease in the Zn concentration from 250 ppm (inner rim) to 20 ppm (outer rim). This change in Zn content reflects staurolite growth, which started after resorption of the inner rim of tourmaline and after a major deformation event. This chemical and textural discontinuity coincides with a marked shift in $\delta^{18}O$, which increases by ~0·8‰ across the inner rim–outer rim boundary. Our thermodynamic models suggest that resorption of the inner rim of tourmaline may be associated with small amounts (5–7 vol. %) of melt formed at ~650°C and 8·5 kbar. By using detailed textural observations, major and trace element zoning patterns and thermodynamic data, it was possible to model the metamorphic evolution of these rocks in considerable detail and, specifically, to correlate the growth and breakdown of major and accessory minerals.*

KEY WORDS: *garnet; tourmaline; accessory minerals; trace element zoning; oxygen isotope zoning*

*Corresponding author. Telephone: (+49) 761-203-6409. Fax: (+49) 761-203-6407. E-mail: giere@uni-freiburg.de

INTRODUCTION

The Campolungo area is a classic locality in the Swiss Alps (Fig. 1) and has long been famous for its wealth of mineral occurrences (Gübelin, 1939) and for its spectacularly exposed recumbent dolomite folds (Preiswerk, 1919). The area was the subject of geological studies as early as the late 18th and the early 19th centuries (Antognini & Bianconi, 2007), most notably by E. Pini, who first (in 1786) described the occurrence in dolomite of a mineral that was later named tremolite. Other key early studies were made by the French and Catalan geologists D. de Dolomieu and C. de Gimbernat. This region also offers an excellent opportunity to analyze the overprinting effects of the various deformation phases (e.g. Grujic & Mancktelow, 1996).

Despite numerous geological, structural and mineralogical studies in the Campolungo area, one conspicuous rock type (i.e. tourmaline-bearing pelitic schist) has not been investigated in detail. These schists are characterized by large euhedral tourmaline crystals, which form part of a typical amphibolite-grade metapelite mineral assemblage. These metapelites are highly suited for studying both trace element partitioning between various phases and trace element zoning patterns in refractory minerals. Moreover, these rocks give further insight into the metamorphic and structural evolution of the Lepontine Alps.

Chemical zoning in porphyroblasts is regarded as a record of changes in intensive parameters and of metamorphic reactions involved in porphyroblast crystallization. Consequently, compositional zoning in metamorphic minerals, especially garnet, provides key information for thermobarometric analysis and derivation of pressure–temperature–time (P–T–t) paths (e.g. Spear *et al.*, 1984). At high T, however, major element zoning may be modified considerably by intracrystalline diffusion (e.g. Florence & Spear, 1991; Caddick *et al.*, 2010). Trace element zoning, on the other hand, may be less susceptible to modification by diffusion and can be more pronounced than major element zoning (e.g. Hickmott & Shimizu, 1990; Hickmott & Spear, 1992; Lanzirotti, 1995; Spear & Kohn, 1996), suggesting that trace elements may be highly sensitive to chemical changes, kinetic effects, and changes in P and T. Several studies have demonstrated the usefulness of investigating both major and trace element zoning in garnet from metamorphic rocks (Chernoff & Carlson, 1999; Pyle & Spear, 1999; Skora *et al.*, 2006; Corrie & Kohn, 2008; Konrad-Schmolke *et al.*, 2008). Discontinuous changes in trace element concentration profiles across porphyroblasts have been interpreted as reflecting events that occurred simultaneously throughout the entire rock; for example, breakdown or formation of metamorphic phases or infiltration of trace element-enriched fluids or melts during porphyroblast growth (Hickmott *et al.*, 1987, 1992; Carlson, 1989; Hickmott & Spear, 1992; Schwandt *et al.*, 1996; Spear & Kohn, 1996; Konrad-Schmolke *et al.*, 2008). Other studies, however, argued that in some circumstances, these zoning features may record only local effects in the immediate vicinity of a porphyroblast, reflecting failure of some elements to achieve chemical equilibrium at hand-sample scale (Chernoff & Carlson, 1997, 1999). Here we explore these possibilities further by comparing trace and major element zoning in coexisting garnet and tourmaline porphyroblasts. We propose that the distinct compositional profiles across crystals of both phases may be correlated by using a combination of major and trace element data, textural information, accessory phases, and thermodynamic modeling.

GEOLOGICAL SETTING

Campolungo is located in the Lepontine area of the Central Alps (Fig. 1), an area that is dominated by recumbent folds, or nappes, which were formed during the Alpine orogeny. The Alps resulted from collision of the European and African continents, recording the closure of oceanic basins (Alpine Tethys) originally located between Europe and the Adriatic microplate (part of the Apulian plate, which originally belonged to Gondwana; see Stampfli, 2000; Stampfli *et al.*, 2001). The rocks described in this paper belong to the Simano nappe, paleogeographically a part of the European domain before the onset of tectonic convergence. The nappes derived from the European domain include the Gotthard 'Massif' as well as the Leventina, Lucomagno, Simano and Antigorio nappes (Fig. 1), which have been known as the Lower Penninic (or Sub-Penninic) nappes. The classic term 'Penninic', however, has been avoided in the recent literature (e.g. Schmid *et al.*, 2004; Berger *et al.*, 2005), because it included units derived from various paleogeographical domains (i.e. the European continental margin, the Valais ocean, the Briançonnais terrane, and the Piemont–Liguria ocean). The Pennine zone thus referred to the geological units that lie structurally south and above the Aar Massif and the Helvetic cover nappes, and north and below the Austroalpine domain, which represents the northern continental margin of the Adriatic microplate (Trümpy, 1980). The Valais and the Piemont–Liguria oceans belong to the Alpine Tethys, which separated the European and the Adriatic plates during the Upper Jurassic and parts of the Cretaceous and which is kinematically linked to the opening of the Atlantic Ocean (Stampfli, 2000). Structurally above the Simano nappe is the Adula nappe, a Paleogene tectonic mélange unit (Berger *et al.*, 2005). This 'tectonic accretion channel' (Engi *et al.*, 2001) is overlain by the Tambo and Suretta nappes, which belong to the Briançonnais terrane (Fig. 1), located paleogeographically between the Valais and the Piemont–Liguria oceans.

In the Lepontine Alps, the European domain consists of a pre-Triassic basement (shown in red in Fig. 1) and, at

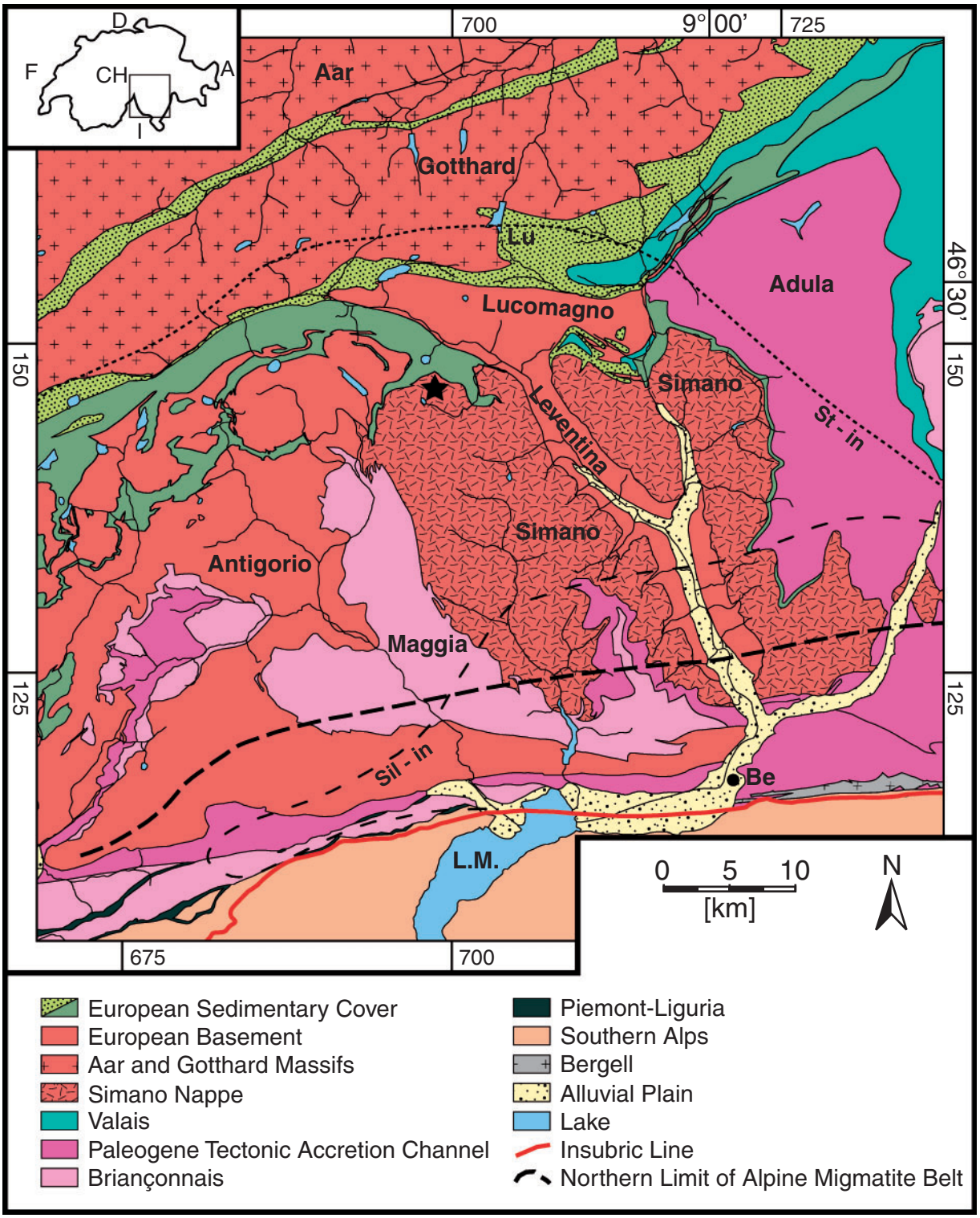

Fig. 1. Tectonic map of the Central Alps, simplified from the 1:500 000 Tectonic Map of Switzerland (Sektion Geologische Landesaufnahme, 2005), with additional information from the Tectonic and Petrographic Map of the Central Lepontine Alps (Berger & Mercolli, 2006) and from Berger *et al.* (2005). The northern limit of the Alpine migmatite belt (bold dashed line) is from Burri *et al.* (2005); staurolite and sillimanite zone boundaries (fine dashed lines labeled St-in and Sil-in, respectively) are from Frey & Ferreiro Mählmann (1999). Filled star marks Campolungo locality. Lu, Lukmanier pass; Be, Bellinzona; L.M., Lago Maggiore.

several localities, a metamorphosed sedimentary cover of Late Paleozoic and Early Mesozoic age. The basement, often referred to as crystalline basement, consists of orthogneisses (Lower and Upper Paleozoic metagranitoids), polymetamorphic paragneisses, some amphibolites, and rare ultramafic lenses. The orthogneisses of the Simano nappe are represented by the leucocratic two-mica Verzasca gneiss, derived from an Upper Carboniferous granite emplaced at the end of the Variscan orogeny, and by a biotite gneiss derived from an ~490 Ma granite protolith (Allègre *et al.*, 1974; Köppel *et al.*, 1981; Köppel, 1993).

The general stratigraphic sequence observed in the sedimentary cover of the European basement comprises, from bottom to top, the following units: (1) clastic metasedimentary rocks, which consist of pelitic to psammitic gneiss and more quartz-rich muscovite schist to gneiss with quartz pebbles (metaconglomerates?); the protoliths of these characteristic metasedimentary rocks were probably deposited during the Permian and possibly Carboniferous (Bossard, 1936; Grütter & Preiswerk, 1936); (2) white to buff-colored quartzite (also known as basal quartzite), which may contain considerable amounts of muscovite; (3) phlogopite-bearing dolomite, locally alternating with quartzitic layers; (4) various types of mainly dolomitic marble; (5) greywacke; (6) a characteristic metamarl, the so-called Quartenschiefer; (7) calcareous micaschists (also known as Bündnerschiefer) with a typical brownish gray color. These calcareous micaschists are attributed to the Jurassic, whereas units (2)–(6) are assigned to the Triassic. The general stratigraphic sequence observed in the European domain is similar to the Germanic Triassic and has been interpreted as the result of the marine transgression by the Tethys (see Berger *et al.*, 2005).

The Campolungo area was mapped in careful detail by Bianconi (1971), who also provided complete stratigraphic profiles as well as thorough petrographic descriptions of the various rock types. At Campolungo, the only metasedimentary unit missing from the stratigraphic sequence is the Upper Triassic Quartenschiefer. Variations in the Triassic lithostratigraphy are also known from other localities in the Simano nappe (Bianconi, 1971), pointing to slight variations in the depositional environment. Most prominent at Campolungo is stratigraphic unit (4): it is thick and consists of white and grey dolomites, ranging from laminated varieties to massive bands with saccharoidal texture, and from pure dolomite to tremolite-rich layers (for detailed descriptions, see Bianconi, 1971; Mercolli, 1982). Another prominent lithological unit at Campolungo is a thick sequence of psammitic to pelitic rocks (unit 1). It is these clastic metasedimentary rocks that are the topic of the present study, and all samples were collected from outcrops near Lago Leit (Swiss coordinates 698.650/146.600; see Fig. 1).

Structural investigations at Campolungo and in adjacent areas identified five phases of deformation during the Alpine orogeny (Grujic & Mancktelow, 1996; Maxelon & Mancktelow, 2005). The first phase, D_1, is related to the initial thrust and nappe development and is preserved as recumbent tight to isoclinal folds. These folds exhibit cores of pre-Triassic basement surrounded by metasedimentary cover rocks. The second deformation phase, D_2, refolded the nappe pile into major isoclinal folds characterized by a strong penetrative axial plane schistosity (S_2), which represents the dominant regional schistosity. The D_2 structural features were themselves overprinted during deformation phase D_3, which led to the development in mica-rich layers of a pronounced crenulation cleavage, S_3 (parallel to the axial planes of D_3 folds). The entire fold sequence was then folded (during D_4) about a large-scale F_4 synform with an east–west-trending axial plane. During the last phase (D_5), kink-like chevron folds developed locally (for details, see Grujic & Mancktelow, 1996).

PETROGRAPHIC FEATURES

Major and minor minerals

The regionally metamorphosed Campolungo pelites contain biotite, muscovite, garnet, staurolite, kyanite, and quartz, and the minor minerals tourmaline, plagioclase, chlorite, rutile, and ilmenite. Here, we describe the relationships between major and minor minerals observed in 42 thin sections, also detailing key microstructures (Figs 2 and 3). Combined with the deformation phases established on a regional scale (Grujic & Mancktelow, 1996), these thin-section observations allowed us to deduce relationships between mineral growth and deformation (summarized in Fig. 4).

A characteristic feature of these rocks is the presence of large (up to several centimeters long), euhedral black tourmaline crystals (Fig. 2a). In many cases, the tourmaline porphyroblasts have been broken into several pieces, which have then been pulled apart and in some orientations slightly displaced (Fig. 2a, long crystal in upper part of image). Staurolite can be observed in the space between the pulled-apart segments of tourmaline, clearly showing that it grew after tourmaline fracturing and extension (Fig. 2a, shorter crystal in lower part of the image). Such relationships between euhedral staurolite and tourmaline can be observed directly in the field. In plane-polarized light, tourmaline crystals exhibit an optically visible three-stage zoning consisting of a dark green core (C), an olive-colored inner rim (IR), and a lighter olive outer rim (OR; see Fig. 2b and c). Crystal cores may display lamellae that are characterized by different shades of green in transmitted light. Some tourmaline cores also contain small (~200–300 μm across) but distinct rounded tourmaline inclusions, which can be recognized by their slightly different

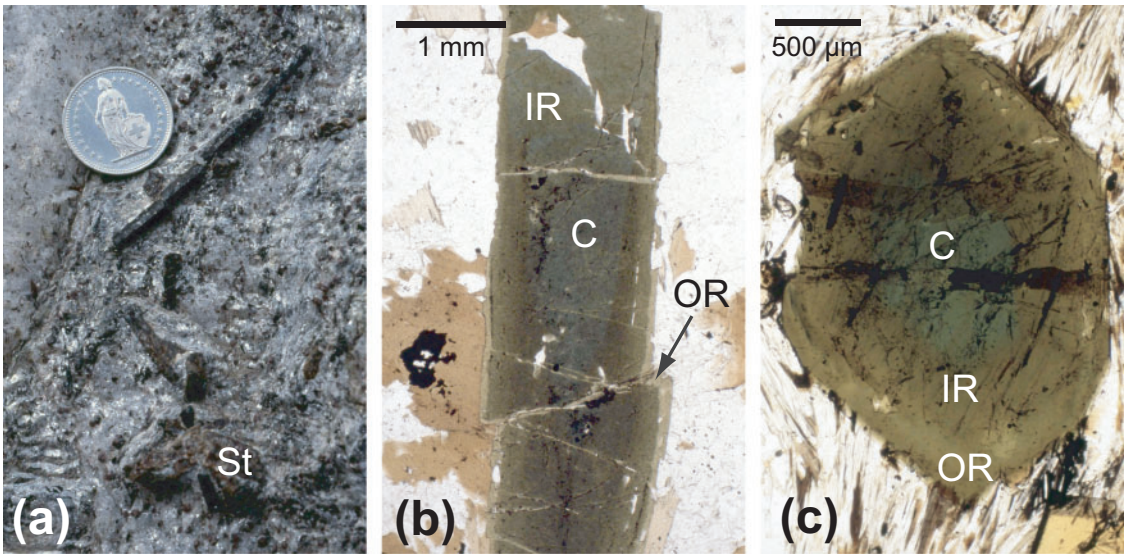

Fig. 2. Hand specimen (a) and photomicrographs (b, c; both plane-polarized light) of the metapelites from Campolungo. (a) Euhedral tourmaline crystals (black), which have been broken during deformation phase D_3. The staurolite crystal grown through the fracture of a tourmaline crystal should be noted (lower center). (b) Longitudinal section through a typical zoned tourmaline exhibiting a core, inner rim, and light-colored outer rim. The fractures across tourmaline are healed by light-colored tourmaline of the same composition as the light outer rim. (c) Typical cross-section through tourmaline. The crystal displays three zones of distinct color: dark olive core, olive inner rim, and light olive outer rim. Coin in (a) has a diameter of 2·6 cm. C, core; IR, inner rim; OR, outer rim; St, staurolite.

color and are interpreted to be of detrital origin. Textural relationships indicate that the IR probably crystallized pre- to syn-D_2, implying that the core was formed earlier, probably during D_1 (see Fig. 4). The IR of some large crystals contains abundant ilmenite inclusions, which exhibit a core of rutile and appear to be preferentially aligned. Detailed microscopic observations show that tourmaline was fractured before growth of the outer rim. The fractures and 'boudinaged' segments have been healed by light olive-colored tourmaline, which is continuous with, and has the same optical and chemical properties as, the OR (Fig. 2b). Therefore, the OR must have crystallized at the same time as the fracture fillings; that is, during or after the fracturing event, which, based on textural relationships, must be represented by D_3.

Staurolite crystals between pulled-apart tourmaline segments grew at the same time as the tourmaline OR (see Fig. 2a). This conclusion is further supported by the post-kinematic structure exhibited by many of the poikiloblastic crystals, which shows that they overgrew the crenulation produced during D_3 (Fig. 3a). However, close examination of large porphyroblasts (up to several millimeteres long) indicates that some staurolite had probably also grown during earlier stages of the metamorphic history (Fig. 4). This interpretation is based on the occurrence of inclusion trails in the core area (Fig. 3b), which are discordant to the folded foliation in other parts of the crystals or in the adjacent matrix. Moreover, muscovite, quartz and/or biotite occasionally occur together in what appears to be a pseudomorphic replacement of staurolite (Fig. 3c). The main schistosity wraps around these pseudomorphs, suggesting that the original mineral must have formed prior to D_2 (Fig. 4). Commonly, staurolite crystals exhibit highly irregular grain boundaries, whereby their rims are intimately intergrown with muscovite and quartz. In a few cases, staurolite exhibits embayed grain boundaries, which are filled by plagioclase. Staurolite contains inclusions of garnet, biotite, rutile, rutile rimmed by ilmenite (typically aligned along S_2), tourmaline, and quartz (Fig. 3b).

Garnet also forms prominent porphyroblasts, which range in size from 200 μm to several millimeters. Typically, crystals are fractured and show irregular grain boundaries, which may be overgrown by biotite or chlorite. Independent of size, garnet crystals exhibit distinct inclusion-rich cores, and inclusion-poor rims. Some of the larger crystals seem to consist of multiple cores surrounded by a single inclusion-poor rim. Smaller crystals occur frequently as aggregates or form garnet-rich bands. In many crystals a narrow, concentric band of tiny inclusions located between the core–rim boundary and the crystal edge can be recognized in cross-polarized light. Some garnet cores display an internal inclusion fabric (mostly defined by white micas and quartz) that clearly indicates syn-kinematic growth (Fig. 3d). In some cases, the main schistosity wraps around garnet crystals, which then also exhibit pressure shadows containing randomly oriented biotite. As crystal cores are so distinct and sometimes

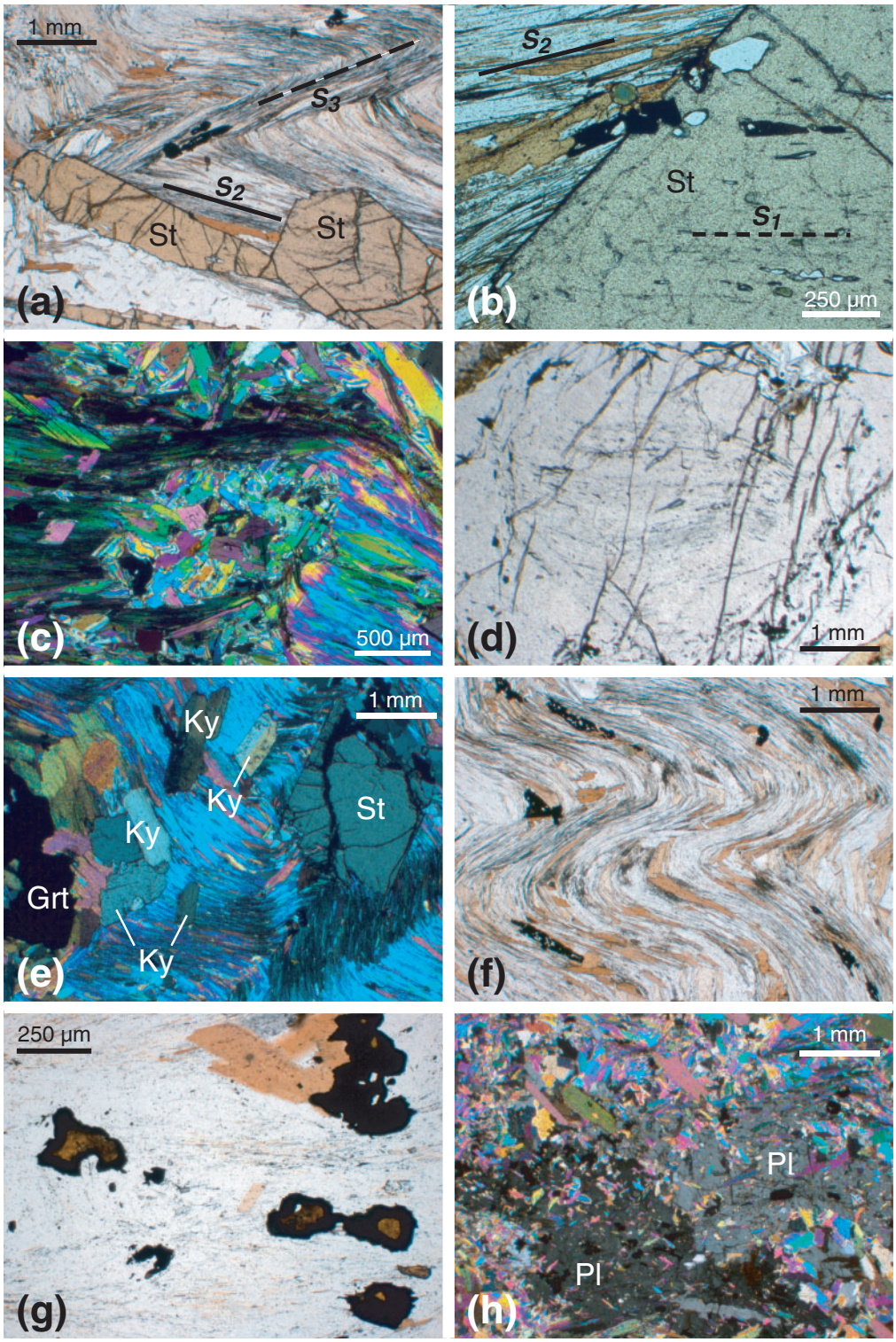

Fig. 3. Photomicrographs of the metapelites from Campolungo. (a) Large staurolite crystals overgrowing the main foliation (S_2) as well as the crenulation cleavage (S_3), which is delineated by muscovite and ilmenite. (b) Staurolite with inclusion trails aligned along S_1 in the core area overgrows S_2 (seen in the matrix). (c) Pseudomorph after staurolite(?) consisting of mostly muscovite. The S_2 schistosity is wrapped around the pseudomorph. (d) Garnet crystal with synkinematic, inclusion-rich core. (e) Kyanite in random orientation and staurolite overgrow the folded main schistosity, which is marked by muscovite (appearing in mostly blue colors). (f) Folded main schistosity marked by synkinematic muscovite, biotite, and ilmenite. (Note the late ilmenite crystals in fold hinge in left center of image.) (g) Matrix rutile surrounded by ilmenite. (h) Poikilitic plagioclase overgrowing muscovite and randomly oriented, late ilmenite. Images (c), (e) and (h) are photomicrographs taken with crossed polarizers; all other micrographs taken with plane-polarized light. Grt, garnet; Ky, kyanite; Pl, plagioclase; St, staurolite.

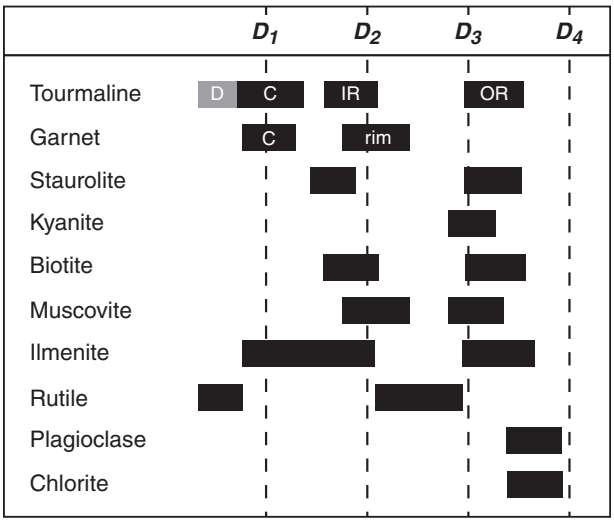

Fig. 4. Schematic representation of the relationship between mineral growth and deformation phases in the metapelites at Campolungo. D, detrital core; C, core; IR, inner rim; OR, outer rim. The deformation phases D_1, D_2, D_3, and D_4 are those of Grujic & Mancktelow (1996). D_2 produced the pervasive schistosity.

perfectly euhedral, we conclude that they grew during D_1, whereas the rims were formed in a separate growth event, before and during D_2. Garnet is also found as small (<700 μm across), euhedral inclusions in staurolite, as well as in the IR of large tourmaline crystals. In two instances, a tourmaline core was found to contain garnet inclusions (up to 1·2 mm across).

Kyanite is aligned in the folded S_2 foliation or, in some cases, overgrows this foliation (Fig. 3e). These textures suggest crystallization during or after D_3 (Fig. 4). In some cases, kyanite appears to be partially replaced by chlorite.

Muscovite is very abundant (~40–50 vol. %) and, along with the less abundant biotite (~15 vol. %), defines the main foliation (S_2), which was folded during D_3 (Fig. 3e and f). In addition, muscovite is frequently oriented parallel to the axial planes of the crenulation, defining a crenulation cleavage (S_3; Fig. 3a). Both micas are polygonized in the hinges of the crenulation, suggesting that they recrystallized after D_3. Moreover, large biotite crystals (several millimeters long) are also found as cross-micas (i.e. discordant to S_2) or replacing garnet.

Lath-shaped ilmenite crystals are typically aligned parallel to the main foliation (Fig. 3f). Ilmenite is also found in the hinges of the folded S_2 foliation, aligned parallel to S_3 (Fig. 3a), and is occasionally randomly distributed (Fig. 3h). It is a common inclusion in staurolite (Fig. 3b), tourmaline (core and IR), and in the outer parts of garnet. Ilmenite frequently forms rims around matrix rutile crystals (Fig. 3g), with the same texture occasionally present as inclusions in tourmaline (IR) and staurolite. In the interior parts of garnet, the Ti phase is typically rutile (see below).

Plagioclase occurs as large (several millimeters across), poikilitic porphyroblasts, which overgrow the crenulation, particularly in muscovite-rich layers. This microstructure (Fig. 3h) indicates that plagioclase is a late phase, formed after D_3 (Fig. 4). Plagioclase does not occur in all examined samples. It is notably absent from sample Leit 8, which is representative of most of the studied pelites and for which most mineral compositions are presented (see below).

Chlorite is a clearly retrograde phase (Fig. 4), which is always observed to overgrow the main foliation. It replaces garnet, biotite and occasionally staurolite and kyanite.

Our interpretation of the described relationship between mineral growth and deformation, as presented in Fig. 4, is largely consistent with that of Grujic & Mancktelow (1996). The major differences from this earlier work are that in the Campolungo metapelites most of the staurolite is clearly post-kinematic with respect to D_3 and there is no evidence for post-D_3 formation of garnet. Both of these porphyroblast types are commonly distinctly fractured, which we interpret as recording a D_4 phase that left few other clear traces.

Accessory minerals

Allanite, apatite, monazite, potassium feldspar, xenotime, and zircon are all present as accessory phases. The following description is based on observations made during a detailed scanning electron microscope (SEM) examination of thin sections Leit 1a and Leit 8g (Klapper, 2008). Additional information, obtained from the remaining 40 thin sections, was collected optically as well as with back-scattered electron (BSE) images and element distribution maps.

Only one allanite crystal has been found (section Leit 1a). It occurs together with monazite (Fig. 5a) as a small (3·5 μm across) inclusion in garnet, in an area that is also rich in xenotime inclusions.

Apatite is relatively abundant and occurs as primarily anhedral grains, which reach 1·8 mm in size. The larger grains are porphyroblastic, may contain quartz inclusions, and are fractured. Apatite crystals are frequently aligned in the S_2 foliation and have also been found as inclusions within the rims of garnet crystals.

Monazite ranges in size from 60 to 260 μm and is most abundant in biotite- and muscovite-rich domains. It is typically anhedral and frequently arranged in clusters of small grains (Fig. 5). Monazite also occurs as inclusions in garnet and staurolite. Occasionally, monazite encloses small grains of rutile or ilmenite.

Only two crystals of potassium feldspar have been found. They are ~1 mm across and associated with muscovite.

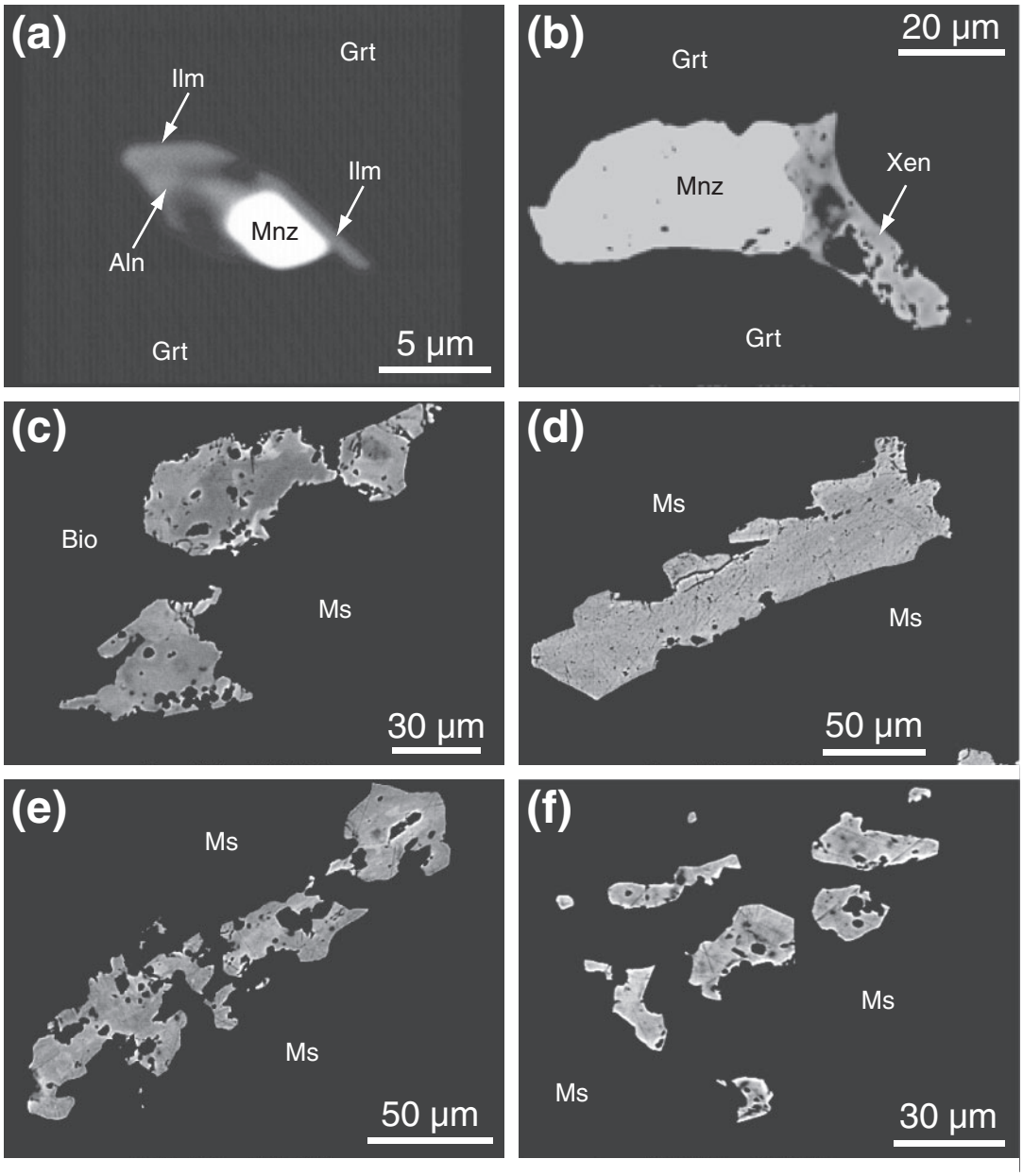

Fig. 5. BSE images showing inclusions of monazite in garnet (a, b) and the typical appearance of monazite in the matrix (c–f) of the metapelites at Campolungo. (a) sample Leit 1a; (b) monazite associated with xenotime; sample Leit 8c; (c) sample Leit 8c; (d–f) sample Leit 8g. Aln, allanite; Bio, biotite; Grt, garnet; Ilm, ilmenite; Mnz, monazite; Ms, muscovite; Xen, xenotime.

Xenotime is present exclusively as inclusions in garnet, where it is typically found as anhedral grains, which range in size from 10 to 35 μm across. Xenotime is occasionally found associated with monazite (Fig. 5b).

Zircon is typically subhedral to anhedral and occurs both in the matrix and as inclusions in garnet and tourmaline. Within garnet, zircon appears to be especially abundant in the center. The zircon grains are commonly 15–20 μm across, but may form subhedral crystals with dimensions up to 130 μm × 35 μm. Occasionally, zircon occurs as inclusion in ilmenite and kyanite.

BULK-ROCK COMPOSITION

The studied metapelites exhibit a considerable compositional variation with respect to both major and trace element contents (Table 1). The variation in most major element contents is reflected by the distinct mineralogical

Table 1: Bulk-rock composition of metapelites from Campolungo

	Method	D.L.	Leit 3	Leit 8		Leit 10		Leit 300	Leit 300a	Leit 400	Leit 400a	Leit 400b	Leit 900
				Average	SD	Average	SD						
n:			1	4		3		1	1	1	1	1	1
wt %													
SiO_2	XRF	0·01	53·9	53·2	0·3	61·0	0·4	55·6	56·1	61·8	50·4	50·5	60·5
TiO_2	XRF	0·001	1·13	1·10	0·01	0·93	0·01	1·06	1·07	0·83	1·16	1·17	0·89
Al_2O_3	XRF	0·01	24·6	24·1	0·1	20·6	0·2	23·8	23·6	20·0	26·1	25·6	20·5
Fe_2O_3[1]			2·27	1·4	0·2	0·82	0·06	1·14	1·16	0·77	1·32	1·45	0·72
FeO	COL	0·1	5·50	7·6	0·2	6·0	0·1	6·50	6·30	5·30	7·00	7·00	6·20
MnO	XRF	0·01	0·10	0·11	0·00	0·09	0·00	0·12	0·12	0·06	0·12	0·12	0·11
MgO	XRF	0·01	2·00	2·28	0·01	1·78	0·02	1·82	1·98	1·96	2·16	2·34	2·00
CaO	XRF	0·01	0·27	0·20	0·05	0·28	0·00	0·30	0·29	0·28	0·35	0·54	0·28
Na_2O	XRF	0·01	1·22	1·08	0·04	1·03	0·02	1·19	1·26	1·31	1·90	1·98	0·98
K_2O	XRF	0·01	4·82	4·61	0·05	3·96	0·06	4·53	4·69	4·05	4·78	4·38	4·30
P_2O_5	XRF	0·01	0·10	0·07	0·00	0·10	0·00	0·10	0·09	0·14	0·11	0·10	0·11
H_2O[2]			3·00	2·78	0·07	2·23	0·06	2·83	2·79	3·12	3·48	3·07	2·94
CO_2	CHM	0·04	0·26	0·3	0·1	0·34	0·09	0·44	0·26	0·07	0·15	0·26	0·15
Total			99·2	98·9		99·2		99·4	99·7	99·7	99·0	98·5	99·7
Fe_2O_3 (tot)	XRF	0·01	8·38	9·90	0·08	7·53	0·09	8·36	8·16	6·66	9·10	9·23	7·61
LOI			2·65	2·2	0·1	1·90	0·05	2·55	2·35	2·60	2·85	2·55	2·40
ppm													
Li	ICP_{90}	10	16	24	10	15	3	17	22	39	39	57	20
Be	MS_4	0·5	6·6	5·6	0·1	4·0	0·2	5·3	5·1	3·9	5·2	6·3	3·7
B	ICP_{90}	10	22	39	7	25	8	44	57	47	97	203	15
S	CHM	100	400	125	50	333	231	200	200	300	400	200	200
Sc	ICP_{90}	5	19	19	1	16·7	0·6	18	17	16	20	19	16
V	MS_4	2	146	137	5	112	6	137	133	124	145	141	117
Cr	XRF	5	208	274	35	376	58	319	285	178	245	231	253
Co	XRF	2	50	54	2	55	2	54	45	61	43	38	61
Ni	XRF	2	37	53	3	46	4	44	56	37	58	54	44
Cu	XRF	2	20	20·0	0·0	10·0	0·0	30	10	20	10	10	20
Zn	XRF	2	139	145	3	134	4	132	123	79	120	101	100
Ga	XRF	3	32	31	2	26·7	0·6	29	30	26	35	34	26
As	XRF	3	5	14	1	9	1	7	7	5	5	5	6
Se	XRF	3	<3	<3		<3		<3	<3	<3	<3	<3	<3
Rb	XRF	2	201	206	5	162	7	181	188	184	209	201	173
Sr	XRF	2	103	92	1	83	4	104	102	87	124	135	80
Y	XRF	2	42	51	1	49	2	48	49	33	49	45	42
Zr	XRF	2	231	232	1	232	8	219	206	150	198	215	174
Nb	XRF	2	20	22	1	20	2	22	19	18	22	21	19
Mo	XRF	2	2	2·2	0·5	3·3	0·6	3	2	2	3	2	3
Ag	MS_4	0·2	0·4	0·4	0·2	0·27	0·06	0·5	<0·2	<0·2	<0·2	<0·2	<0·2
Cd	MS_4	10	<10	<10		10	0	<10	<10	<10	<10	<10	<10
Sn	XRF	5	6	5	0	5	0	6	6	5	6	5	6
Sb	XRF	3	<3	4	2	<3		<3	<3	<3	<3	<3	<3
Ba	XRF	20	685	693	22	616	50	655	616	565	703	659	626
La	MS_{90}	0·1	71·6	73	6	61	1	70·6	74·1	56·6	73·1	73·2	58·5

(continued)

Table 1: Continued

	Method	D.L.	Leit 3	Leit 8		Leit 10		Leit 300	Leit 300a	Leit 400	Leit 400a	Leit 400b	Leit 900
				Average	SD	Average	SD						
n:			1	4		3		1	1	1	1	1	1
Ce	MS_{90}	0·1	138·0	140	12	116	3	135·0	142·0	106·0	136·0	138·0	112·0
Pr	MS_{90}	0·2	13·9	14	1	11·6	0·2	13·2	13·9	10·6	13·7	13·7	11·2
Nd	MS_{90}	0·1	58·0	58	4	48	2	54·9	57·4	44·0	58·2	56·6	46·9
Sm	MS_{90}	0·1	10·7	10·7	0·7	9·0	0·2	10·4	10·8	8·6	11·3	10·8	8·9
Eu	MS_{90}	0·05	2·11	2·1	0·2	1·77	0·02	2·00	2·00	1·62	2·15	2·15	1·78
Gd	MS_{90}	0·1	9·2	9·0	0·7	8·1	0·2	8·7	9·2	7·2	9·3	9·6	8·2
Tb	MS_{90}	0·1	1·2	1·23	0·05	1·20	0·00	1·2	1·2	1·0	1·3	1·4	1·2
Dy	MS_{90}	0·1	7·3	7·5	0·1	7·9	0·4	7·2	7·6	5·9	7·9	9·0	7·3
Ho	MS_{90}	0·05	1·25	1·35	0·06	1·5	0·1	1·37	1·32	1·11	1·45	1·61	1·35
Er	MS_{90}	0·1	4·2	4·5	0·1	5·0	0·4	3·3	4·4	3·8	4·8	5·1	4·4
Tm	MS_{90}	0·1	0·5	0·55	0·06	0·57	0·06	0·5	0·5	0·5	0·6	0·6	0·6
Yb	MS_{90}	0·1	3·5	3·8	0·1	4·2	0·2	3·7	3·4	3·2	4·1	4·2	3·4
Lu	MS_{90}	0·05	0·49	0·50	0·02	0·54	0·03	0·49	0·46	0·45	0·55	0·61	0·47
Ta	XRF	5	<5	<5		5	0	<5	<5	6·00	<5	5·00	<5
Pb	XRF	2	30	25	6	30·0	0·0	30	30	30	50	50	20
Bi	XRF	3	6	5·3	0·5	6	2	3	6	5	5	7	5
Th	MS_{90}	0·1	26·6	26	2	22·2	0·6	23·4	24·8	19·3	26·3	25·4	21·8
U	MS_{90}	0·1	4·2	4·2	0·2	3·67	0·06	3·7	3·9	3·1	3·9	3·8	3·4
Eu/Eu*			0·65	0·64		0·63		0·64	0·61	0·62	0·64	0·64	0·63
$(La/Yb)_{CN}$			14·2	13·2		10·1		13·2	15·1	12·2	12·3	12·1	11·9

Abbreviations for methods: XRF, X-ray fluorescence spectrometry (borate-fused glass beads for major elements; pressed powder pellets for trace elements); ICP_{90}, inductively coupled plasma optical emission spectrometry, preceded by Na_2O_2 fusion; MS_{90}, inductively coupled plasma mass spectroscopy, preceded by Na_2O_2 fusion; MS_4, inductively coupled plasma mass spectroscopy, preceded by $LiBO_2$ fusion; CHM, LECO infrared spectroscopy; COL, colorimetry, preceded by digestion in a multi-acid mixture ($HF–HNO_3–H_3BO_3$) in a non-oxidizing environment. D.L., detection limit of the method. LOI, loss on ignition.
[1]Calculated from the contents of total Fe_2O_3 (XRF) and FeO (COL).
[2]Calculated from LOI, FeO and CO_2 data.

banding, characterized by quartz-rich and garnet-staurolite-mica-rich layers. Despite the observed compositional variation, the contents of most major and trace elements in the studied metapelites are typical for shales. All samples, for example, plot within the shale field in Herron's (1988) chemical classification diagram for terrigenous clastic rocks (given as Fig. 1S in the electronic supplementary material, available for downloading at http://www.petrology.oxfordjournals.org). Enrichments or depletions relative to the North American Shale Composite (NASC; data from Condie, 1993) are less than a factor of two for most elements (Fig. 6; Cr enrichment is most probably due to the Cr-steel mill used for sample preparation). A notable exception is the pronounced depletion in Ca relative to NASC. A distinctly low CaO content is characteristic for the studied rocks (average CaO content 0·31 ±0·09 wt %, $n = 9$). In comparison with the shale data of Turekian & Wedepohl (1961), the Campolungo metapelites are also markedly depleted in S (200–300 ppm vs 2400 ppm). High field strength elements are relatively abundant in all analyzed samples, including Ti ($TiO_2 = 1·0 \pm 0·1$ wt %; average of nine samples), Y (45 ± 6 ppm), Zr (210 ± 30 ppm), Nb (20 ± 1 ppm), and Th (24 ± 2 ppm).

The Li content of the Campolungo metasedimentary rocks shows considerable variability (15–57 ppm). It overlaps with the concentration range reported for various shales (28–109 ppm), and the average value of 28 ± 14 ppm is similar to the estimated average Li content of the upper continental crust (McLennan, 2001; Teng *et al.*, 2004).

The B concentrations (average 61 ±58 ppm; range 22–203 ppm) are typical for argillaceous sedimentary rocks, which on average host ~100 ppm B (Goldschmidt & Peters, 1932*a*, 1932*b*; Harder, 1970), but may contain up to 310 ppm (Leeman & Sisson, 1996).

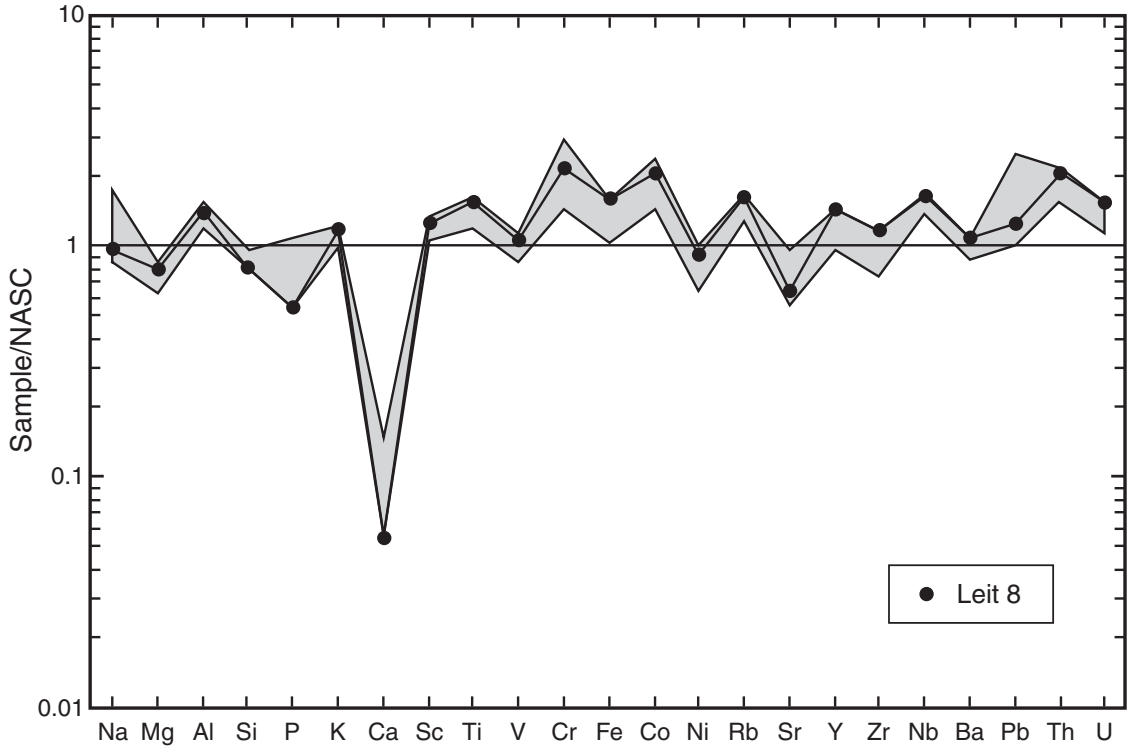

Fig. 6. Bulk-rock composition of the Campolungo metapelites plotted in an NASC-normalized multi-element diagram. Continuous black line with dots represents sample Leit 8; shaded area shows the range in composition for all studied Campolungo metapelites. NASC, North American Shale Composite; data from Condie (1993).

The chondrite-normalized rare earth element (REE) patterns (Fig. 7) exhibit a distinct light REE (LREE) enrichment, with an average $(La/Yb)_{CN}$ of ~13, which is approximately twice the enrichment observed for NASC. The Campolungo metapelites further display a marked negative Eu anomaly (average $Eu/Eu^* = 0{\cdot}63 \pm 0{\cdot}01$), which is very similar to those of shales ($Eu/Eu^* = 0{\cdot}68$ for NASC) and upper continental crust ($Eu/Eu^* = 0{\cdot}61$, Taylor & McLennan, 1985).

MINERAL COMPOSITION

Tourmaline

After careful optical examination of many tourmaline crystals in several samples and in various orientations, four crystals were selected for element mapping and quantitative electron probe microanalysis (EPMA) traverses. The observations reported below are consistent with all four analyzed tourmaline crystals.

Element distribution maps and EPMA data document pronounced chemical zoning in tourmaline, but all analyses plot within the field of the alkali group of Henry *et al.* (2011). As shown in Fig. 8, element distribution maps display clearly the three-stage zoning observed optically (Fig. 2b and c). The maps reveal that the core, the IR and the OR are separated by two pronounced discontinuities of markedly different appearance. The first boundary outlines a euhedral core, which is particularly well visible in the Ti and Fe maps. The second discontinuity, between IR and OR, is distinctly sutured and is particularly well recognizable in the Mg map.

Quantitative EPMA data from a traverse across the crystal shown in Fig. 8 reveal that both IR and OR are themselves simply zoned (see, for example, the decreasing Na and Fe contents of the IR, Fig. 9a). The sutured discontinuity between the IR and OR truncates the relatively simple zoning of the IR (shown clearly by Ca and Mg maps in Fig. 8) and represents a pronounced chemical gradient. In all studied crystals, this boundary is characterized by a sharp increase in Na and Mg content, and by decreases in Al, Fe_{tot}, Ca, Ti, and in the calculated number of X-site vacancies (Fig. 9a). A detailed Mg map (Fig. 2S, electronic supplementary material) reveals that the zone with highest Mg contents in the inner rim has a euhedral outline, which is parallel to the core–IR boundary. Rimward, the Mg concentration first drops to considerably lower levels before increasing abruptly at the sutured boundary with the OR. This suture cuts discordantly through both the low-Mg and the high-Mg zones of the IR. The low-Mg zone of the IR is thus not preserved

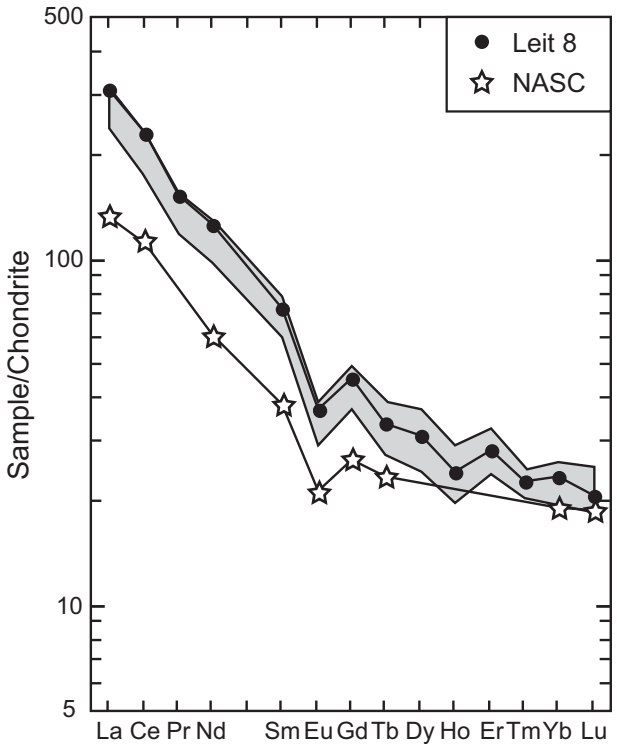

Fig. 7. Chondrite-normalized REE patterns for the metapelites at Campolungo. Continuous black line with dots represents sample Leit 8; shaded area shows the range in composition for all studied Campolungo metapelites. NASC, North American Shale Composite; data from Condie (1993). Chondrite values from Anders & Grevesse (1989).

everywhere (see Fig. 8e). A similar pattern is exhibited by the Na distribution (Fig. 8f).

The cores of analyzed tourmaline crystals contain irregularly shaped, rounded zones (e.g. Na, Ti, and Mg maps in Fig. 8). This feature is most obvious in the Ti distribution (Fig. 8c), where an ~100 μm diameter patch contains less Ti than the rest of the core (labeled D in Fig. 8a). This observation is displayed quantitatively in zoning profiles (Fig. 9a), where it is apparent that the rounded area (labeled D) also has elevated Al contents relative to the rest of the core. Based on its shape and location within the euhedral core, we interpret this, and similar rounded areas in the cores of other crystals, as detrital grains. A second feature of the euhedral crystal cores is an irregular, lamellar distribution of Ti, similar to that observed in the mica-rich matrix surrounding the tourmaline crystal (Fig. 8c). These lamellae of alternating high and low Ti concentrations are evident as color variations in transmitted light, and produce the oscillatory Ti zoning profile seen in the core section of Fig. 9a. Less well-defined lamellae are also apparent in the distributions of Mg (see detail in Fig. 2S, electronic supplementary material), Na (Fig. 8f), and Al (not shown).

A significant characteristic of the studied tourmalines is the presence of two pronounced annuli with Ca contents that are distinctly higher than that of the adjacent areas (Figs 8b and 9a). Both Ca-rich annuli are euhedral and parallel to the boundary between the core and IR. The first Ca-rich annulus occurs in the IR and is truncated by the sutured boundary between the IR and OR. A similar annulus, also truncated at the boundary between the IR and OR, appears as a narrow band with slightly lower concentrations in the Fe map (Fig. 8d, yellow band in IR; see also Fig. 9a). The outer Ca-rich annulus occurs within the OR, closer to the edge of the crystal than the zone of highest Mg and lowest Al contents (Fig. 9a). Both Ca annuli are associated with small positive spikes in the concentration profile of Ti (Figs 8c and 9a).

Identical Ca-rich annuli have been observed in all four tourmaline crystals that were mapped and/or analyzed by EPMA, and occur in both cross-sections and longitudinal sections. The CaO concentration within the annuli is 0·6–0·85 wt %, higher than in any other part of tourmaline (Table 2). In contrast, the lowest Ca concentrations are always found in the cores of tourmaline crystals (0·03–0·05 wt % CaO).

The crystal shown in Figs 2c and 8 was investigated further by laser ablation inductively coupled plasma mass spectrometry (LA-ICP-MS), whereby the SiO_2 content determined by EPMA served as an internal standard. LA-ICP-MS results reveal that the OR is markedly enriched in LREE compared with the interior parts of the crystal (Fig. 9b), where most of these elements are at or below their detection limits (Table 3). The OR displays chondrite-normalized REE values that are one order of magnitude higher than those of the IR and, moreover, it is characterized by a distinct positive Eu anomaly (Fig. 10). Pronounced zoning is also exhibited by Zn, with highest Zn contents in the core (270–280 ppm) and the IR (~250 ppm), and an abrupt decrease to 40–50 ppm at the suture between the IR and OR. Other trace elements show no sharp change in abundance at this boundary, but are gently zoned from core to IR (e.g. Sr and V, Fig. 9b). A similar pattern is exhibited by Cr (not shown), but the contents of Ni and Pb are relatively constant across the entire crystal. The studied crystal is very poor in Li, which is typical for tourmaline containing considerable amounts of Mg (e.g. Henry & Dutrow, 1990).

Garnet

Element distribution maps, electron microprobe analyses, and *in situ* UV-LA-ICP-MS data document pronounced chemical zoning in garnet. Compositional traverses and element distribution maps were obtained on carefully centered sections (based on maximum Mn concentration) through several garnet crystals in three samples. One of the most striking features displayed by garnet is the presence of a concentric, Ca-rich band, which is typically

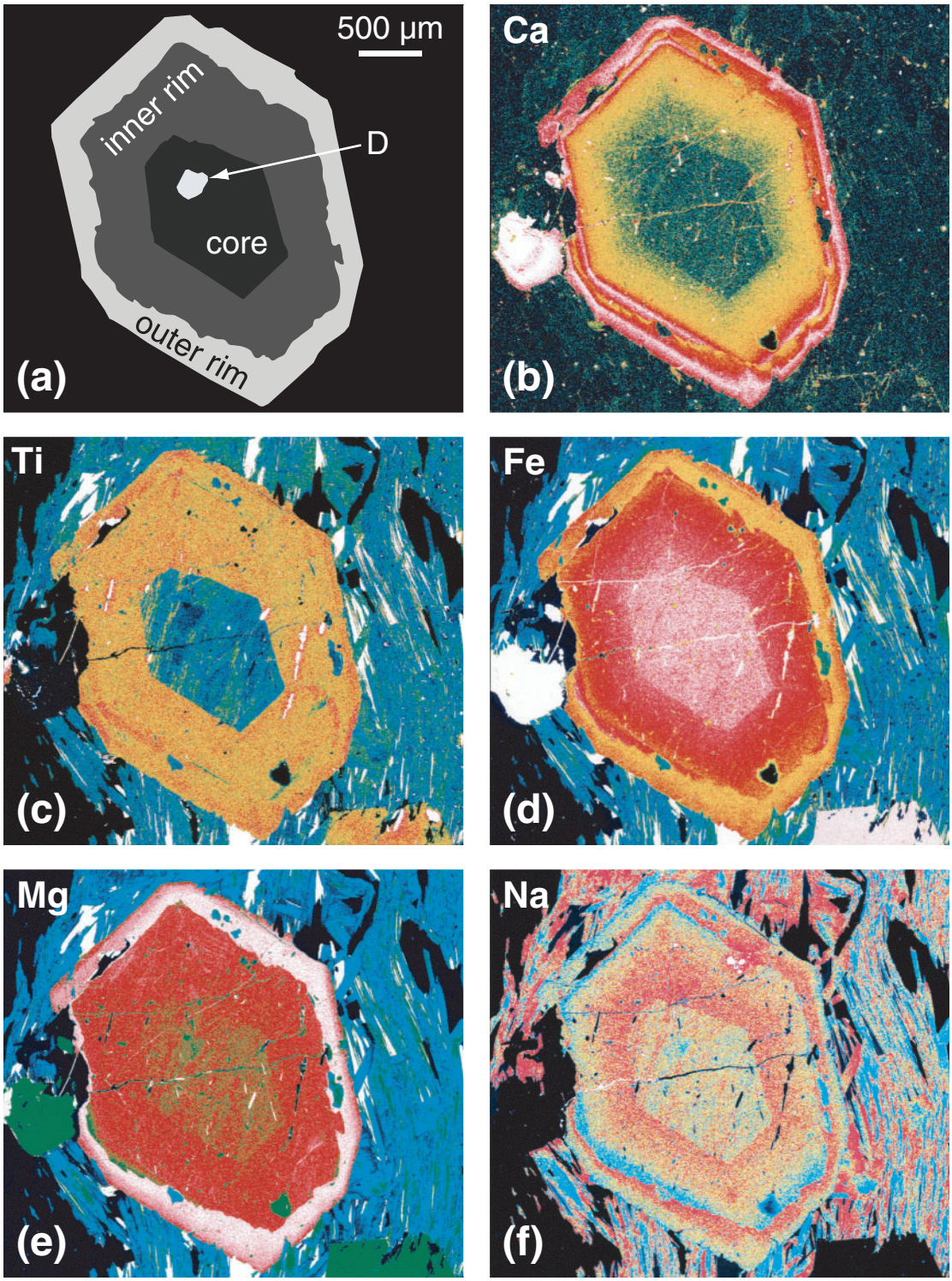

Fig. 8. Schematic diagram (a) and X-ray maps showing the distribution of various elements (b–f) within the tourmaline crystal shown in Fig. 2c (thin section Leit 8g). Small, white, irregularly shaped area, labeled D in (a), represents the detrital tourmaline core. Cool colors in X-ray maps represent low concentrations, warm colors high concentrations, white represents maximum concentration.

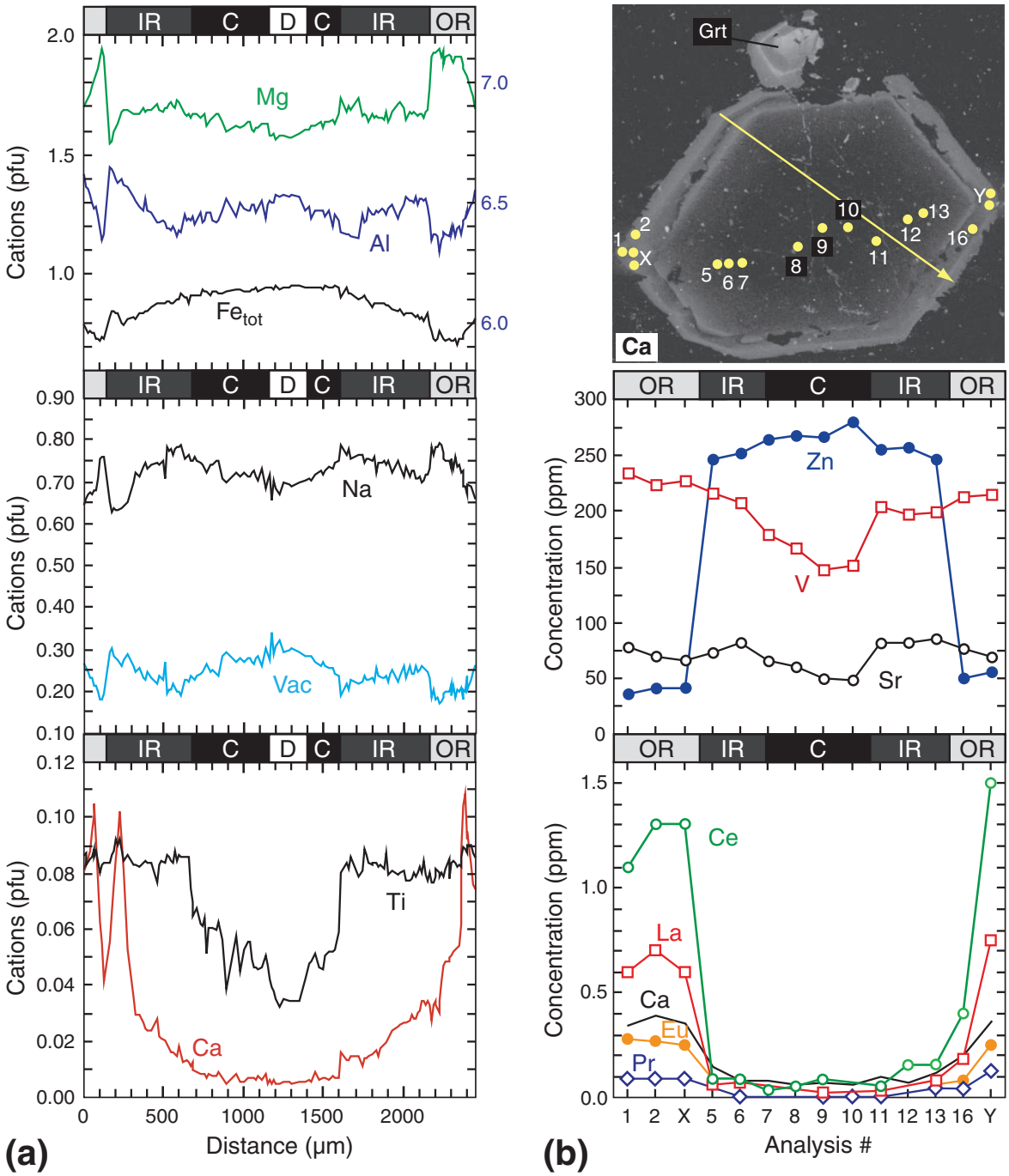

Fig. 9. Zoning profiles through the tourmaline crystal shown in Figs 2c and 8. (a) EPMA data for selected major components [in cations per formula unit (p.f.u.); 146 analyses]; (b) LA-ICP-MS data for selected trace elements (in elemental ppm, except for Ca, which is shown in wt % CaO). Image on upper right represents the Ca map of the crystal and shows where the EPMA and LA-ICP-MS data were collected. Line with arrow marks the trace of the EPMA profiles shown in (a). Numbered spots in the map indicate LA-ICP-MS analysis numbers in Table 3; X and Y designate the locations of analyses 3 and 4, and 14 and 15, which were averaged, respectively. The small crystal above the tourmaline is garnet, which displays the typical Ca-rich core as well as a Ca-rich annulus. D, detrital core; C, core; IR, inner rim; OR, outer rim; Vac, number of X-site vacancies in tourmaline (p.f.u.); Grt, garnet.

Table 2: Representative EPMA data for tourmaline from profile shown in Fig. 9 (thin section Leit 8g)

Analysis no.:	t4	t7	t9	t19	t23	t41	t49	t66	t74	t78	t81	t85	t99	t115	t129	t143	t146
Zone*:	OR	OR	OR	IR	IR	IR	C	C	D	D	C	C	IR	IR	OR	OR	OR
Micrometers:	34	71	97	231	327	640	743	1093	1228	1345	1426	1513	1800	2064	2232	2386	2424
B_2O_3 (stoich)	10·6	10·5	10·6	10·6	10·6	10·6	10·6	10·6	10·6	10·6	10·6	10·6	10·6	10·6	10·6	10·6	10·6
B_2O_3 (analyzed)	10·8	10·7	10·7	10·6	10·8	10·7	11·0	10·8	11·1	10·8	11·0	11·0	11·1	11·1	10·9	10·9	10·8
SiO_2	35·8	35·6	36·0	35·4	36·1	36·0	36·1	36·1	36·2	36·0	36·1	36·1	36·0	35·9	36·1	35·7	35·9
Al_2O_3	33·9	33·4	33·1	34·0	33·7	33·2	33·2	33·4	33·8	33·8	33·2	33·4	33·2	33·5	32·8	33·2	33·7
TiO_2	0·69	0·69	0·66	0·75	0·67	0·70	0·50	0·37	0·26	0·28	0·40	0·41	0·67	0·65	0·64	0·72	0·74
FeO (tot)	5·56	5·33	5·27	5·78	5·97	6·60	6·80	6·75	6·89	6·94	6·85	6·98	6·27	6·06	5·45	5·53	5·77
FeO (calc)	4·35	3·98	3·77	4·46	4·85	4·92	4·62	4·68	4·36	4·40	4·68	4·49	4·85	4·62	3·62	4·22	4·25
Fe_2O_3 (calc)	1·34	1·50	1·67	1·47	1·25	1·87	2·42	2·30	2·81	2·82	2·41	2·77	1·58	1·60	2·04	1·46	1·68
MnO	<0·01	<0·01	<0·01	<0·01	<0·01	<0·01	<0·01	<0·01	0·01	0·01	0·01	0·01	<0·01	0·01	<0·01	<0·01	<0·01
MgO	7·19	7·46	7·77	6·84	6·84	6·77	6·79	6·59	6·50	6·49	6·61	6·70	6·79	6·85	7·83	7·51	7·25
CaO	0·50	0·60	0·36	0·58	0·17	0·08	0·05	0·04	0·03	0·03	0·03	0·04	0·09	0·16	0·20	0·62	0·48
Na_2O	2·13	2·12	2·37	1·99	2·27	2·38	2·33	2·21	2·12	2·20	2·20	2·29	2·34	2·27	2·47	2·15	2·16
K_2O	0·01	0·02	0·02	0·01	0·02	0·02	0·02	0·02	0·01	0·02	0·03	0·02	0·01	0·02	0·02	0·01	0·02
F	0·19	0·16	0·19	0·11	0·18	0·15	0·21	0·21	0·18	0·14	0·18	0·16	0·16	0·20	0·23	0·19	0·16
H_2O (calc)	3·16	3·15	3·16	3·16	3·16	3·16	3·15	3·14	3·16	3·17	3·14	3·17	3·15	3·14	3·15	3·14	3·17
O = F	0·08	0·07	0·08	0·05	0·08	0·06	0·09	0·09	0·08	0·06	0·08	0·07	0·07	0·08	0·10	0·08	0·07
Total	99·7	99·1	99·6	99·3	99·8	99·7	99·8	99·6	100·0	99·9	99·5	100·1	99·4	99·4	99·6	99·4	100·0
On the basis of 15 cations and 31 anions																	
B (stoich)	3·000	3·000	3·000	3·000	3·000	3·000	3·000	3·000	3·000	3·000	3·000	3·000	3·000	3·000	3·000	3·000	3·000
Si	5·861	5·862	5·901	5·829	5·918	5·922	5·923	5·936	5·919	5·906	5·951	5·913	5·930	5·901	5·913	5·877	5·863
Al (tot)	6·537	6·485	6·397	6·603	6·512	6·426	6·418	6·475	6·521	6·523	6·435	6·444	6·454	6·502	6·347	6·430	6·490
Ti	0·085	0·086	0·081	0·093	0·083	0·086	0·061	0·046	0·032	0·035	0·049	0·051	0·084	0·080	0·079	0·089	0·091
Fe (tot)	0·761	0·735	0·723	0·797	0·817	0·907	0·935	0·927	0·942	0·951	0·943	0·956	0·863	0·834	0·747	0·761	0·789
Fe^{2+}	0·596	0·549	0·516	0·614	0·664	0·677	0·635	0·643	0·596	0·603	0·644	0·615	0·668	0·636	0·496	0·580	0·582
Fe^{3+}	0·166	0·186	0·206	0·183	0·154	0·231	0·299	0·284	0·345	0·348	0·299	0·341	0·196	0·199	0·251	0·181	0·207
Mn	0·000	0·000	0·000	0·000	0·000	0·000	0·000	0·000	0·001	0·001	0·002	0·001	0·000	0·001	0·000	0·000	0·000
Mg	1·755	1·832	1·899	1·679	1·670	1·658	1·663	1·616	1·584	1·586	1·621	1·635	1·669	1·682	1·913	1·843	1·768
Ca	0·088	0·105	0·063	0·102	0·030	0·014	0·008	0·008	0·005	0·006	0·006	0·007	0·015	0·028	0·034	0·109	0·083
Na	0·675	0·677	0·754	0·636	0·721	0·757	0·741	0·704	0·671	0·697	0·703	0·727	0·749	0·725	0·785	0·687	0·686
K	0·003	0·004	0·003	0·003	0·005	0·003	0·003	0·004	0·001	0·004	0·006	0·004	0·002	0·003	0·004	0·003	0·003
X-site vacancies	0·234	0·214	0·179	0·259	0·244	0·226	0·248	0·285	0·322	0·293	0·286	0·261	0·234	0·243	0·176	0·201	0·228
F	0·101	0·083	0·100	0·056	0·093	0·079	0·107	0·108	0·095	0·073	0·094	0·084	0·083	0·104	0·118	0·100	0·083
OH (calc)	3·450	3·458	3·450	3·472	3·453	3·461	3·447	3·446	3·453	3·464	3·453	3·458	3·459	3·448	3·441	3·450	3·459
O (calc)	27·450	27·458	27·450	27·472	27·453	27·461	27·447	27·446	27·453	27·464	27·453	27·458	27·459	27·448	27·441	27·450	27·459
Fe^{3+}/Fe^{2+}	0·278	0·340	0·400	0·297	0·232	0·341	0·472	0·442	0·579	0·577	0·464	0·554	0·293	0·313	0·507	0·312	0·356
$Mg/(Mg+Fe^{2+})$	0·747	0·770	0·786	0·732	0·716	0·710	0·724	0·715	0·726	0·724	0·716	0·727	0·714	0·726	0·794	0·760	0·752

*OR, outer rim; IR, inner rim; C, core; D, detrital core.

10–15 μm wide, occurs in the outer parts of crystals, and is slightly irregular to ring-like in shape (Fig. 11). All garnet crystals, independent of their size, display such a Ca-rich annulus, as also seen in Fig. 9b (small crystal above tourmaline) and Fig. 3S (electronic supplementary material). The Ca-rich band is located entirely within the garnet rim; that is, it does not coincide with the prominent boundary between the core and IR (Fig. 11a). Furthermore, the rounded annuli contrast with the more regular, polygonal shape of the Ca-rich cores. This polygonal core geometry is not visible in the distribution maps of Mg, Mn or Fe. Moreover, the Mg and Mn maps do not show the annular

Table 3: LA-ICP-MS data for tourmaline, obtained along the profile shown in Fig. 9

	Isotopic mass	Analysis no.													
		1	2	3 and 4	5	6	7	8	9	10	11	12	13	16	14 and 15
Zone*:		OR	OR	OR	IR	IR	IR	C	C	C	IR	IR	IR	OR	OR
Crater diameter (μm):		60	60	60	60	60	60	60	60	60	60	60	60	60	60
ppm															
Li	7	<14	<7	<8	8·4	<9	<8	<15	<16	8·3	<18	<8	<7	9·3	<13
B	11	32727	33077	32728	32064	32070	31608	32105	31366	33212	32362	32189	32649	31839	31928
wt %															
Na_2O	23	2·32	2·28	2·30	2·40	2·40	2·40	2·42	2·37	2·40	2·50	2·54	2·53	2·51	2·32
MgO	24	6·45	6·48	6·48	5·90	5·87	5·69	5·82	5·63	5·70	5·80	5·90	6·06	6·76	6·44
Al_2O_3	27	30·5	29·2	28·3	30·6	29·7	29·6	28·9	28·4	28·9	29·0	28·8	29·6	29·6	29·9
SiO_2[1]	29	36·0	36·0	36·0	36·0	36·0	36·0	36·0	36·0	36·0	36·0	36·0	36·0	36·0	36·0
CaO	42	0·34	0·39	0·35	0·15	0·08	0·08	<0·06	<0·07	<0·06	<0·1	0·07	0·12	0·20	0·36
TiO_2	49	0·63	0·61	0·60	0·56	0·58	0·45	0·39	0·37	0·35	0·55	0·55	0·58	0·56	0·61
ppm															
V	51	233	223	226	216	208	180	166	147	151	203	196	198	213	214
Cr	52	154	119	150	199	186	179	128	139	157	211	178	179	247	281
wt %															
FeO	57	4·7	4·7	4·6	5·1	5·1	5·4	5·6	5·6	5·6	5·5	5·4	5·3	4·4	4·6
ppm															
Ni	60	162	176	174	170	162	163	168	174	173	162	174	176	206	159
Zn	66	36	41	42	246	252	264	268	266	279	255	256	247	51	55
As	75	<1	<0·7	<0·7	<0·9	<0·8	<0·7	<0·8	<0·7	<0·7	14	1·3	0·65	<0·6	<0·6
Sr	88	78	69	66	74	82	67	61	51	49	82	83	85	77	70
Y	89	<0·07	<0·08	<0·06	<0·06	<0·07	<0·04	<0·06	<0·08	<0·07	<0·09	<0·07	0·2	<0·08	<0·06
Zr	90	0·09	<0·09	<0·1	<0·1	<0·2	<0·1	<0·1	<0·1	6·0	0·5	<0·09	66	<0·2	<0·1
Nb	93	<0·2	<0·1	0·16	<0·2	<0·1	<0·2	<0·2	<0·2	<0·2	0·24	0·25	0·20	<0·1	<0·4
Cs	133	<0·04	0·12	<0·1	<0·03	0·34	0·10	0·06	<0·04	0·14	0·05	0·24	0·23	0·14	6·4
La	139	0·6	0·7	0·6	0·06	0·07	<0·05	<0·04	0·02	<0·04	0·03	<0·05	0·08	0·18	0·75
Ce	140	1·1	1·3	1·3	0·09	0·09	0·03	0·05	0·09	<0·04	0·05	0·16	0·16	0·40	1·5
Pr	141	0·09	0·09	0·09	<0·05	0·01	<0·02	<0·04	0·01	0·01	0·01	<0·06	0·04	0·04	0·13
Nd	146	0·2	0·3	0·3	0·06	<0·3	<0·1	<0·2	0·02	<0·2	0·03	<0·2	<0·1	<0·2	0·4
Sm	147	<0·2	<0·3	<0·2	<0·4	0·05	<0·2	<0·2	<0·2	<0·2	<0·4	<0·2	<0·3	<0·2	<0·2
Eu	153	0·28	0·27	0·25	<0·09	<0·08	<0·04	<0·07	<0·06	<0·08	<0·09	<0·04	<0·06	0·08	0·25
Gd	157	<0·3	<0·4	<0·2	0·03	<0·4	<0·4	<0·2	<0·4	<0·4	<0·5	<0·4	<0·3	<0·2	<0·3
Tb	159	<0·05	0·01	0·01	<0·04	<0·03	<0·04	<0·05	0·01	<0·05	0·02	<0·05	<0·04	<0·03	<0·05
Dy	163	<0·1	<0·3	<0·06	<0·2	<0·3	<0·1	0·03	<0·3	<0·2	<0·4	<0·2	0·06	<0·2	<0·2
Ho	165	<0·08	<0·04	<0·04	0·02	<0·04	<0·06	0·01	<0·06	<0·04	<0·07	<0·03	<0·04	<0·03	<0·08
Er	166	<0·2	<0·2	<0·2	<0·2	<0·2	<0·1	<0·1	<0·1	<0·2	0·05	<0·2	<0·1	<0·1	<0·2
Tm	169	<0·05	<0·05	<0·04	<0·06	<0·05	<0·05	<0·06	<0·06	<0·05	<0·09	<0·04	<0·06	<0·06	<0·06
Yb	173	<0·3	<0·2	<0·2	<0·5	<0·2	<0·3	<0·2	<0·2	<0·2	0·09	0·01	<0·3	<0·2	<0·2
Lu	175	<0·04	0·01	<0·02	0·01	0·01	<0·03	0·02	<0·08	<0·04	<0·07	<0·06	<0·05	0·01	<0·06
Ta	181	<0·05	<0·05	<0·08	<0·06	<0·1	0·01	<0·04	<0·08	<0·06	0·02	0·01	<0·09	<0·04	<0·08
Pb	208	9·9	9·8	9·5	9·6	11	9·0	8·7	7·5	7·8	12	12	11	11	20
Bi	209	0·10	<0·05	<0·04	0·01	<0·03	<0·04	<0·03	<0·06	0·14	<0·04	<0·03	<0·03	0·03	<0·03
Th	232	0·01	<0·03	<0·04	0·01	0·01	<0·04	<0·04	<0·05	<0·03	<0·08	<0·05	<0·04	<0·05	<0·05
U	238	<0·05	<0·03	<0·05	<0·03	<0·04	<0·03	<0·03	<0·03	0·07	0·02	0·02	0·6	<0·03	<0·02

*OR, outer rim; IR, inner rim; C, core.
[1]SiO_2 concentration as determined by EPMA used as internal standard.

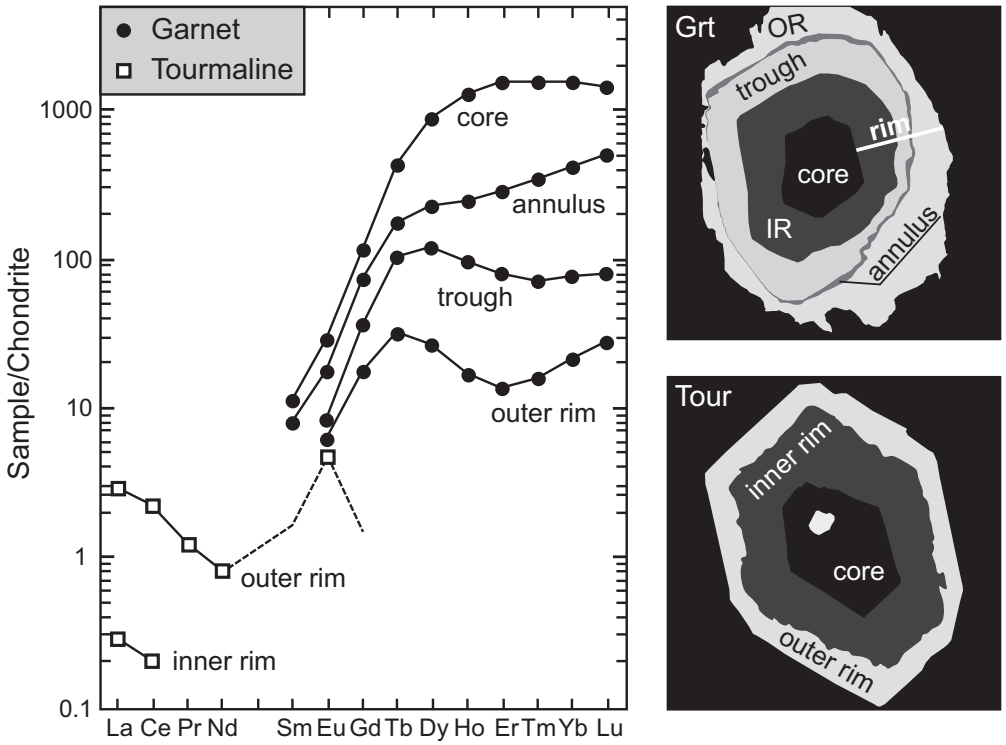

Fig. 10. Chondrite-normalized REE patterns for tourmaline (open squares) and garnet (black dots) from the metapelites at Campolungo. LA-ICP-MS data for crystals from thin section Leit 8g. Chondrite values from Anders & Grevesse (1989). Schematic diagrams on right identify the zones within garnet and tourmaline (see Figs 8, 9 and 11, 12). IR, inner rim; OR, outer rim; Grt, garnet; Tour, tourmaline. Dashed lines connect to detection limits of elements that were not detected (no symbol shown).

features observed for Ca, although the Fe map reveals a coincident ring of low Fe content (Fig. 11c).

These qualitative observations are corroborated by quantitative EPMA data obtained from traverses across several garnet crystals. The EPMA data discussed here (Table 4) are representative of all other studied garnet crystals from several samples. Chemical variation is characterized by bell-shaped zoning profiles for MnO and CaO, with maximum contents of 3 wt % for both components in the crystal core. Magnesium exhibits the opposite behavior, with MgO contents of ~1·8 wt % in the core and ~4 wt % near the edge of the crystals. In contrast to the smooth changes observed in the rim–core–rim Mg and Mn profiles, the Ca profile displays prominent spikes, with abrupt increases in Ca content (Fig. 12a). These spikes, where CaO concentrations reach 1·5 wt % (Table 4), are the Ca-rich, Fe-depleted annuli described above (Fig. 11). Maximum X_{grs} of the spike is less than that of the crystal core. Both the X-ray map (Fig. 11b) and the chemical profile (Fig. 12a) demonstrate that the variation in Ca concentration across the annuli is not symmetric, but rather displays a steep slope on the inner side of the annulus and a more gradual decrease in concentration on the outer side. A distinct change in Ca content is also observed at the boundary between the Ca-rich core and the IR of garnet (Fig. 12a). In some cases, there is a zone rich in apatite inclusions between the IR and the annuli (see Fig. 3S, electronic supplementary material).

To study the distribution of trace elements in garnet, and in particular in the Ca-rich annuli, the representative crystal shown in Figs 11 and 12 was also subjected to *in situ* chemical analysis using LA-ICP-MS. The Al_2O_3 content of garnet, as determined by EPMA, served as an internal standard for the LA-ICP-MS analysis. As a consistency check, data were also collected for some major components, and these are in good agreement with those obtained by EPMA (compare CaO, MgO and MnO contents in Tables 4 and 5). The results show that the sharp spike in Ca coincides with prominent spikes in the concentration of several trace elements, especially the REE (Fig. 12b). Indeed, the Ca concentration profile is broadly mimicked by all detectable REE, with the highest REE contents found in the garnet core. From core to rim, the REE contents decrease continuously until the Ca-rich annulus is reached, at which point a marked increase in REE concentrations is observed (Fig. 12b). Rimward of the Ca spike, the REE concentrations decrease again, reaching their lowest levels at the edge of the crystal.

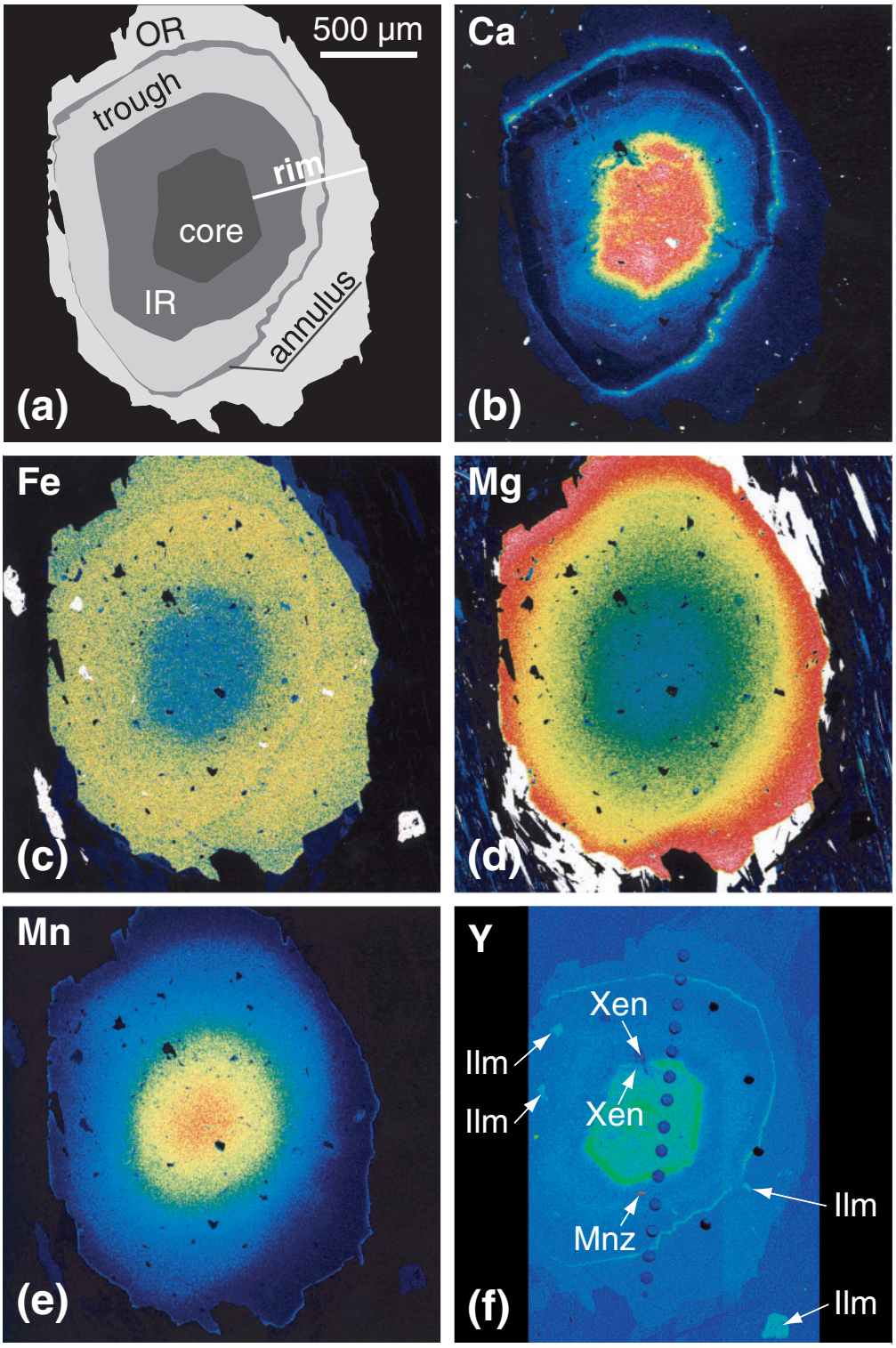

Fig. 11. Schematic diagram (a) and X-ray maps showing the distribution of various elements (b–f) within a typical garnet crystal (thin section Leit 8g). The Ca-rich core displays a roughly six-sided outline, whereas the Ca-rich annulus exhibits a ring-like shape. The dots forming a straight line in (f) represent craters that resulted from LA-ICP-MS analysis (see Fig. 12a). Cool colors in X-ray maps represent low concentrations, warm colors high concentrations, white represents maximum concentration. IR, inner rim; OR, outer rim; Ilm, ilmenite; Mnz, monazite; Xen, xenotime.

Table 4: Representative EPMA data for garnet from profile shown in Fig. 12 (thin section Leit 8g)

Analysis no.:	Gar2	Gar3	Gar24	Gar31	Gar36	Gar50	Gar63	Gar76	Gar89	Gar93	Gar112	Gar148	Gar163	Gar168	Gar174	Gar186	Gar189
Micrometers:	15	26	355	456	547	721	883	1051	1218	1267	1514	1996	2168	2230	2291	2426	2475
SiO_2	38·1	37·9	37·5	37·6	37·4	37·4	37·2	37·4	37·3	37·2	37·3	37·0	37·3	37·3	37·5	37·6	37·7
Al_2O_3	21·9	21·7	21·4	21·2	21·5	21·5	21·4	21·5	21·3	21·5	21·4	21·1	21·5	21·5	21·5	21·8	21·3
Cr_2O_3	<0·01	0·03	0·01	<0·01	0·02	<0·01	0·01	0·05	0·02	<0·01	<0·01	0·03	0·01	0·01	0·02	0·01	0·02
TiO_2	<0·02	0·02	0·04	0·01	0·04	0·08	0·04	0·02	0·04	0·02	0·12	0·03	<0·01	0·01	0·04	0·01	<0·01
FeO (tot)	37·0	37·0	38·3	37·5	38·7	38·5	36·8	34·9	34·8	34·8	35·0	38·3	38·1	37·3	37·7	37·0	37·4
MnO	0·27	0·23	0·47	0·76	0·96	1·36	1·94	2·33	2·76	2·78	2·36	1·13	0·89	0·76	0·48	0·39	0·59
ZnO	0·04	<0·01	<0·01	0·01	0·06	0·01	<0·02	0·01	0·02	<0·01	<0·01	0·04	<0·02	0·02	0·02	<0·01	0·02
MgO	4·15	4·28	3·11	2·54	2·49	2·35	2·04	1·84	1·82	1·82	1·91	2·53	2·85	2·94	3·57	4·11	3·77
CaO	0·42	0·41	0·58	1·44	0·42	0·81	1·74	3·04	2·61	2·62	2·59	0·65	0·29	1·19	0·56	0·42	0·41
Na_2O	0·03	0·02	0·04	0·02	0·02	0·05	0·07	0·08	0·10	0·09	0·06	0·06	0·11	0·01	0·05	0·02	0·02
Total	101·9	101·7	101·5	101·1	101·6	102·0	101·3	101·2	100·7	100·9	100·8	100·9	101·2	101·1	101·4	101·3	101·3
Cations per formula unit based on 12 oxygens																	
Si	2·992	2·989	2·987	3·005	2·987	2·978	2·983	2·989	2·997	2·986	2·991	2·979	2·986	2·981	2·980	2·979	2·998
Al	2·028	2·016	2·011	2·001	2·020	2·016	2·021	2·023	2·016	2·033	2·024	2·007	2·028	2·025	2·014	2·030	1·997
Cr	0·000	0·002	0·001	0·000	0·001	0·000	0·001	0·003	0·001	0·000	0·000	0·002	0·001	0·001	0·001	0·001	0·001
Ti	0·000	0·001	0·002	0·000	0·002	0·005	0·002	0·001	0·002	0·001	0·007	0·002	0·000	0·001	0·002	0·001	0·000
Fe^{2+} (tot)	2·431	2·438	2·551	2·508	2·587	2·566	2·466	2·335	2·337	2·338	2·351	2·581	2·551	2·492	2·505	2·447	2·482
Mn	0·018	0·015	0·032	0·051	0·065	0·092	0·131	0·158	0·188	0·189	0·160	0·077	0·060	0·051	0·032	0·026	0·040
Zn	0·002	0·000	0·000	0·001	0·004	0·001	0·000	0·000	0·001	0·000	0·000	0·002	0·000	0·001	0·001	0·000	0·001
Mg	0·486	0·503	0·369	0·302	0·297	0·279	0·244	0·220	0·218	0·217	0·229	0·304	0·340	0·351	0·423	0·485	0·446
Ca	0·035	0·034	0·049	0·123	0·036	0·069	0·149	0·261	0·225	0·225	0·222	0·056	0·025	0·102	0·048	0·035	0·035
Na	0·005	0·003	0·007	0·003	0·003	0·008	0·010	0·013	0·015	0·014	0·010	0·010	0·017	0·001	0·007	0·003	0·004
Sum (cat)	7·997	8·002	8·008	7·996	8·002	8·013	8·009	8·003	8·000	8·003	7·994	8·020	8·008	8·006	8·014	8·007	8·004
Al(IV)	0·008	0·011	0·013	0·000	0·013	0·022	0·017	0·011	0·003	0·014	0·009	0·021	0·014	0·019	0·020	0·021	0·002
Al(VI)	2·020	2·006	1·998	2·001	2·007	1·994	2·005	2·013	2·013	2·019	2·015	1·986	2·014	2·006	1·994	2·009	1·995
SUM (oct)	2·020	2·008	2·001	2·002	2·010	1·999	2·008	2·017	2·016	2·020	2·022	1·990	2·015	2·008	1·998	2·010	1·997
SUM (cub)	2·977	2·994	3·007	2·990	2·991	3·014	3·001	2·985	2·983	2·983	2·972	3·030	2·993	2·998	3·016	2·996	3·008
X(alm)	0·817	0·814	0·848	0·839	0·865	0·851	0·822	0·782	0·783	0·784	0·791	0·852	0·852	0·831	0·830	0·817	0·825
X(grs)	0·012	0·011	0·016	0·041	0·012	0·023	0·050	0·087	0·075	0·075	0·075	0·019	0·008	0·034	0·016	0·012	0·012
X(prp)	0·163	0·168	0·123	0·101	0·099	0·093	0·081	0·074	0·073	0·073	0·077	0·100	0·114	0·117	0·140	0·162	0·148
X(sps)	0·006	0·005	0·011	0·017	0·022	0·030	0·044	0·053	0·063	0·063	0·054	0·025	0·020	0·017	0·011	0·009	0·013
X(uva)	0·000	0·001	0·000	0·000	0·001	0·000	0·000	0·002	0·001	0·000	0·000	0·001	0·000	0·000	0·001	0·000	0·001

Analogous distributions are exhibited by Sr and Y (Table 5, Fig. 12b). Both the Y-rich core, with a distinct hexagonal outline, and the Y-rich annulus are clearly visible in the Y distribution map shown in Fig. 11f. Crystal-scale zoning of V and Zn (Fig. 12b), as well as Nb and Cr (not shown), is far less pronounced than in tourmaline. Significant core-to-rim increases in Co content are observed.

REE zoning in garnet is associated with a marked core-to-rim change in the chondrite-normalized REE patterns. The garnet core displays a typical heavy REE (HREE)-enriched pattern, which is flat for the HREE and decreases sharply toward the LREE (Fig. 10), yielding a $(Sm/Lu)_{CN}$ value of 0·01. The $(Sm/Lu)_{CN}$ value, however, is twice as large in the Ca-rich annulus. Moreover, the chondrite-normalized values for the HREE in the core are nearly two orders of magnitude larger than in the OR. The chondrite-normalized patterns of both the 'trough' (low-Ca zone just inside the Ca annulus, corresponding to the average of analyses 6 and 15 in Fig. 12b) and the OR display a prominent sinusoidal shape (Fig. 10).

The Y map reveals a number of tiny xenotime inclusions in garnet, which were also analyzed qualitatively by

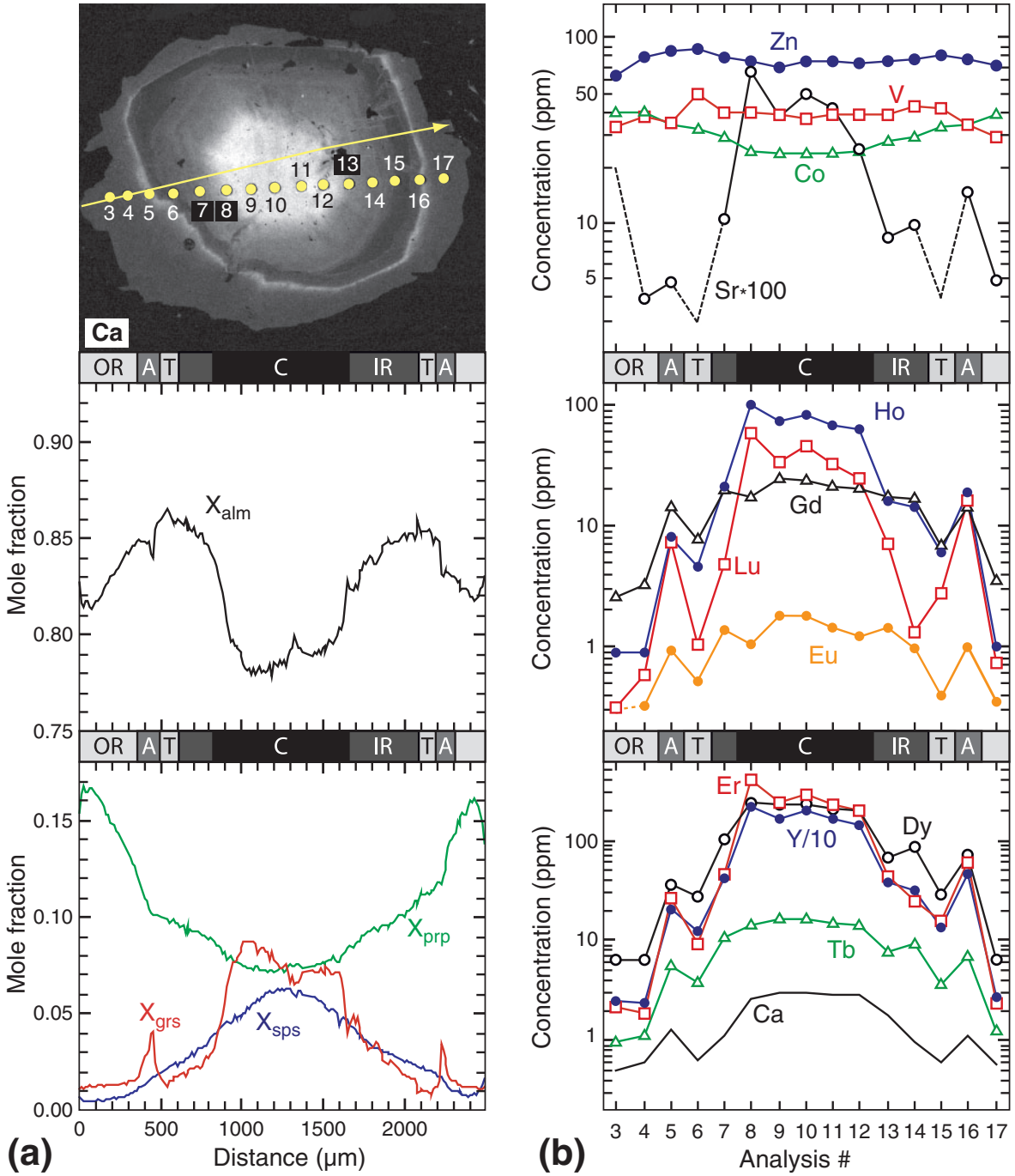

Fig. 12. Zoning profiles through the garnet crystal shown in Fig. 11. (a) EPMA data for the major garnet components, plotted as mole fractions of respective end-members (187 analyses). Image on upper left represents the Ca map of the crystal and shows where the EPMA and LA-ICP-MS data were collected. Line with arrow marks the trace of the EPMA profiles shown in (a). (b) LA-ICP-MS data for selected trace elements (in elemental ppm, except for Ca, which is shown in wt % CaO). Profiles for Tm and Yb are not shown, as they are virtually identical to those of Lu and Er, respectively. Dashed lines connect to detection limits of elements that were not detected (no symbol shown). Traverse shows profile indicated in the Ca map shown in upper left, where the numbered spots indicate analysis numbers in Table 5. C, core; IR, inner rim; T, trough; A, annulus; OR, outer rim; alm, almandine; grs, grossular; prp, pyrope; sps, spessartine.

Table 5: LA-ICP-MS data for garnet, obtained along the profile shown in Fig. 12

	Isotopic mass	Analysis no.														
		3	4	5	6	7	8	9	10	11	12	13	14	15	16	17
Crater diameter (μm):		40	80	80	80	80	80	80	80	80	80	80	80	80	80	80
wt %																
Na_2O	23	0·05	0·05	0·04	0·05	0·07	0·11	0·11	0·11	0·09	0·07	0·06	0·07	0·07	0·03	0·04
MgO	25	4·33	3·05	2·76	2·76	2·59	2·26	2·13	2·11	2·17	2·25	2·45	2·67	2·85	2·94	3·00
Al_2O_3*	27	21·8	21·7	21·6	21·5	21·4	21·4	21·4	21·4	21·4	21·4	21·4	21·4	21·6	21·7	21·8
CaO	42	0·50	0·60	1·27	0·63	1·09	2·61	3·07	2·95	2·92	2·83	1·77	0·96	0·59	1·10	0·59
TiO_2	49	0·02	0·03	0·04	0·10	0·05	0·08	0·28	0·26	0·10	0·02	0·04	0·05	0·04	0·07	0·02
ppm																
V	51	33	38	35	50	39	39	39	36	39	39	39	43	42	34	29
Cr	53	95	102	62	116	111	94	93	73	66	85	78	66	121	79	93
wt %																
MnO	55	0·31	0·46	0·63	0·96	1·33	1·88	2·23	2·37	2·22	1·93	1·56	1·13	0·92	0·73	0·46
ppm																
Co	59	40	39	34	32	29	25	24	24	24	24	28	29	33	34	39
Ni	62	<10	<5	<3	<2	<3	<4	<4	<4	<3	<5	<4	<6	<5	<3	<3
Zn	66	62	79	85	87	79	75	69	74	74	74	75	77	80	77	70
Rb	85	<0·3	<0·06	0·07	<0·07	0·09	0·55	0·24	0·34	0·28	0·24	0·06	<0·05	<0·08	0·10	<0·08
Sr	88	<0·2	0·04	0·05	<0·03	0·11	0·65	0·38	0·50	0·41	0·25	0·09	0·10	<0·04	0·15	0·05
Y	89	24	24	205	122	427	2152	1657	1983	1682	1446	377	310	137	454	28
Zr	90	2·7	3·1	2·4	1·3	2·2	1·0	1·3	0·9	2·3	0·8	1·6	2·2	1·4	1·6	2·1
Nb	93	<0·2	<0·05	0·1	1·5	0·04	0·6	5·2	4·1	1·2	0·4	0·1	<0·06	<0·05	0·5	<0·05
Cs	133	<0·1	<0·04	<0·04	<0·06	<0·06	<0·05	<0·06	<0·05	<0·04	<0·05	<0·06	<0·05	<0·05	<0·05	<0·04
Ba	137	<1	<0·4	<0·5	<0·4	<0·4	<0·4	<0·3	<0·3	<0·4	<0·4	<0·3	<0·3	<0·2	0·02	<0·3
La	139	<0·1	<0·04	<0·07	<0·03	<0·07	<0·07	<0·03	0·06	<0·05	<0·05	<0·04	<0·02	<0·05	0·03	<0·04
Ce	140	<0·2	<0·05	<0·02	<0·05	<0·04	<0·05	<0·04	0·25	0·12	<0·04	<0·04	<0·02	<0·05	<0·03	<0·03
Pr	141	<0·08	<0·03	<0·02	<0·05	<0·03	<0·04	<0·04	<0·04	<0·03	<0·04	<0·04	<0·03	<0·04	<0·03	<0·03
Nd	146	0·16	<0·1	<0·2	<0·2	<0·2	<0·2	<0·3	<0·2	<0·2	0·18	<0·2	<0·2	<0·4	<0·3	<0·2
Sm	147	<1·9	<0·4	1·4	0·7	1·3	1·0	1·9	2·0	1·4	1·3	1·6	1·2	<0·4	1·0	0·4
Eu	153	<0·3	0·3	0·9	0·5	1·4	1·1	1·8	1·8	1·4	1·2	1·4	1·0	0·4	1·0	0·4
Gd	157	2·5	3·2	14	7·6	20	17	25	24	21	20	18	17	6·7	14	3·6
Tb	159	1·0	1·1	5·4	3·8	11	14	16	17	15	14	7·8	9·4	3·6	7·1	1·2
Dy	163	6·3	6·4	37	27	101	244	224	234	206	197	66	83	29	72	6·3
Ho	165	0·9	0·9	8·0	4·6	21	100	73	81	67	62	16	14	6·1	19	1·0
Er	167	2·1	1·9	26	9·47	47	399	240	291	227	202	45	25	16	62	2·4
Tm	169	0·4	0·3	4·9	1·1	5·5	68	37	46	36	30	6·4	2·2	2·3	12	0·4
Yb	173	<1·9	3·4	42	7·9	35	473	248	320	236	191	48	11	17	94	3·5
Lu	175	0·3	0·6	7·4	1·1	4·9	59	34	45	33	25	7·1	1·3	2·8	16	0·7
Hf	178	<0·9	<0·3	<0·1	<0·14	0·17	<0·1	<0·4	0·19	<0·2	<0·3	<0·4	<0·2	<0·3	<0·2	<0·3
Ta	181	0·07	<0·08	<0·09	0·12	<0·1	0·08	0·39	0·27	0·13	<0·07	<0·1	<0·08	<0·2	0·06	<0·07
Th	232	<0·2	<0·1	<0·09	<0·07	<0·1	<0·08	<0·09	<0·07	<0·1	<0·08	<0·05	<0·07	<0·2	<0·07	0·03
U	238	<0·2	<0·04	<0·1	<0·07	0·06	<0·06	<0·1	<0·09	0·12	<0·08	<0·07	<0·06	<0·09	<0·07	<0·04

*Al_2O_3 concentration as determined by EPMA used as internal standard.

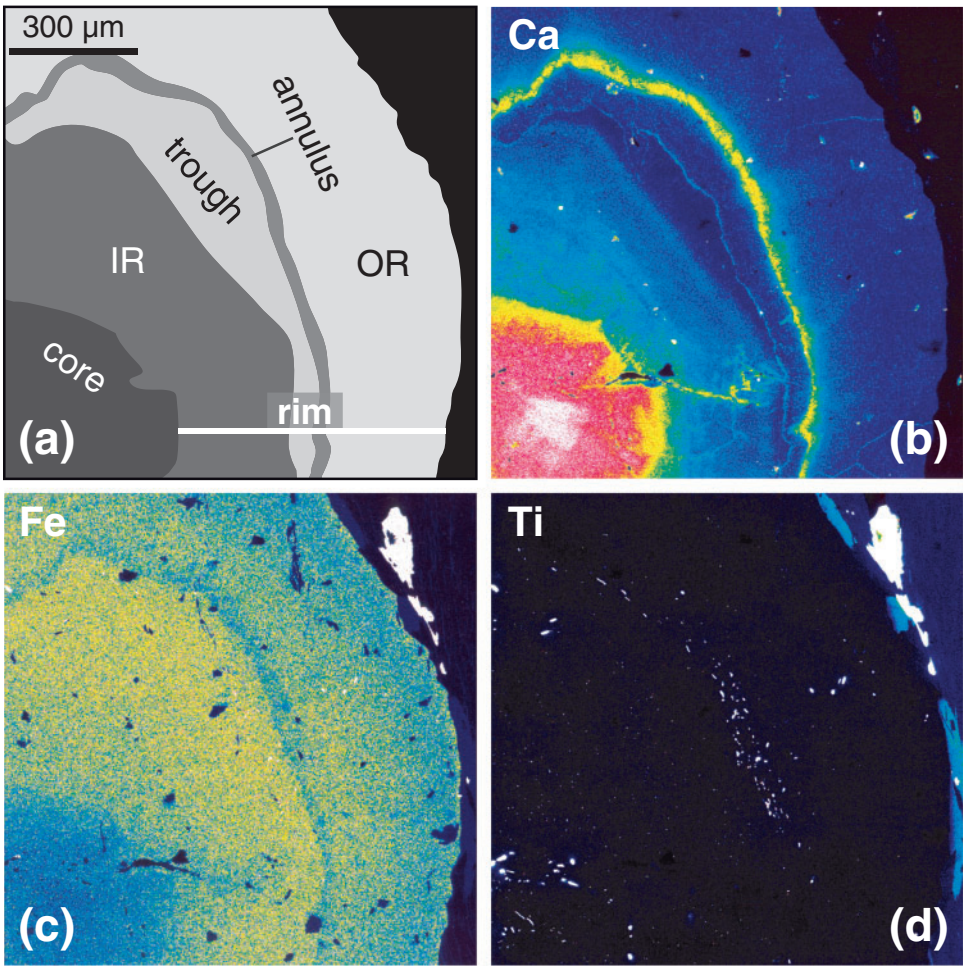

Fig. 13. Detail of a garnet crystal from thin section Leit 8d. (a) Sketch identifying the zones defined by the element distribution maps of (b) Ca, (c) Fe, and (d) Ti. The maps show that rutile inclusions are especially abundant in the Ca-rich core (lower left corner) and in the low-Ca trough just inside the Ca-rich annulus (depleted in Fe). Outside the annulus as well as in the surrounding rock matrix the Ti phase is ilmenite. Cool colors in X-ray maps represent low concentrations, warm colors high concentrations, white represents maximum concentration. IR, inner rim; OR, outer rim.

energy-dispersive X-ray (EDX) spectroscopy. These inclusions are restricted to the area inside the Ca-rich annulus, where they occur mostly inside the hexagonal-shaped high-Y zone of the core (Fig. 11f). Element distribution maps and EDX analyses further indicate that monazite is present in several garnet crystals, but mostly at, or outside, the Ca- and Y-annulus (Klapper, 2008).

The garnet porphyroblasts in these metapelites exhibit an additional striking characteristic: all studied crystals contain abundant Ti-mineral inclusions in their interior parts but only scarce Ti-mineral inclusions outside the Ca-rich annulus. Moreover, Ti-mineral inclusions are especially abundant in two distinct zones: the Ca-rich core, and the low-Ca trough just inside the Ca-rich annulus (Fig. 13). The related Fe and Ti distribution maps (Fig. 13) reveal that inclusions inside the Ca-rich annulus are almost exclusively rutile, whereas on the outside the few inclusions are ilmenite. This phase identification has been verified by EDX spectra of numerous inclusions. Very rare ilmenite crystals have been observed inside the annulus, where they occur typically in the low-Ca trough.

Other major and minor minerals

The composition of the other major minerals, and of ilmenite, plagioclase and chlorite, in various thin sections is given in Table 6. Trace element data obtained by LA-ICP-MS analysis are listed in Table 7 for selected minerals from thin section Leit 8 g.

Biotite exhibits a statistically identical average chemical composition in all samples. It has an X_{Mg} of ~0·51, and contains ~1·4 wt % TiO_2 and 0·4 wt % Na_2O. The sum of all alkali-site cations amounts to only 0·85 per formula unit (p.f.u.). The Li content of biotite is 70 ppm, 10 times

Table 6: Average compositions (EPMA data) and oxygen-normalized formulae of biotite, muscovite, staurolite, kyanite, ilmenite, plagioclase, and chlorite occurring in the metapelites at Campolungo (microprobe sections from samples Leit 8, Leit 400, and Leit 10)

Mineral:	Biotite	Biotite	Biotite	Muscovite	Muscovite	Muscovite	Staurolite	Staurolite	Kyanite	Ilmenite	Plagioclase	Plagioclase	Chlorite
Section:	Leit 8c[1]	Leit 8c[2]	Leit 8d[1]	Leit 8c[1]	Leit 8d[1]	Leit 8d[3]	Leit 8c	Leit 8g	Leit 8c	Leit 8c	Leit 400	Leit 10b	Leit 400[4]
n:	20	41	44	37	127	15	14	69	32	9	14	14	7
SiO_2	36·3(6)	36·5(7)	36·8(4)	46·5(7)	47·6(6)	48·9(5)	28·6(3)	28·0(4)	37·2(3)	n.a.	67·1(5)	64·5(4)	25·0(2)
Al_2O_3	19·6(3)	19·9(4)	19·1(3)	36·8(7)	37·0(7)	36(1)	53·6(4)	53·5(6)	63·8(3)	<0·02	21·1(3)	22·5(1)	23·3(3)
Cr_2O_3	0·05(7)	0·05(7)	0·04(3)	0·05(6)	0·04(5)	0·03(3)	n.a.	0·04(2)	0·07(4)	n.a.	<0·01	n.a.	0·01(1)
TiO_2	1·5(1)	1·3(2)	1·42(9)	0·35(7)	0·39(7)	0·38(6)	0·61(5)	0·63(5)	0·01(2)	53·3(4)	0·01(1)	0·01(1)	0·11(2)
FeO_{tot}	18·7(5)	18·3(4)	18·7(5)	0·8(2)	0·8(2)	0·9(2)	13·4(1)	13·9(2)	0·18(5)	47·9(4)	0·02(2)	0·1(1)	23·8(6)
MnO	0·05(7)	0·04(5)	0·02(3)	0·03(5)	0·02(4)	0·01(2)	0·03(1)	0·04(2)	0·01(1)	0·17(3)	0·01(1)	0·01(1)	0·03(2)
NiO	0·04(5)	0·06(7)	0·04(3)	0·02(5)	0·02(3)	0·01(1)	n.a.	0·02(2)	0·01(1)	n.a.	n.a.	n.a.	n.a.
ZnO	n.a.	n.a.	n.a.	n.a.	n.a.	n.a.	0·36(3)	0·35(2)	n.a.	n.a.	n.a.	n.a.	n.a.
MgO	10·8(4)	11·2(2)	10·9(2)	0·6(2)	0·6(2)	0·8(3)	1·89(9)	1·9(1)	0·01(1)	0·34(3)	<0·01	<0·01	16·0(4)
CaO	<0·01	<0·02	<0·02	<0·01	<0·01	<0·01	n.a.	<0·01	0·01(2)	n.a.	1·5(2)	3·2(1)	0·01(1)
Na_2O	0·40(8)	0·42(6)	0·40(3)	2·2(2)	2·0(2)	1·8(3)	n.a.	0·01(1)	0·01(1)	n.a.	10·8(1)	9·9(1)	0·01(1)
K_2O	8·5(2)	8·2(2)	8·0(1)	8·2(3)	7·8(2)	7·8(3)	n.a.	<0·02	0·01(1)	n.a.	0·08(2)	0·09(2)	0·04(7)
H_2O[5]	4·02	4·03	4·00	4·57	4·63	4·67	1·83	1·72					11·6
Total	100·0	100·0	99·3	100·2	100·9	101·6	100·3[6]	100·1[7]	101·4	101·7	100·7	100·3	99·8
Oxygens	11	11	11	11	11	11	46·5	46·5	5	3	8	8	28
Li							0·054	0·054					
Si	2·710	2·715	2·753	3·049	3·084	3·140	7·945	7·828	0·991		2·922	2·836	5·184
Al	1·728	1·745	1·688	2·846	2·822	2·746	17·574	17·613	2·006		1·082	1·166	5·688
Cr	0·003	0·003	0·003	0·003	0·002	0·002		0·010	0·001				0·002
Ti	0·084	0·074	0·080	0·017	0·019	0·019	0·128	0·132	0·000	0·992	0·000	0·000	0·016
Fe^{2+}	1·170	1·138	1·169	0·047	0·046	0·048	3·103	3·246	0·004	0·992	0·001	0·003	4·122
Mn	0·003	0·002	0·001	0·001	0·001	0·001	0·007	0·010	0·000	0·004	0·000	0·000	0·006
Ni	0·003	0·004	0·002	0·001	0·001	0·000		0·004	0·000				
Zn							0·074	0·073					
Mg	1·208	1·237	1·215	0·058	0·060	0·079	0·783	0·780	0·001	0·013			4·926
Ca									0·000		0·071	0·149	0·002
Na	0·057	0·060	0·058	0·283	0·255	0·221		0·006	0·001		0·914	0·845	0·005
K	0·807	0·780	0·763	0·689	0·644	0·643			0·000		0·004	0·005	0·011
ΣCations	7·772	7·758	7·732	6·995	6·934	6·899	29·667[8]	29·759[9]	3·005	2·000	4·995	5·006	19·963
OH (calc)	2·000	2·000	2·000	2·000	2·000	2·000	3·400	3·216					16·000
Al(IV)	1·290	1·285	1·247	0·951	0·916	0·860	0·055	0·172					2·816
Al(VI)	0·438	0·460	0·441	1·896	1·906	1·886	17·519	17·442					2·872
Na + K + Ca	0·864	0·840	0·821	0·972	0·898	0·864					0·989	0·999	
Mg/(Fe + Mg)	0·508	0·521	0·510	0·555	0·569	0·621	0·202	0·194		0·013			0·544

Values in parentheses are standard deviations (σ_{n-1}) of the average and apply to the last digit. n.a., not analyzed.
[1]In foliation.
[2]In pressure shadow.
[3]Post-tectonic (cross-mica).
[4]Retrograde.
[5]H_2O contents calculated according to stoichiometry. For staurolite, the H_2O content was calculated according to the procedure of Hawthorne (1995) using a Li_2O content of 0·048 wt %, as determined by LA-ICP-MS.
[6]Total includes 0·048 wt % Li_2O, as determined by LA-ICP-MS analysis.
[7]Total includes 0·048 wt % Li_2O, as determined by LA-ICP-MS analysis, and 0·02(3) wt % F (corresponding to 0·016 F p.f.u.).
[8]Includes 0·054 Li.
[9]Includes 0·054 Li.

Table 7: Average elemental concentrations (in ppm) in selected minerals from thin section Leit 8g (LA-ICP-MS data)

	Isotopic mass	Staurolite		Biotite		Muscovite		Ilmenite	Quartz		Monazite	
		Av.	SD	Av.	SD	Av.	SD	nv16a10	Av.	SD	Av.	SD
n:		6		6		6		1	3		4	
Crater diameter (μm):		60		60		60/30		40	60		10	
Li	7	230	16	70	5	6·8	0·6	<1·46	6	3	9	1
B	11	<13		<6·9		40	4	<17·43	<23		<107	
Na	23	8	7	3000	148	14000	1380	12	5	3	<21	
Mg	26	10800	274	58000	2568	3700	565	603	<50		<211	
Al	27	320000	16014	118000	4653	210000	19694	106	29	4	600	416
Si	29	Standard		Standard		Standard		1510	Standard		<8881	
P	31	<40		25	6	35	6	<48	<62		Standard	
Ca	42	<558		<278		<500		<660	<732		5600	573
Ti	49	3000	363	8600	587	1900	169	Standard	<16		<83	
Cr	53	240	60	150	11	130	27	90	<32		<157	
Mn	55	340	18	120	42	<49		1626	<3·9		60	34
Co	59	76	3	63	3	1·8	0·5	39	<0·42		<4·2	
Ni	61	78	8	280	37	<93		<54	<56		<644	
Zn	66	3100	144	60	11	3	1	103	<4·9		<32	
Rb	85	<0·3		800	50	260	34	<0·29	<0·41		<3·3	
Sr	88	<0·1		2	1	140	14	1·7	<0·16		2500	348
Y	89	<0·11		0·3	0·2	<0·33		<0·12	<0·19		6600	879
Zr	90	<0·4		6	8	0·22	0·05	0·9	<0·46		<2·9	
Nb	93	0·7	0·9	20	4	10	2	407	<0·23		<1·6	
Cs	133	<0·11		40	10	1·3	0·2	<0·08	<0·13		<1·9	
Ba	137	<1·1		360	32	900	101	1·1	<0·85		<24	
La	139	<0·12		<0·07		<0·45		<0·15	70	66	148000	7516
Ce	140	<0·1		0·12	0·06	<0·58		0·06	0·02	0·01	270000	25329
Pr	141	<0·08		<0·06		<0·53		<0·10	<0·11		26000	1482
Nd	146	<0·58		<0·50		<3·2		<0·38	<0·70		98000	7654
Sm	147	<0·70		<0·46		<3·2		<0·50	<0·70		18000	1835
Eu	153	<0·24		<0·17		<1·2		<0·13	<0·20		3400	275
Gd	157	<0·79		<0·72		<5·3		<0·55	<0·77		12000	1084
Tb	159	<0·12		<0·09		<0·75		<0·08	<0·11		1400	135
Dy	163	<0·56		<0·52		<1·9		<0·59	<0·40		4000	460
Ho	165	<0·18		<0·11		<0·86		<0·09	<0·11		310	37
Er	166	<0·46		<0·44		<1·9		0·03	<0·41		290	31
Tm	169	<0·19		<0·14		<0·38		<0·09	<0·17		11	2
Yb	173	<0·93		<0·79		<4·3		<1·26	<0·97		28	6
Lu	175	<0·21		<0·14		<0·83		<0·11	<0·19		<5·0	
Hf	178	<0·63		<0·45		<4·4		0·1	0·08	0·03	<23	
Ta	181	<0·17		0·9	0·2	0·6	0·2	43	<0·20		<5·6	
Pb	208	<0·92		9·8	0·5	46	3	<1·20	<1·4		1200	158
Th	232	<0·19		0·08	0·04	<0·70		0·1	0·02	0·01	42000	7183
U	238	<0·11		0·10	0·08	<0·58		0·3	<0·17		5100	681

larger than that of muscovite. Biotite also contains considerably larger amounts of Rb (800 vs 260 ppm) and Cs (40 vs ~1 ppm), and is richer in all analyzed transition elements. With the exception of Ce, the REE are present in concentrations that are below the detection limits of the LA-ICP-MS method used (Table 7).

Muscovite also has the same composition in multiple samples, and in different textural settings. It contains only ~0·1 Mg + Fe atoms p.f.u., and Ca was not detected (Table 7), but it is relatively rich in Na_2O (~2 wt %). The sum of all alkali-site cations ranges from 0·86 to 0·97 p.f.u., yielding a value of 0·26–0·28 for Na/(Na + K + Ca). In addition to tourmaline, muscovite is the only phase in thin section Leit 8 g that hosts B. Its B content (40 ± 4 ppm) is almost identical to that of the host rock (39 ± 7 ppm), implying that most of the rock's B occurs in muscovite (modal abundance: 40–50 vol. %) and not in tourmaline. Compared with biotite, muscovite is considerably richer in Sr (140 ppm vs 2 ppm) and Ba (900 ppm vs 360 ppm), and contains four times more Pb. No REE were detected in muscovite.

The EPMA data for staurolite in Table 6 are averages of randomly selected crystals from two thin sections. Staurolite is not compositionally zoned and displays no appreciable crystal-to-crystal variations in composition. It has an Mg/(Mg + Fe) value of 0·2, and is relatively rich in ZnO (0·36 wt %). Moreover, the LA-ICP-MS data show that staurolite contains >200 ppm Li, the highest Li content of all studied phases (Table 7). It also hosts considerable amounts of Cr (240 ppm), and ~80 ppm each of Co and Ni. No other trace elements were detected by LA-ICP-MS.

Kyanite contains minor Fe (FeO_{tot} = 0·18 ± 0·05 wt %, n = 32) and Cr_2O_3 (0·07 ± 0·04 wt %). No LA-ICP-MS data are available for kyanite.

Ilmenite contains minor amounts of MnO and MgO (Table 6). The LA-ICP-MS results also revealed the presence of ~100 ppm Cr and Zn, ~400 ppm Nb, and ~40 ppm Co and Ta. No REE were detected.

Plagioclase is chemically homogeneous within a given sample, but exhibits distinct compositions in different hand specimens, ranging from albite (An_7) in samples Leit 400 and Leit 400a to oligoclase (An_{15}) in samples Leit 1 and Leit 10 (Table 6).

Chlorite is intermediate in composition, exhibiting an Mg/(Fe + Mg) value of ~0·5 (Table 6).

Quartz is virtually pure, with only trace amounts of Li (~6 ppm) and Al (~30 ppm).

Accessory minerals

Monazite contains ~2 wt % Y_2O_3 when enclosed in garnet, but typically <1 wt % when it occurs in the matrix. It hosts >5000 ppm of U and Ca, as well as ~2500 ppm Sr and ~1200 ppm Pb (Tables 7 and 8). The ThO_2 content ranges from 3 to 5 wt %, but some matrix crystals display an overgrowth characterized by higher concentrations (~7 wt %). The chondrite-normalized REE pattern (not shown) exhibits the pronounced LREE enrichment typical of monazite, with $(La/Yb)_{CN}$ = 3702. The REE pattern further displays a marked negative Eu anomaly (Eu/Eu* = 0·68), which is similar to that of the host rock (Table 1). When normalized to the host rock, the REE pattern is almost flat for the LREE, decreasing sharply towards the HREE (Fig. 14).

Xenotime contains high concentrations of HREE, as determined by EPMA (Table 8; no LA-ICP-MS data available). It displays a typical HREE-enriched chondrite-normalized pattern (not shown). When normalized to the bulk-rock composition, the REE pattern increases from ~800 for Gd to ~8000 for Ho, Er and Lu (Fig. 14).

Zircon is relatively rich in HfO_2 (~2 wt %) and contains up to 0·3 wt % Y_2O_3 (Table 8).

OXYGEN ISOTOPE COMPOSITION

Major minerals

The $\delta^{18}O$ values decrease in the order quartz, staurolite, muscovite, biotite, and garnet, reflecting a tendency towards equilibrium isotope fractionation between the minerals (Table 9). The average values display small standard deviations for all phases, except for staurolite (0·4‰). The reasons for the variability of $\delta^{18}O$ in staurolite are not known. Because all oxygen isotope data represent values obtained from hand-picked mineral separates, no information in regard to possible heterogeneity of $\delta^{18}O$ in staurolite is available.

Tourmaline

The average bulk $\delta^{18}O$ value for six randomly selected tourmaline separates was determined at 7·3 ± 0·3‰ (Table 9).

To analyze the oxygen isotopic composition of single growth zones in tourmaline, we extracted oxygen gas from separates of each zone. The average $\delta^{18}O$ value for the core is well constrained by two analyses from two crystals (Table 10). The inner rims of two crystals exhibit statistically identical $\delta^{18}O$ values (crystals C and P), similar to those of inner rim B2. The values obtained for the other two crystals (B1 and D1), however, are higher (Table 10). For two crystals, $\delta^{18}O$ values are available for both core and IR: in the case of crystal C, the values are identical, whereas the inner rim of crystal B2 has a lower $\delta^{18}O$ than the core. On average, the oxygen isotopic compositions of core and IR are similar, if not identical (6·4‰ vs 6·5 ± 0·4‰).

The average oxygen isotope composition of the OR is relatively poorly constrained, as the two available analyses differ by ~0·9‰ (Table 10). However, when comparing

Table 8: Average compositions (EPMA data) and oxygen-normalized formulae of monazite, xenotime, and zircon occurring in the metapelites at Campolungo (microprobe sections from sample Leit 8)

Mineral:	Monazite	Monazite (low-Th)	Monazite (high-Th)	Monazite[1]	Xenotime[2]	Xenotime	Zircon	Zircon	Zircon	Zircon	Zircon	Zircon
Grain:	Mon1	Mon2	Mon2	Mona5	Xeno5	Xeno2						
Host:	Garnet	Muscovite	Muscovite	Garnet	Garnet	Garnet	Biotite	Muscovite	Garnet	Quartz	Kyanite	Ilmenite
Section:	Leit 8g	Leit 8g	Leit 8g	Leit 8c	Leit 8c	Leit 8c	Leit 8g/8c	Leit 8g/8c	Leit 8g/8c	Leit 8g/8c	Leit 8g/8c	Leit 8g/8c
n:	2	41	11	8	5	2	12	45	34	6	3	3
SiO_2	0·44	0·46(6)	0·4(1)	0·8(3)	n.a.	n.a.	32·3(5)	32·1(2)	32·2(4)	32·0(2)	32·02(4)	32·2(1)
P_2O_5	29·9	29·4(2)	30·3(3)	29·4(5)	35·8(1)	35·7	n.a.	n.a.	n.a.	n.a.	n.a.	n.a.
CaO	0·6	0·7(1)	1·5(4)	0·66(8)	n.a.	n.a.	n.a.	n.a.	n.a.	n.a.	n.a.	n.a.
Fe_2O_3	n.a.	n.a.	n.a.	n.a.	1·5(2)	2·3	0·9(1)	0·1(1)	1·4(1)	0·39(9)	0·93(7)	0·92(2)
Y_2O_3	2·4	0·8(1)	0·5(2)	1·9(2)	48·2(3)	47·0	0·1(1)	0·2(1)	0·3(1)	0·12(5)	0·04(1)	0·16(2)
ZrO_2	n.a.	n.a.	n.a.	n.a.	n.a.	n.a.	65·8(7)	65·6(5)	65·4(7)	65·8(7)	65·6(7)	65·2(4)
La_2O_3	14·3	14·6(4)	12(1)	14·4(2)	n.a.	n.a.	n.a.	n.a.	n.a.	n.a.	n.a.	n.a.
Ce_2O_3	29·2	29·4(9)	26(1)	28·5(7)	n.a.	n.a.	n.a.	n.a.	n.a.	n.a.	n.a.	n.a.
Pr_2O_3	3·06	3·1(1)	3·0(1)	3·0(1)	n.a.	n.a.	n.a.	n.a.	n.a.	n.a.	n.a.	n.a.
Nd_2O_3	11·92	12·0(5)	12·8(7)	12·0(3)	n.a.	n.a.	n.a.	n.a.	n.a.	n.a.	n.a.	n.a.
Sm_2O_3	2·0	2·0(1)	2·9(5)	2·12(9)	n.a.	n.a.	n.a.	n.a.	n.a.	n.a.	n.a.	n.a.
Eu_2O_3	0·12	0·02(3)	0·1(1)	n.a.	n.a.	n.a.	n.a.	n.a.	n.a.	n.a.	n.a.	n.a.
Gd_2O_3	1·9	1·5(1)	2·2(5)	1·5(2)	0·75(4)	0·86	n.a.	n.a.	n.a.	n.a.	n.a.	n.a.
Tb_2O_3	n.a.	n.a.	n.a.	n.a.	0·32(2)	0·30	n.a.	n.a.	n.a.	n.a.	n.a.	n.a.
Dy_2O_3	n.a.	n.a.	n.a.	n.a.	5·1(1)	4·62	n.a.	n.a.	n.a.	n.a.	n.a.	n.a.
Ho_2O_3	n.a.	n.a.	n.a.	n.a.	1·39(4)	1·34	n.a.	n.a.	n.a.	n.a.	n.a.	n.a.
Er_2O_3	n.a.	n.a.	n.a.	n.a.	3·8(1)	4·21	n.a.	n.a.	n.a.	n.a.	n.a.	n.a.
Yb_2O_3	n.a.	n.a.	n.a.	n.a.	2·5(4)	3·7	n.a.	n.a.	n.a.	n.a.	n.a.	n.a.
HfO_2	n.a.	n.a.	n.a.	n.a.	n.a.	n.a.	1·8(2)	1·8(3)	1·5(2)	1·9(1)	1·97(8)	1·8(2)
ThO_2	3·2	4(1)	7(1)	3·6(2)	n.a.	n.a.	0·02(1)	0·04(2)	0·06(3)	0·04(4)	0·01(1)	0·06(4)
UO_2	0·60	0·6(2)	1·0(3)	0·7(1)	n.a.	n.a.	0·02(4)	0·01(1)	0·06(2)	<0·01	<0·01	0·11(9)
Total	99·6	98·9	99·2	98·6	99·4	100·1	100·9	99·8	100·8	100·3	100·6	100·4
Oxygens	4	4	4	4	4	4	4	4	4	4	4	4
Si	0·017	0·018	0·017	0·032			0·987	0·991	0·984	0·986	0·983	0·989
P	0·987	0·987	1·002	0·980	0·989	0·984						
Ca	0·026	0·031	0·062	0·028								
Fe^{3+}					0·037	0·057	0·020	0·003	0·031	0·009	0·022	0·021
Y	0·049	0·016	0·011	0·040	0·838	0·815	0·002	0·002	0·004	0·002	0·001	0·003
Zr							0·980	0·989	0·976	0·989	0·983	0·976
La	0·206	0·214	0·169	0·209								
Ce	0·417	0·427	0·367	0·411								
Pr	0·044	0·045	0·042	0·043								
Nd	0·166	0·169	0·179	0·169								
Sm	0·027	0·028	0·039	0·029								
Eu	0·002	0·000	0·002	0·000								
Gd	0·025	0·019	0·029	0·020	0·008	0·009						
Tb					0·003	0·003						
Dy					0·054	0·049						
Ho					0·014	0·014						
Er					0·039	0·043						
Yb					0·025	0·037						
Hf							0·016	0·015	0·013	0·016	0·017	0·016
Th	0·029	0·039	0·063	0·032			0·000	0·000	0·000	0·000	0·000	0·000
U	0·005	0·006	0·009	0·006			0·000	0·000	0·000			0·001
ΣCations	2·000	1·998	1·990	1·999	2·007	2·011	2·006	2·001	2·009	2·003	2·006	2·006
ΣREE	0·936	0·918	0·838	0·921	0·981	0·970	0·002	0·002	0·004	0·002	0·001	0·003

Values in parentheses are standard deviations (σ_{n-1}) of the average and apply to the last digit. n.a., not analyzed.
[1]Coexists with Xeno5 (see Fig. 5b).
[2]Coexists with Mona5 (see Fig. 5b).

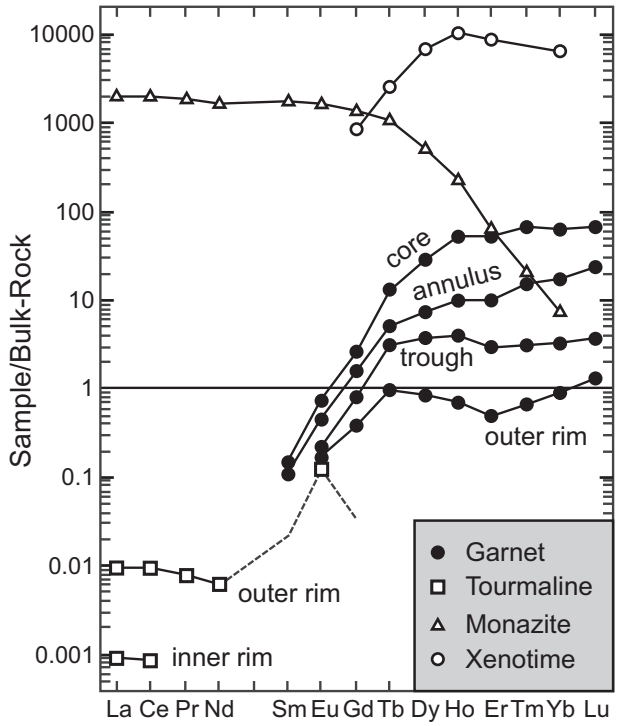

Fig. 14. Bulk-rock normalized REE patterns for the main REE carriers in sample Leit 8. LA-ICP-MS data for crystals from thin section Leit 8g, except for xenotime (Leit 8c, EPMA data for crystal Xeno5, which coexists with monazite; data from Table 8). Dashed lines connect to detection limits of elements that were not detected (no symbol shown).

Table 9: Average $\delta^{18}O$ values (in per mil VSMOW) for major minerals in the tourmaline-rich metapelite from Campolungo

Mineral	$\delta^{18}O$	σ_{n-1}	*n*
Quartz	8·86	0·15	10
Muscovite	6·13	0·15	5
Biotite	5·17	0·15	4
Staurolite	6·15	0·40	7
Garnet	5·02	0·21	7
Tourmaline*	7·34	0·30	6

*Data represent bulk value for tourmaline.

the inner and outer rims of a single crystal (D1), it is evident that the OR is characterized by a distinctly higher $\delta^{18}O$ (7·7‰ vs 6·9‰).

In summary, the average $\delta^{18}O$ values determined for the core and the IR are very similar, whereas those obtained for the OR are considerably higher.

Table 10: $\delta^{18}O$ values (in per mil VSMOW) for single growth zones in tourmaline

Zone and crystal	$\delta^{18}O$	Average $\delta^{18}O$	σ_{n-1}
Core			
Average (crystals B2 and C)		6·35	
B2	6·48		
C	6·22		
Inner rim			
Average (all crystals)		6·50	0·38
B1	7·02		
B2	6·07		
C	6·22		
C	6·43		
C	6·36		
C	6·26		
Average (crystal C)		6·32	0·10
D1	6·86		
D1	6·91		
Average (crystal D1)		6·89	
P	6·85		
P	5·97		
Average (crystal P)		6·41	
Outer rim			
Average (crystals D1 and X)		7·23	
D1	7·67		
X	6·78		

The upper-case letters refer to separate crystals.

DISCUSSION

Bulk-rock composition

The chemical composition of clastic sedimentary rock suites exhibits major variations owing to changes in grain size (e.g. Roser & Korsch, 1986, 1988). It reflects predominantly the nature and proportion of their detrital components and thus, their provenance (e.g. Roser & Korsch, 1986). Because the composition of the source rocks is a function of tectonic setting, the tectonic evolution of a depositional basin may be reconstructed using the chemical composition of the clastic sedimentary rocks (e.g. Roser & Korsch, 1986, 1988; Cullers, 2000; Cullers & Podkovyrov, 2000; Shao *et al.*, 2001). Provenance can also be inferred from the abundance and ratio of certain trace elements. For example, the relative distribution of trace elements with fairly low mobility during sedimentary and diagenetic processes, and with different concentrations in silicic and basic source rocks, has been used to infer the relative contributions of silicic and basic sources in shales and sandstones (e.g. Bhatia & Crook, 1986;

Slack & Stevens, 1994; Cullers, 2000). Similarly, relative REE patterns and the extent of the Eu anomaly have been used to infer sources of sedimentary rocks (e.g. Wronkiewicz & Condie, 1987).

On a global scale, mudrocks reflect the average composition of the upper continental crust (UCC; see Taylor & McLennan, 1985). Most mudrocks, however, form in restricted sedimentary basins, and their compositions thus reflect adjacent source rocks (Cox & Lowe, 1995). For example, incompatible elements such as LREE and Th are more concentrated in silicic than in basic igneous rocks, whereas other trace elements (e.g. Sc, Cr, Co) are more enriched in basic igneous rocks, so their abundances and ratios have been used for determinations of provenance and tectonic setting of sedimentary rocks (Cullers, 1994*a*, 1994*b*, 2000; Mongelli *et al.*, 1996; Nyakairu & Koeberl, 2001). The chemical signature of the source rock, however, may be modified by processes such as weathering at the source, hydraulic sorting during transport, and diagenesis or metamorphism, which both also obscure or destroy the original detrital mineralogical composition (Cullers *et al.*, 1987; Crichton & Condie, 1993; Condie *et al.*, 1995; Cox & Lowe, 1995; Nesbitt *et al.*, 1996). On the other hand, chemical characteristics of provenance may survive metamorphism as high as amphibolite grade (Roser & Korsch, 1988).

Although the Campolungo metapelites display many characteristics of shales, including B content and Eu anomaly, they are enriched in certain elements, notably the LREE and Th, and are markedly depleted in Ca relative to NASC (Figs 6 and 7). A similar Ca depletion has also been reported for other argillaceous rocks (Wronkiewicz & Condie, 1987; Saleemi & Ahmed, 2000; Bhat & Ghosh, 2001) and has been ascribed to selective leaching during weathering, as it is associated in many cases with Na and Sr depletion [see discussion by Wronkiewicz & Condie (1987)]. The Campolungo metapelites do not show a pronounced depletion in Na or Sr relative to NASC (Fig. 6), and the low Ca contents remain to be explained.

Roser & Korsch (1988) developed a method for determining provenance of sandstone–mudstone suites. This method, which is largely independent of grain-size effects, applies a discriminant function using seven major element components and allows for distinction of four sources (Fig. 15a). According to this method, the Campolungo metapelites plot mostly in the field of intermediate igneous provenance (andesite–dacite). Roser & Korsch (1986) have shown further that sandstones, siltstones and mudrocks from different tectonic settings can be distinguished on the basis of their K_2O:Na_2O values and their SiO_2 contents. The K_2O/Na_2O vs SiO_2 discrimination diagram (Fig. 15b) suggests that the argillitic protolith of the Campolungo metapelites was deposited in an active continental margin setting, consistent with trace element data. In the La–Th–Sc tectonic discrimination diagram of Bhatia & Crook (1986) the Campolungo metapelites plot as a tight cluster at the boundary between the fields of active or passive margins and continental arc (Fig. 15c). Using Zr as a plotting variable instead of La (Bhatia & Crook, 1986), the fields of active and passive continental margins are resolved, and all analyzed metapelites fall within the active continental margin field (Fig. 15d). In both trace element plots, the Campolungo metapelites are distinct from the NASC composition, particularly because of their high La (and other LREE) and Th contents (see Figs 6 and 7). An active margin setting for the source rocks is consistent with models proposed for the evolution of the western Tethys realm, specifically during the Permian (Stampfli *et al.*, 2001, fig. 16).

Values of Th/Sc increase with sedimentary maturation and/or supply of evolved (acidic) detritus (Roser *et al.*, 1996). For the Campolungo metapelites, the average values of Th/Sc ($1{\cdot}34 \pm 0{\cdot}07$), La/Sc ($3{\cdot}8 \pm 0{\cdot}2$) and Eu/Eu* ($0{\cdot}63 \pm 0{\cdot}01$) lie within the range of sedimentary material derived from silicic sources (Cullers, 2000), and are very similar to those of tonalitic rocks (Condie & Wronkiewicz, 1990). The REE are preferentially enriched in the finest size fractions of sediments (Taylor & McLennan, 1985), and therefore the REE as well as the size of the Eu anomaly of pelites are representative of the bulk composition of the source (Cullers *et al.*, 1987).

The active continental-margin field has been described as representing continental-margin magmatic arc or uplifted areas associated with strike-slip faults and deposited in pull-apart basins. From the combination of all geochemical characteristics of the studied rocks, we conclude that the protolith of the rocks studied here probably represents material derived from uplifted areas associated with strike-slip faults and deposited in pull-apart basins. Such intramontane basins existed during the late Paleozoic in the region that is now represented by the Helvetic and Lepontine Alps (Trümpy, 1980).

Thermodynamic modeling and metamorphic evolution

P–T *pseudosection modeling*

The metamorphic evolution of the Campolungo metapelites has been modeled in the system Na_2O–K_2O–CaO–MgO–FeO–MnO–TiO_2–Al_2O_3–SiO_2–H_2O, using the bulk-rock composition of sample Leit 8 (Table 1). The water content was set at the amount determined analytically for this sample. The *P–T* diagram shown in Fig. 16 was computed using free energy minimization (PerplexX; see Connolly, 2005) with end-member thermodynamic data from Holland & Powell (1998), and solution models as shown in Table S1 (electronic supplementary material). Andalusite, kyanite, sillimanite, quartz, ilmenite, and rutile were considered as pure phases. Because of the lack of thermodynamic data for tourmaline and because it is

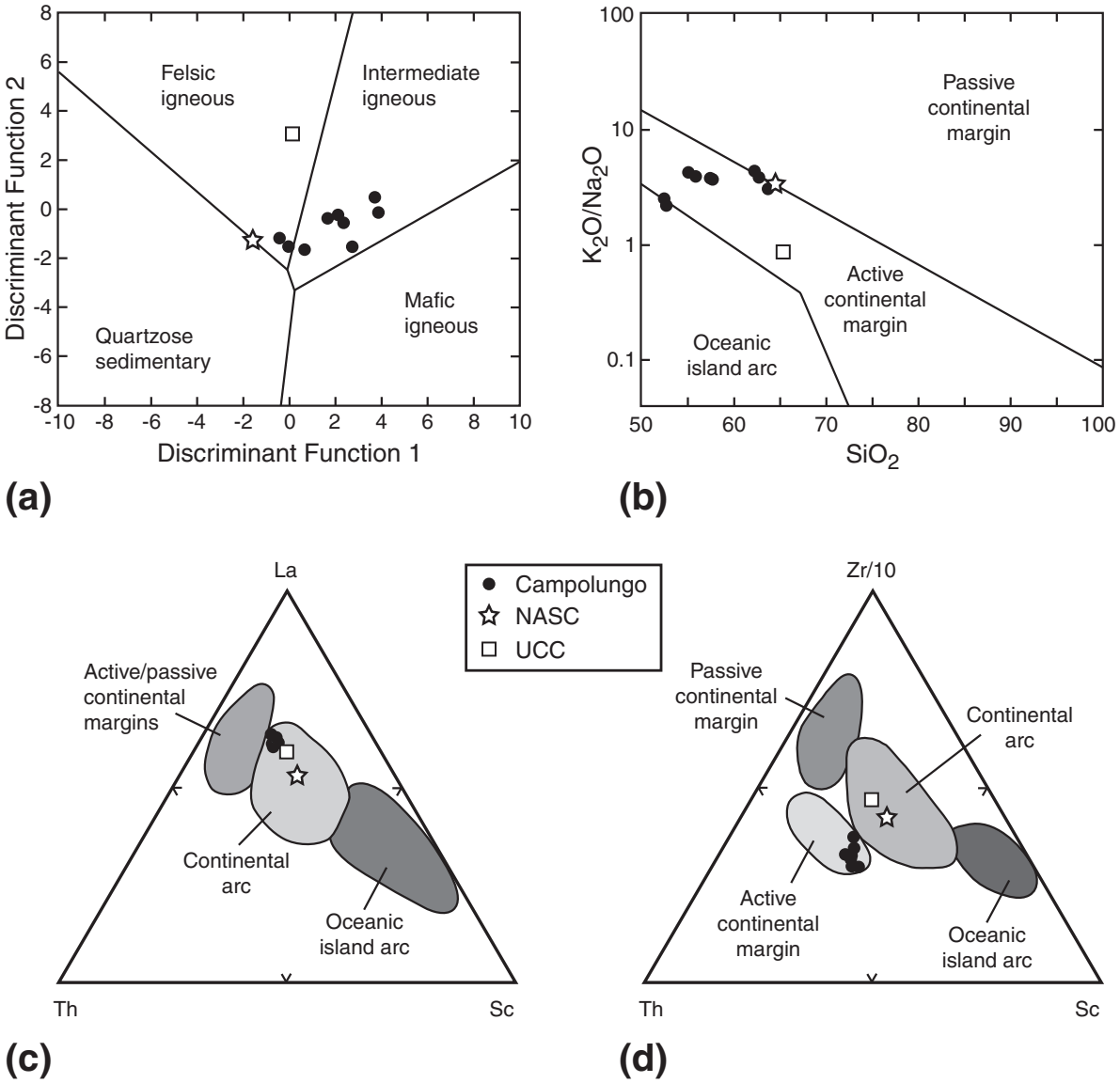

Fig. 15. Bulk-rock composition of the Campolungo metapelites plotted in various discrimination diagrams. (a) The discriminant function diagram for provenance signatures of sandstone–mudstone suites using the seven major element oxides Al_2O_3, TiO_2, Fe_2O_3 (total Fe), MgO, CaO, Na_2O, and K_2O (after Roser & Korsch, 1988). (b) The K_2O/Na_2O vs SiO_2 diagram for tectonic discrimination of sandstone–mudstone suites (after Roser & Korsch, 1986). The components are plotted in wt % (recalculated on 100 wt % volatile-free). (c) The La–Th–Sc tectonic discrimination diagram for clastic sediments (Bhatia & Crook, 1986). (d) The Zr/10–Th–Sc tectonic discrimination diagram for clastic sediments (Bhatia & Crook, 1986). NASC, North American Shale Composite; data from Condie (1993). UCC, average Upper Continental Crust; data from Taylor & McLennan (1985).

the only B-rich mineral in the rock, the phase was not considered. To illuminate the evolution of the model system, modal abundances (Fig. 17) and compositions (Fig. 4D, electronic supplementary material) of the stable phases were extracted along the path indicated on the P–T phase diagram section (Fig. 16). The starting point of the P–T path (point A: 462°C, 4·7 kbar) was chosen to match the spessartine and pyrope contents of the garnet core (Figs 12 and Fig. 4S; Table 4). The path was further constrained to be consistent with the occurrence of kyanite (appearing above ~660°C and >7·1 kbar) and retrograde staurolite as well as with the absence of retrograde plagioclase in this sample.

At the starting point of the P–T path (point A in Fig. 16), the phase diagram section predicts that garnet, staurolite, chloritoid, biotite, ilmenite, and two white micas should be stable. One of the white micas, paragonite, breaks down at ~550°C and ~6·4 kbar, *c.* 50°C higher than the

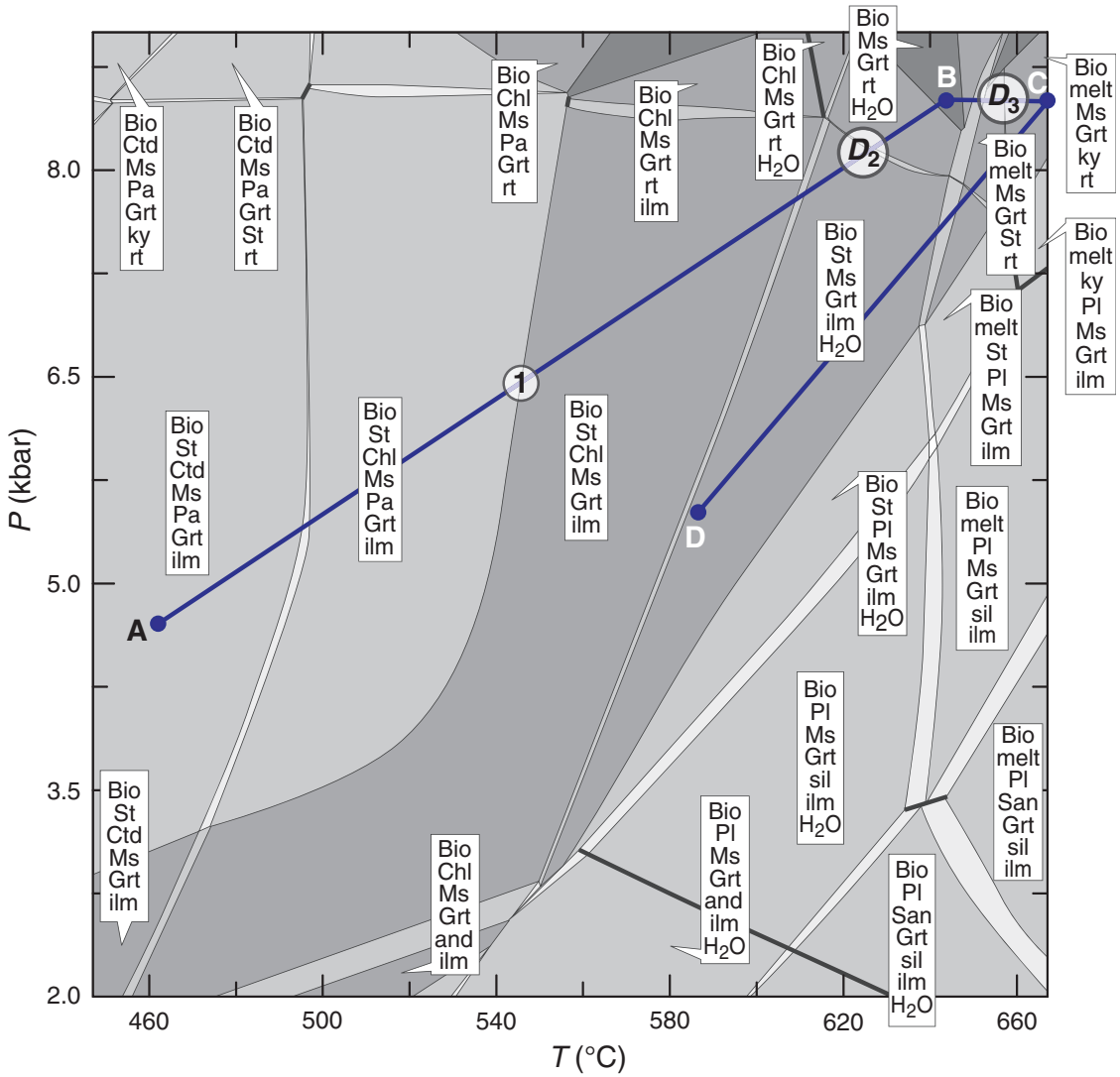

Fig. 16. Phase diagram section calculated for the bulk-rock composition of sample Leit 8 and showing the P–T path selected for the modeling of the metamorphic evolution of the Campolungo rocks. Conditions for points along the P–T path are: A: 462°C, 4·7 kbar; B: 644°C, 8·5 kbar; C: 667°C, 8·5 kbar; D: 587°C, 5·5 kbar. Point 1 marks the conditions inferred for the allanite-to-monazite reaction and formation of the Ca-rich annulus in garnet. Bio, biotite; Chl, chlorite; Ctd, chloritoid; Grt, garnet; Ms, muscovite; Pa, paragonite; Pl, plagioclase; San, sanidine; St, staurolite; and, andalusite; ilm, ilmenite; ky, kyanite; qtz, quartz; rt, rutile; sil, sillimanite. Lower-case abbreviations indicate that the minerals have been treated as pure phases. Solution models of the other phases are given in Table S1 (electronic supplementary material). Shading indicates degree of variance: light shades have a lower variance than dark shades. Bold continuous lines represent univariant reactions.

disappearance of chloritoid (Fig. 16). At 540°C and 6·28 kbar, just prior to its disappearance, paragonite has an X_{Na} of 0·864 and an X_{Ca} of 0·041 (approximately twice the calculated Ca content of coexisting muscovite). This relatively high Ca content is redistributed throughout the assemblage during paragonite breakdown. The analyzed pyrope content of the Ca-rich annulus in garnet ($X_{prp} = 0{\cdot}10$–$0{\cdot}12$; see Fig. 12a, Table 4) is consistent with formation at ~550°C and ~6·5 kbar, coinciding with paragonite breakdown (Figs 16, 17 and 4S). Therefore, we tentatively interpret the sharp increase in X_{grs} observed at the annulus as having resulted in part from the increased availability of Ca owing to the disappearance of paragonite. Calculations suggest that muscovite, on the other hand, continues to grow through this part of the P–T path (Fig. 17), with Na-rich compositions (Fig. 4S) agreeing well with EPMA data (Table 6).

After the disappearance of chlorite at ~610°C and ~7·8 kbar, growth of considerable amounts of garnet and muscovite at the expense of biotite and staurolite is predicted (Fig. 17). Rutile growth at the expense of ilmenite also occurs. A major phase of garnet growth is predicted

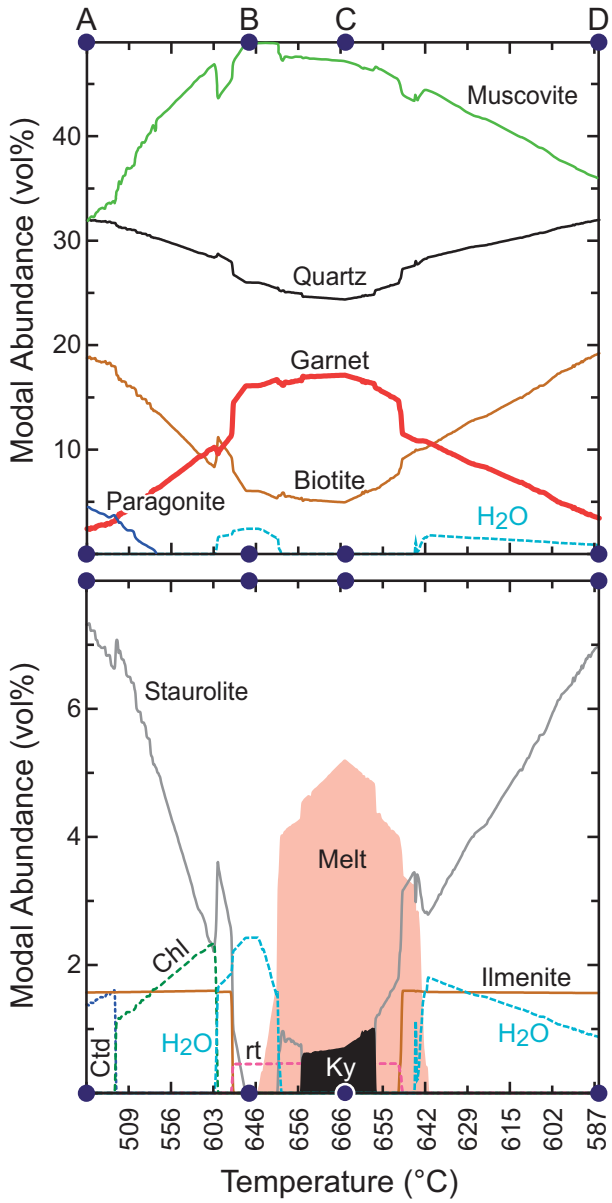

Fig. 17. Diagram showing the evolution of the modal abundance (in vol. %) of the main phases as calculated along the P–T path shown in Fig. 16. Abbreviations as in Fig. 16.

at ~8·1 kbar and ~630°C, in excellent agreement with the oxygen isotope equilibration temperature obtained from garnet–quartz pairs using the latest fractionation coefficients (see Table 11). In combination with the thin-section observations (Fig. 4), we interpret this event to represent the syn-D_2 mineral growth.

The production of small amounts of melt (4–5 vol. %; see Fig. 17) is predicted at ~650°C and 8·5 kbar (between points B and C, Fig. 16). The temperature of subsequent kyanite formation (~660°C) is almost independent of P within the range of ~7·7–8·7 kbar (Fig. 16), and we interpret these conditions (~660°C, ~8·5 kbar) as representing D_3 (thin-section observations indicate that kyanite crystallizes during or after D_3; Figs 3e and 4). The observed textural relationships (e.g. Fig. 2a and b) further suggest that both the OR of tourmaline and crack-filling staurolite crystallize after D_3 (Fig. 4). Average $\delta^{18}O$ compositions of the OR of tourmaline and quartz yield an equilibrium fractionation temperature of either 708°C or 627°C, depending on the choice of fractionation coefficients (Table 11). Staurolite growth is predicted to occur early in the retrograde history of the inferred P–T path (~660°C and ~8·2 kbar) at the expense of kyanite (Fig. 17). This event is followed by formation of ilmenite from rutile, consistent with observed ilmenite rims around matrix rutile grains (Fig. 3g). The inferred retrograde P–T path then exits the melt stability field (Figs 16 and 17), and whereas muscovite is partially consumed, biotite continues to grow. This late-stage biotite is recorded texturally as cross-biotite. Staurolite continues to grow until the end of the path at 5·5 kbar and 587°C (point D in Figs 16 and 17), consistent with the oxygen isotope equilibration temperature calculated from staurolite–quartz pairs using the Zheng (1993*a*, 1993*b*) fractionation coefficients (Table 11). Temperature calculated with the coefficients of Richter & Hoernes (1988) seems unrealistically high in this case. Continuation of the path to lower P and T would result in retrograde chlorite (subject to the availability of water), in agreement with the thin-section observations. Extrapolating the path even further (using the same dP/dT) would yield a pressure of ~2 kbar at 500°C, which is consistent with estimates for the development of the assemblage tremolite + calcite in late (syn- to post-D_4) veins within dolomite marbles of the Campolungo area (Mercolli *et al.*, 1987).

Previous thermobarometric calculations using fluid-conserving multi-equilibria (based on thin section Leit 8c) yielded a well-defined P–T estimate at 7·5 ± 0·4 kbar and 643 ± 11°C (Engi *et al.*, 1995; Todd & Engi, 1997), which has been interpreted as representing the thermal peak of the Alpine metamorphism (P at T_{max}). Similarly, an oxygen isotope equilibration temperature of ~630°C, obtained for other metapelites from Campolungo (containing magnetite), has been interpreted as T_{max} of the Alpine metamorphism (Hoernes & Friedrichsen, 1980). These conditions agree relatively well with our data, but fall slightly below the temperature of the field of kyanite stability predicted here. Indeed, our oxygen isotope equilibration result mirrors that of Hoernes & Friedrichsen (1980) extremely well, but we interpret this as representing the thermal conditions accompanying garnet growth during D_2 rather than the subsequent maximum temperature achieved. The previous temperature estimate of 643 ± 11°C lies between our estimates for

Table 11: Oxygen isotope equilibrium fractionation temperatures (°C), calculated using different calibrations

Quartz–biotite	Quartz–muscovite	Quartz–staurolite	Quartz–tourmaline	Quartz–garnet	Mineral–mineral oxygen isotope fractionation coefficients from
610	571	587	708*	629†	Zheng (1993*a*, 1993*b*)
627	625	725		600	Richter & Hoernes (1988)
657	541				Javoy (1977)
	682				Hoffbauer *et al.* (1994)
			627*		Kotzer *et al.* (1993)
				596	Bottinga & Javoy (1973)
				628	Sharp (1995)
				636	Rosenbaum & Mattey (1995)

*Outer rim.
†Isotope fractionation coefficients used are those for almandine.

the mineral assemblages formed during D_2 and D_3. The presence of both rutile and kyanite in the samples studied here yields a higher P estimate than that of Engi *et al.* (1995), although the absolute maximum pressure is difficult to constrain here. On the basis of piezobarometric observations, Rosenfeld (1969) determined a pressure of >8 kbar at an estimated 600°C for the growth of garnet in the Campolungo metapelites; this estimate is consistent with garnet growth during D_2, as calculated here. Our P and T estimates for D_2 and D_3 also agree well with those derived from similar micaschists occurring near Campolungo in another part of the Simano nappe (Rütti *et al.*, 2005) as well as in a comparable structural setting ~10 km further to the west (Galli *et al.*, 2007).

Pelitic sediments usually contain considerable amounts of B because of concentration in clay minerals, particularly illite [see discussion by Sperlich *et al.* (1996)]. With increasing metamorphic grade, B is released during recrystallization or breakdown of illite and white mica, becoming available for tourmaline growth. Rocks that originally contained abundant illite tend to produce tourmaline during prograde metamorphism. As the B contents of the studied metapelites are within the range of typical argillaceous sedimentary rocks (see above) and most of the B is now present in muscovite, we conclude that no external B source was needed for tourmaline growth. Instead we propose, in agreement with Sperlich *et al.* (1996), that the B required to form the large tourmaline cores was derived from the continuous transformation of illite into white mica, probably during D_1. Furthermore, breakdown of paragonite (Fig. 17), calculated here at ~550°C, may have released sufficient B to allow formation of the IR of tourmaline, which thus must have grown at $T > 550$°C. The OR of tourmaline grew after partial resorption of the IR, as documented by the sutured boundary between the two distinct growth zones (Fig. 8). Moreover, textures, such as that shown in Fig. 2b, suggest that the OR of tourmaline grew only after fracturing during D_3. Our calculations indicate that this event occurred at a temperature of ~660°C (Fig. 16) and suggest limited consumption of muscovite at this stage of the history (Fig. 17). Muscovite, however, recrystallized to a certain extent during D_3, as indicated by the pronounced crenulation cleavage that it defines (Fig. 3a). We therefore conclude that partial recrystallization of muscovite during D_3 released sufficient B to allow formation of the OR of tourmaline.

An important remaining question is why tourmaline, a highly refractory phase (Henry & Dutrow, 1996), experienced partial resorption before final growth. Our calculations point to the production of melt, albeit in very small amounts (~5 vol. %; Fig. 17), during this stage of the metamorphic evolution. Whether or not this melt was indeed generated is uncertain and what role it may have played in the resorption is unknown. In the field, the rocks lack visible signs of melt presence, and the study area is outside the Alpine migmatite belt (Fig. 1). The oxygen isotopic composition of the OR of tourmaline (Table 10), however, does indicate that it may have formed at conditions that were considerably different from those prevailing during formation of the IR.

Garnet growth and diffusion

The preceding discussion was based upon equilibrium calculations for a fixed bulk-rock composition, but numerous studies have suggested that the effective bulk-rock composition can change as metamorphism progresses, partly owing to sequestration of components in, or release of components from, zoned phases (e.g. Spear, 1988; Stüwe, 1997). We thus performed a separate set of calculations, predicting the phase proportions grown along a specific P–T path, but removing the components forming garnet after each step in which garnet was stable. The amount and composition of garnet extracted from the bulk-rock at

each step were then used to forward model the garnet zoning that would occur owing to crystal-rim equilibration during prograde burial and heating to the peak conditions inferred above, based upon a spherical crystal geometry. An important assumption of this process is that once garnet was removed from the bulk-rock composition we did not allow its resorption, so periods of staurolite growth at the expense of garnet (e.g. Florence & Spear, 1993), or partial dissolution during decompression, will be poorly represented. Calculations were based upon the same initial bulk-rock composition, thermodynamic data and solid-solution models as those used in the P–T pseudosection modeling (see above), but with additional bulk-rock H_2O (3·38 wt % rather than 2·78 wt %). It was found that addition of more than *c.* 3·4 wt % bulk-rock water inhibits garnet stability (enhancing phyllosilicate stability) at low temperature, where equilibrium garnet compositions are most consistent with measured crystal-core values. Whenever fluid became stable along the prograde or decompression path, we removed it from the bulk-rock composition, retaining the structurally bound H in crystalline phases.

For an appropriate timescale (10 Myr heating and 10 Mry cooling), intracrystalline diffusion across the growing zoned garnet crystal was calculated at each step, again assuming a spherical geometry and using the diffusion data of Carlson (2006). Further information on the garnet growth and diffusion model has been given by Caddick *et al.* (2010). Results (Fig. 18) show the predicted garnet zoning and coexisting phase stabilities, which differ slightly from the P–T pseudosection owing to significant depletion of components (particularly MnO, CaO and FeO) in the effective bulk-rock composition (EBC) once peak conditions are reached. The predicted garnet zoning matches analyzed trends well (Fig. 18a), albeit with lower Fe and higher Mn contents in the modeled crystal core. This small discrepancy may reflect a non-central section (in three dimensions) in the analyzed crystal, an imperfect choice of modeled initial P and T, properties of the underlying thermodynamic mineral solution models, or kinetic factors limiting validity of the assumption of equilibrium growth from a simple bulk-rock composition at the lowest temperatures. The prominent Ca annulus also cannot be reproduced, suggesting that this is at least partly due to reaction kinetics, dissolution of phases not currently modeled (e.g. Spear & Pyle, 2010), or additional processes outside the scope of the current modeling (discussed further below).

For the P–T path of interest, this model predicts generation of a small melt fraction, reaching ~6–7 vol. % melt at the peak temperature (Fig. 18b). This petrologically realistic melt fraction for a pelite at 670°C was controlled by the progressive extraction of water (as a fluid phase) along the preceding prograde path, with the resultant melt composition containing (in molar proportions) approximately 39% H_2O, 49% SiO_2, 6% Al_2O_3 and 5% Na_2O (with minor amounts of CaO, K_2O, FeO and MgO). The melt stability is short-lived (Fig. 18b), with crystallization occurring soon after peak temperature on the path C–D (see P–T path labels in Fig. 16).

Ca-rich annuli and REE zoning

The occurrence of Ca-rich annuli in porphyroblasts of two phases within the same rock is unusual and cannot be reproduced with the simple modeling techniques described above, thus warranting further discussion.

Garnet

The Ca-rich annulus forms a concentric band with distinctly higher concentrations of certain trace elements, including Sr, Y, and HREE (Figs 11 and 12). Similar discontinuous changes in garnet from other localities have been attributed to breakdown or formation of other phases, or open-system interaction with fluids or melts (Hickmott *et al.*, 1987, 1992; Carlson, 1989; Hickmott & Spear, 1992; Schwandt *et al.*, 1996; Spear & Kohn, 1996; Corrie & Kohn, 2008). In their studies of pelitic garnets from the Picuris Range, New Mexico, however, Chernoff & Carlson (1997, 1999) presented convincing arguments against applying such an interpretation universally; most importantly, they observed that even though most garnet crystals (formed at 0·37 GPa and $T_{peak} = 525 \pm 25$°C) exhibited Ca annuli with sharp hexagonal outlines, the chemical composition of these annuli varied widely for different-sized garnets. Specifically, they found a strong correlation between the MnO content of a garnet's core (taken as an index of crystal nucleation time; Carlson, 1989) and the concentrations of MnO, MgO and FeO at the Ca spike in that crystal (shown for MnO in Fig. 19a). Such a relationship would not be expected if the garnet-forming components had achieved equilibrium at the hand-specimen scale (dashed horizontal line in Fig. 19a). Chernoff & Carlson (1997, 1999), thus, concluded that the Ca spikes cannot represent rock-wide event markers in these rocks, because the annuli cannot have formed contemporaneously in all garnets. Rather, those workers interpreted the Ca-rich annuli, which coincide with enrichment in various other trace elements (e.g. Y, Yb), as reflecting the participation of different trace element-enriched phases in the garnet-forming reaction at different times during the reaction history for crystals of different size. At Campolungo, complete core–rim quantitative compositional profiles are available for only two garnet crystals with different sizes and different core MnO contents. This limited dataset demonstrates, however, that the major element composition is almost identical for both Ca annuli, even though the core compositions of the two garnets are distinct (Fig. 19b). Consequently, these data do not lie on the trend of Chernoff & Carlson (1997, 1999),

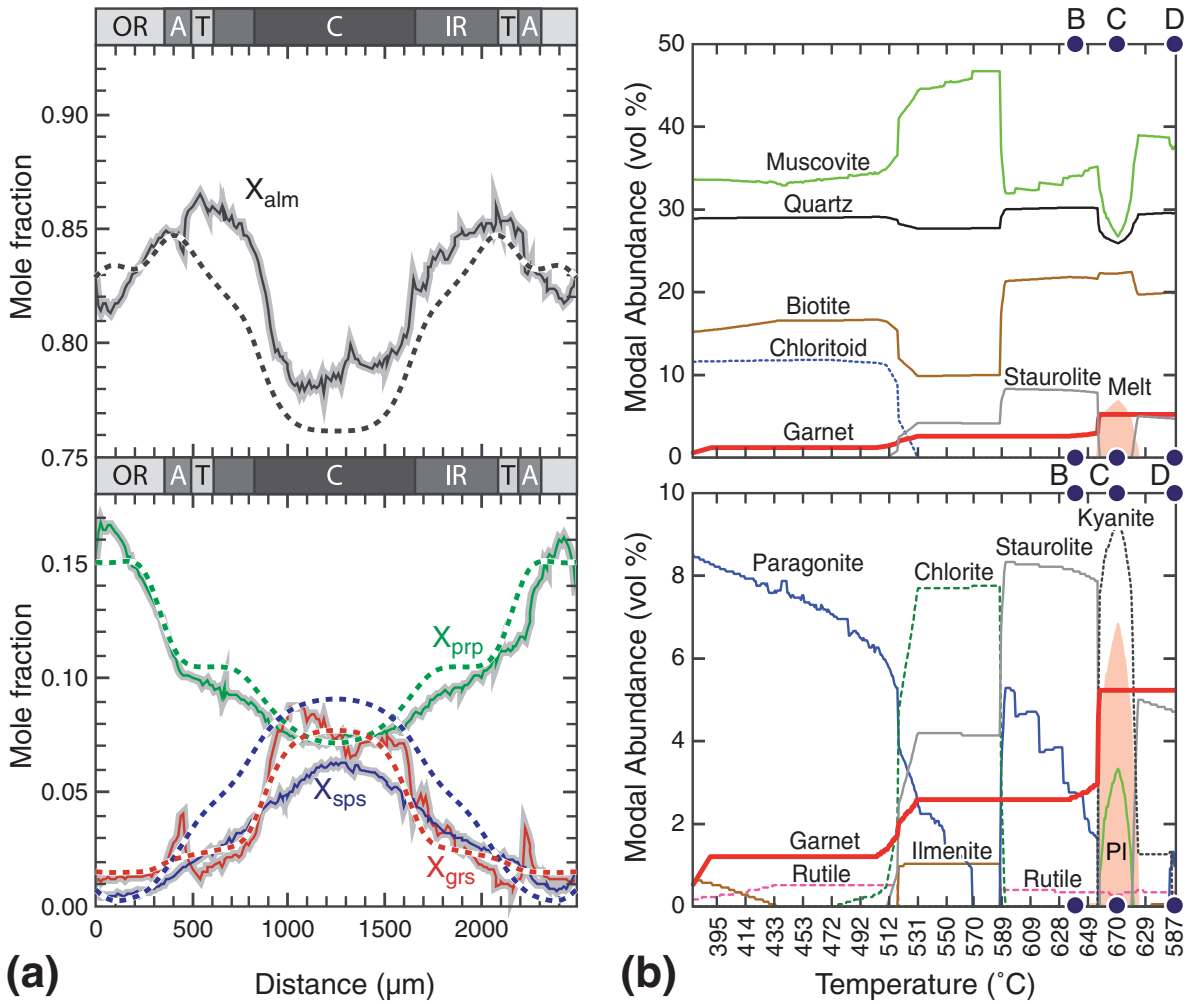

Fig. 18. (a) Comparison of forward-modeled garnet zoning (dashed lines) with an EPMA traverse through a sub-spherical garnet in sample Leit 8 (section Leit 8g; continuous lines with a grey envelope correspond to those shown in Fig. 12a). Model calculated for the starting bulk-rock composition of Leit 8, but allowing for depletion of this initial bulk-rock composition as garnet grew, and for a P–T path involving burial and heating from 377°C at 5·5 kbar to 527°C at 7·5 kbar, and then to points B, C and D, which correspond to those labeled in Figs 16 and 17. An animation of the growth zoning established during this path, and its concomitant diffusive relaxation, is available for downloading as Fig. 5S in the electronic supplementary material. (b) Volume proportion of the calculated coexisting phases along the P–T path for which garnet growth was modeled. The proportion of garnet was calculated by summing the garnet fraction grown over all preceding steps, illustrating how garnet resorption was not permitted in this model. Orange area shows the melt stability field. Pl, plagioclase; alm, almandine; grs, grossular; prp, pyrope; sps, spessartine.

shown schematically for MnO in Fig. 19a, indicating that the Ca spikes could indeed have resulted from a rock-wide event. In this case, the observed enrichment in Sr, Y and HREE in the Ca annuli relative to the adjacent garnet zones can also be due to a rock-wide event.

Yttrium-rich annuli in garnet have also been reported from other garnet- and staurolite-zone metapelites (Lanzirotti, 1995; Chernoff & Carlson, 1999; Pyle & Spear, 1999; Yang & Rivers, 2002; Yang & Pattison, 2006; Corrie & Kohn, 2008). Processes invoked as possibly causing this unusual feature include: (1) changes in the growth rate of garnet; (2) garnet resorption followed by renewed growth; (3) open-system infiltration of a fluid or a melt enriched in Y and other trace elements; (4) breakdown of minerals rich in Y and other trace elements. A substantial change in the abundance of inclusions might indicate mechanism (1) (Lanzirotti, 1995). Element distribution maps for each studied garnet crystal show that the low-Ca trough, just inside the Ca-rich annulus, contains very abundant inclusions of rutile (e.g. Fig. 13). The annulus itself is relatively inclusion-free, which could be explained by a decrease in the rate of garnet growth (Lanzirotti, 1995). This mechanism, however, is difficult to otherwise assess without an explanation for the sudden change in

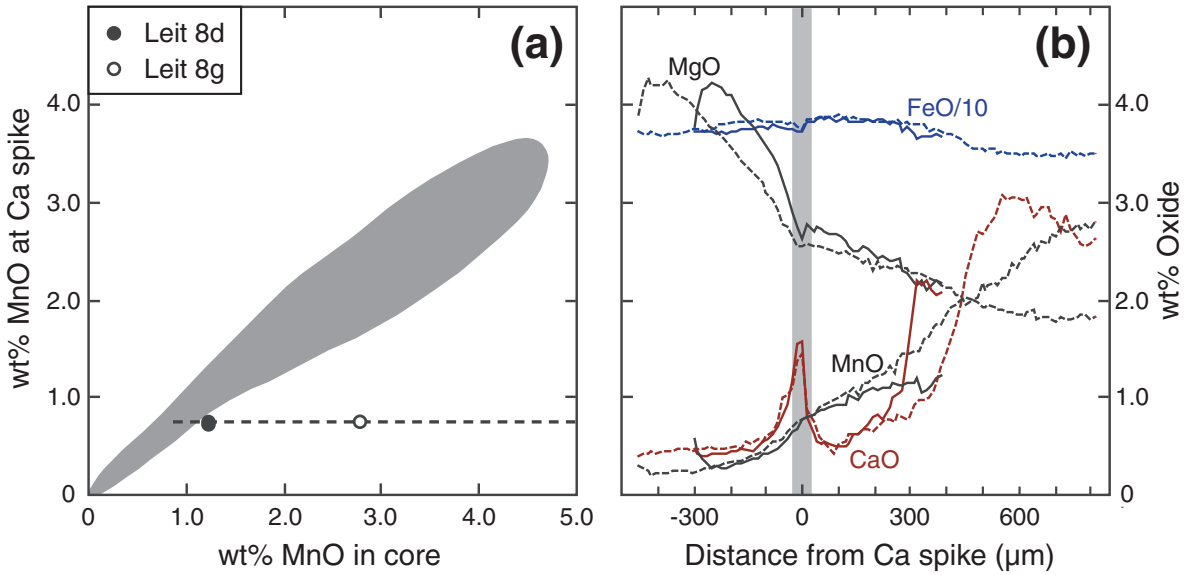

Fig. 19. Comparison of the chemical composition of two garnet crystals of different size. (a) MnO concentrations at Ca spike for two garnet crystals from different thin sections plotted against the MnO content of the respective garnet cores. Data represent two analyses for each of the crystals from sections Leit 8d and Leit 8g. Shaded field shows the analogous data for 178 pelitic garnets from the Picuris Range, New Mexico (data from Chernoff & Carlson, 1997). Dashed line displays the expected relationship for the case of hand-specimen-scale equilibrium and simultaneous formation of the Ca spike in all garnets. (b) Compositional profiles across the same two garnet crystals. Continuous lines are for section Leit 8d; dashed lines are for section Leit 8g. Shaded vertical bar represents the location of the Ca spike in each of the crystals.

growth rate. Annuli preserved in Campolungo garnets exhibit asymmetric concentration profiles, with a steeper slope on the inner side. According to Yang & Rivers (2002), this feature may be indicative of garnet resorption and renewed growth, which would result from a change in the garnet-forming reaction. Similarly, the fact that the annuli do not exhibit a hexagonal shape might also point to an interruption of garnet growth [see discussions by Lanzirotti (1995) and Chernoff & Carlson (1999)]. According to our thermodynamic modeling, however, the Ca-, Sr-, Y-, and HREE-rich annuli of the Campolungo crystals appear to have been formed during a period of continued garnet growth in the temperature range 462–610°C (Figs 16 and 17), so mechanism (2) seems unlikely. Moreover, the annuli are generally subhedral, sometimes having straight outlines (e.g. small crystal in Fig. 9b), and not displaying the embayments on their inner side that would be expected if resorption had preceded renewed garnet growth (Pyle & Spear, 1999; Yang & Rivers, 2002). We therefore suggest that the annuli might indeed represent a zoning feature produced during a hiatus-free garnet growth, as discussed by Lanzirotti (1995) and Chernoff & Carlson (1999).

This conclusion suggests that mechanisms (3) or (4) may have been important in these samples. Both processes are similar in that Y and other trace elements are suddenly available for incorporation into garnet. An additional argument favoring mechanisms (3) or (4) is provided by the REE patterns, especially by the striking sinusoidal REE patterns of both trough and OR (Fig. 10). The proposed mechanisms for the formation of such patterns vary, but all studies agree that garnets with such unusual REE patterns experienced complex evolutions (Shimizu, 1975; Shimizu & Richardson, 1987; Hoal *et al.*, 1994; Stachel *et al.*, 1998; Griffin *et al.*, 1999; Taylor *et al.*, 2003; Zhang *et al.*, 2003; Konrad-Schmolke *et al.*, 2008). Such complex REE patterns in zoned metamorphic garnets can be explained in terms of sequential garnet-producing reactions, which consume major minerals (e.g. chlorite, epidote) in thermodynamic equilibrium with an EBC that is continuously depleted in HREE owing to fractionation into the growing garnet (Konrad-Schmolke *et al.*, 2008). For harzburgitic garnet showing sinusoidal REE patterns, however, it is generally believed that patterns were initially LREE-depleted and subsequently modified by metasomatism through a LREE-enriched fluid. We propose here that the pronounced sinusoidal REE patterns of both the trough and the OR of the Campolungo garnet (Fig. 10) are the result of an attempt by garnet to re-equilibrate with a LREE-enriched medium. The nature of this medium is unknown, but could be either a LREE-rich fluid or melt, or an EBC that has become LREE-enriched through the breakdown of a LREE-rich mineral. Monazite is the only preserved phase with a pronounced LREE-enriched chondrite-normalized pattern. The LREE part of this pattern is parallel to that of the

bulk-rock (Fig. 14). Comparable amounts of LREE and similar REE patterns are typical for allanite (Gieré & Sorensen, 2004), but only one tiny allanite inclusion in garnet was found in the Campolungo samples (Fig. 5a; because of its small size, no quantitative chemical data are available for this allanite). The only other solid phase with detectable, albeit very low, LREE contents is tourmaline (IR and OR; Table 3; Fig. 14). However, tourmaline is an unlikely source of the LREE, because its IR grew contemporaneously with the garnet rim (Fig. 4).

The fact that the annulus in garnet also contains Ca and Sr suggests that it might be related to the breakdown of allanite, which may incorporate large amounts of Sr (Gieré & Sorensen, 2004). Allanite has been shown to break down at 550°C in similar rocks (Janots *et al.*, 2008) from the Lukmanier pass (~12 km north of Campolungo; Fig. 1). Allanite breakdown at lower amphibolite-facies conditions in pelitic schists typically produces monazite (Smith & Barreiro, 1990), forming clusters of anhedral or subhedral monazite grains, which mimic the original shape of the allanite crystals (Wing *et al.*, 2003; Janots *et al.*, 2008). Such monazite aggregates are observed in the matrix of the Campolungo metapelites (Fig. 5e and f), indicating that they may have been formed through allanite breakdown. Moreover, the current generation of monazite contains high amounts of Sr, Ca and Y (Tables 7 and 8), elements that would be released during the allanite breakdown. The allanite breakdown reaction also involves consumption of apatite (Wing *et al.*, 2003; Janots *et al.*, 2008), thus releasing additional Ca and possibly LREE. Because all these elements are enriched in the annulus of garnet, we conclude that the annulus was formed in response to both the allanite-to-monazite reaction and the contemporaneous disappearance of the relatively Ca-rich paragonite (point 1 in Fig. 16). This conclusion is supported by the presence in some garnets of several monazite grains as inclusions at, or near, the Ca-rich annulus (Fig. 5a). Few monazite grains have been observed inside the Ca-rich annulus, with examples coexisting with xenotime (Fig. 5b), suggesting that they may represent detrital grains (no Pb data are available for these grains). Application of the monazite–xenotime thermometer of Gratz & Heinrich (1997) yields 613°C (T_{min} at 8·5 kbar) for the equilibration of the two phases, in general agreement with our modeled peak temperature at this pressure (Fig. 16).

Because garnet incorporates the HREE, Y, Ca and Sr more readily than the LREE and the middle REE (MREE), the Ca-rich annulus exhibits a typical garnet REE pattern (Fig. 10) and displays a distinct enrichment in Y and Sr relative to the adjacent growth zones (Fig. 12b). This more typical garnet REE pattern might be seen to support the hypothesis that mechanism (1) (i.e. decrease in growth rate; see above), caused the development of the pronounced annulus. However, after combining all data and observations, we conclude that mechanism (1) was not the cause of, but may have enhanced, the formation of the annulus in garnet. Later, when the HREE become depleted in the EBC through fractionation during continuous garnet growth (of the OR), the REE pattern changes into a sinusoidal shape, because garnet then attempts to equilibrate with a local environment that has become proportionally enriched in the LREE and MREE.

Similarly, we propose that the sinusoidal pattern of the garnet trough also represents an attempt by garnet to equilibrate with the LREE released through another reaction involving a LREE-rich accessory mineral. It has been shown that in metapelites, detrital grains of monazite are replaced by euhedral allanite during greenschist-facies regional metamorphism (Smith & Barreiro, 1990; Wing *et al.*, 2003). In the Central Alps, this monazite-to-allanite reaction has been inferred to take place upon the appearance of chloritoid at ~450°C (Janots *et al.*, 2008). We therefore conclude that the sinusoidal pattern of the garnet trough was imposed onto garnet by the release of LREE into the EBC during the replacement of detrital monazite by metamorphic allanite. The monazite breakdown reaction also produces apatite (Janots *et al.*, 2008, 2011), consistent with the apatite observed near the IR–trough boundary of some garnet crystals (Fig. 3S, electronic supplementary material).

High Y concentrations and the presence of xenotime inclusions in the garnet core, as well as the steep drop in Y at the core–IR boundary (Fig. 11f), are typical of low-Ca metapelites (Pyle & Spear, 1999). These observations indicate that during the growth of the garnet core, its Y content was buffered by xenotime, which was continuously consumed until it was no longer available, at which point the Y content in garnet decreases abruptly (see Pyle & Spear; 1999; Spear & Pyle, 2010).

Tourmaline

At the boundary between the IR and OR of tourmaline, the compositional profiles display abrupt changes in several components, including LREE, Zn, and several of the major elements (Fig. 9). This compositional discontinuity could again be due to several mechanisms, as discussed above for garnet. Because the OR of tourmaline and staurolite formed contemporaneously (after D_3; Fig. 4), it is most likely that some of the changes are due to the competitive co-crystallization of the two minerals. This conclusion is best supported by the precipitous drop in Zn content from ~250 ppm in the tourmaline IR to <50 ppm in the OR (Fig. 9b), which suggests a sudden decrease in Zn availability owing to its incorporation into staurolite (~3000 ppm Zn), a mineral that tends to strongly concentrate Zn in amphibolite-facies metapelites (e.g. Tuisku *et al.*, 1987). This interpretation is also consistent with the

abrupt decrease at the IR–OR boundary of both Al and Fe (Fig. 9a). A drop in the abundance of these elements, albeit at a much smaller scale, is also recognized at the core–IR boundary and may coincide with the growth of the first generation of staurolite (Fig. 4). As seen in Fig. 8, the IR–OR boundary is sutured, indicating that tourmaline was resorbed prior to the growth of the OR. Resorption also affected the euhedral Ca-rich annulus near the outer edge of the IR (Fig. 8b). A second Ca-rich annulus, which is also enriched in LREE, is present in the OR. Even though the LREE concentrations change abruptly at the IR–OR boundary, the absolute values increase by <1·4 ppm (Fig. 9b). This increase is far less than the changes observed in the case of the garnet annulus (Fig. 12b). To produce this small absolute change it is perhaps not necessary to invoke the breakdown of an LREE-enriched mineral or the infiltration of a fluid phase or melt. Rather, we conclude that the Ca- and LREE-rich annulus in the OR of tourmaline was probably formed as a result of the texturally visible post-D_2 resorption and renewed growth after the deformation event D_3 (Fig. 4). Resorption of tourmaline would additionally release B, which was detected only in tourmaline and, to a far lesser extent, muscovite. It could therefore be argued that muscovite growth and tourmaline resorption are intimately linked. Our thermodynamic calculations, however, predict only minor growth of muscovite (followed by some muscovite consumption) between D_2 and D_3 (Fig. 17). Moreover, both model calculations predict the formation of small amounts (5–7 vol. %) of melt during this stage of the metamorphic history (Figs 17 and 18 b). Even though we did not find textural evidence for the presence of melt in the studied rocks, a significant event must have happened between D_2 and D_3, as indicated also by the change in oxygen isotope composition between IR and OR of tourmaline (Table 10). We conclude therefore, that resorption of tourmaline might be due to partial melting, and that the renewed growth of tourmaline after D_3 may have consumed the melt. This mechanism would also provide an explanation for the Ca- and LREE-rich annulus in the OR of tourmaline. This scenario is further consistent with the elevated $\delta^{18}O$ of the OR relative to that of the IR (Table 10): this increase in $\delta^{18}O$ during renewed growth of tourmaline can be interpreted as reflecting the $\delta^{18}O$ of the melt, which is expected to be elevated relative to the restite material because melting also involves consumption of quartz with a high $\delta^{18}O$ (Table 9).

According to thin-section observations and X-ray maps of garnet inclusions in tourmaline, we conclude that the Ca-rich euhedral annulus in the IR of tourmaline formed contemporaneously with the Ca-rich annulus in garnet.

SUMMARY OF RESULTS AND CONCLUDING REMARKS

The data presented here suggest that the distinct trace element zoning observed in porphyroblasts of two phases can be explained in terms of rock-wide events. We conclude that the Ca-rich annuli in both garnet and the IR of tourmaline are due to a major change in EBC, which took place at ~550°C and ~6·4 kbar. This would be consistent with the loss of a relatively high-Ca paragonite and the effectively contemporaneous replacement of allanite (+ apatite) by monazite. Taken together, these reactions liberate Ca, Sr, REE, Y, and B into the EBC, which can then be incorporated into growing garnet, tourmaline (IR), and monazite. Preferential incorporation of the HREE into garnet results in a 'typical' chondrite-normalized REE pattern for the Ca-rich annulus that grew at this point. Subsequent garnet growth from an increasingly HREE-depleted EBC resulted in a distinctive sinusoidal REE pattern in the garnet OR. An earlier phase of progressive fractionation is interpreted for the 'trough zone' inside the Ca-rich annulus, here involving LREE liberation during a lower-temperature monazite-to-allanite reaction. Earlier studies (Janots *et al.*, 2008) suggested that this reaction probably occurred at *c.* 450°C.

Sutured IR–OR boundaries in tourmaline possibly result from its partial resorption by melt, which is predicted in small volumes during the metamorphic thermal peak (between D_2 and D_3). We interpret subsequent tourmaline overgrowth (OR) with substantially lower Zn contents to reflect the competitive co-crystallization of post-D_3 staurolite. Field evidence for the predicted 5–7 vol. % melt is currently lacking in the Campolungo area, but would provide an important additional constraint on the thermal history of this classic metamorphic region.

The example described here further illustrates how careful correlation of major and trace element zoning in coexisting phases can reveal aspects of their complex shared reaction histories. Furthermore, it indicates how this correlation can be coupled with thermodynamic predictions to determine P–T conditions of these reactions, and reveals shortcomings of current simple models for crystal growth. Difficulties in reconciling mineral trace element contents with readily interpreted metamorphic reactions persist, highlighting the need for continued development of conceptual, thermodynamic and kinetic models for processes of grain dissolution, material transport, crystal nucleation and growth during metamorphism.

FUNDING

This work was supported in part by the Swiss National Science Foundation [grants 8220-037190, and 2124-42′200.94 (PROFIL-award), both to R.G.]. We are grateful to the Wissenschaftliche Gesellschaft Freiburg and

to the Rinne-Stiftung for covering some of the travel costs between Freiburg and Washington, DC.

SUPPLEMENTARY DATA

Supplementary data for this paper are available at *Journal of Petrology* online.

ACKNOWLEDGEMENTS

We thank Thomas Jauss for drafting the tectonic map and for his help with other figures. Dr Hiltrud Müller-Sigmund (Freiburg), Carl Hager (Purdue University) and Chris Hadidiacos (Washington) are thanked for their invaluable help with the investigations at the various microprobes. We also thank Steve Shirey (Carnegie Institution of Washington) for drawing our attention to the sinusoidal REE patterns of garnets in some mantle rocks. This paper benefited substantially from the invaluable comments by William Carlson and two anonymous reviewers, as well as from very helpful suggestions by Jörg Hermann.

REFERENCES

Allègre, C. J., Albarède, F., Grünenfelder, M. & Köppel, V. (1974). $^{238}U/^{206}Pb$–$^{235}U/^{207}Pb$–$^{232}Th/^{208}Pb$ zircon geochronology in Alpine and non-Alpine environment. *Contributions to Mineralogy and Petrology* **43**, 163–194.

Anders, E. & Grevesse, N. (1989). Abundances of the elements: meteoric and solar. *Geochimica et Cosmochimica Acta* **53**, 197–214.

Antognini, M. & Bianconi, F. (2007). Agli albori della geologia in Ticino: Déodat de Dolomieu e Carlos de Gimbernat in visita alla regione del Campolungo a inizio Ottocento. *Bolletino della Società Ticinese di Scienze Naturali* **95**, 75–84.

Berger, A. & Mercolli, I. (2006). Tectonic and petrographic map of the Central Lepontine Alps. Map Sheet 43: Sopra Ceneri. Carta geologica speciale, N. 127, 1:100 000. Wabern, Switzerland: Swiss Federal Office of Topography.

Berger, A., Mercolli, I. & Engi, M. (2005). The central Lepontine Alps: notes accompanying the tectonic and petrographic map sheet Sopra Ceneri (1:100 000). *Schweizerische Mineralogische und Petrographische Mitteilungen* **85**, 109–146.

Bhat, M. I. & Ghosh, S. K. (2001). Geochemistry of the 2·51 Ga old Rampur group pelites, western Himalayas: implications for their provenance and weathering. *Precambrian Research* **108**, 1–16.

Bhatia, M. R. & Crook, K. A. W. (1986). Trace element characteristics of graywackes and tectonic setting discrimination of sedimentary basins. *Contributions to Mineralogy and Petrology* **92**, 181–193.

Bianconi, F. (1971). Geologia e petrografia della regione del Campolungo. *Beiträge zur Geologischen Karte der Schweiz*. Bern, Switzerland: Schweizerische Geologische Kommission **Vol. 142**, 238 p.

Bossard, L. (1936). Das Gebiet der penninischen Decken zwischen Ticino und Brenno. In: Niggli, P., Preiswerk, H., Grütter, O., Bossard, L. & Kündig, E. (eds) *Beiträge zur Geologischen Karte der Schweiz* **71**, 31–72.

Bottinga, Y. & Javoy, M. (1973). Comments on oxygen isotope geothermometry. *Earth and Planetary Science Letters* **20**, 250–265.

Burri, T., Berger, A. & Engi, M. (2005). Tertiary migmatites in the Central Alps: Regional distribution, field relations, conditions of formation, and tectonic implications. *Schweizerische Mineralogische und Petrographische Mitteilungen* **85**, 215–232.

Caddick, M. J., Konopásek, J. & Thompson, A. B. (2010). Preservation of garnet growth zoning and the duration of prograde metamorphism. *Journal of Petrology* **51**, 2327–2347.

Carlson, W. D. (1989). The significance of intergranular diffusion to the mechanisms and kinetics of porphyroblast crystallization. *Contributions to Mineralogy and Petrology* **103**, 1–24.

Carlson, W. D. (2006). Rates of Fe, Mg, Mn and Ca diffusion in garnet. *American Mineralogist* **91**, 1–11.

Chernoff, C. B. & Carlson, W. D. (1997). Disequilibrium for Ca during growth of pelitic garnet. *Journal of Metamorphic Geology* **15**, 421–438.

Chernoff, C. B. & Carlson, W. D. (1999). Trace element zoning as a record of chemical disequilibrium during garnet growth. *Geology* **27**, 555–558.

Condie, K. C. (1993). Chemical composition and evolution of the upper continental crust: Contrasting results from surface samples and shales. *Chemical Geology* **104**, 1–37.

Condie, K. C. & Wronkiewicz, D. J. (1990). The Cr/Th ratio in Precambrian pelites from the Kaapvaal Craton as an index of craton evolution. *Earth and Planetary Science Letters* **97**, 256–267.

Condie, K. C., Dengate, J. & Cullers, R. L. (1995). Behavior of rare earth elements in a paleoweathering profile on granodiorites in the Front Range, Colorado, USA. *Geochimica et Cosmochimica Acta* **59**, 279–294.

Connolly, J. A. D. (2005). Computation of phase equilibria by linear programming: a tool for geodynamic modeling and its application to subduction zone decarbonation. *Earth and Planetary Science Letters* **236**, 524–541.

Corrie, S. L. & Kohn, M. J. (2008). Trace-element distributions in silicates during prograde metamorphic reactions: implications for monazite formation. *Journal of Metamorphic Geology* **26**, 451–464.

Cox, C. & Lowe, D. R. (1995). A conceptual review of the regional-scale controls on the composition of clastic sediment and the co-evolution of continental blocks and their sedimentary cover. *Journal of Sedimentary Research* **A65**, 1–12.

Crichton, J. G. & Condie, K. C. (1993). Trace elements as source indicators in cratonic sediments: a case study from the early Proterozoic Libby Creek Group, southwestern Wyoming. *Journal of Geology* **101**, 319–332.

Cullers, R. L. (1994*a*). The chemical signature of source rocks in size fractions of Holocene stream sediment derived from metamorphic rocks in the Wet Mountains region, USA. *Chemical Geology* **113**, 327–343.

Cullers, R. L. (1994*b*). The controls on the major and trace element variation of shales, siltstones, and sandstones of Pennsylvanian–Permian age from uplifted continental blocks in Colorado to platform sediment in Kansas, USA. *Geochimica et Cosmochimica Acta* **58**, 4955–4972.

Cullers, R. L. (2000). The geochemistry of shales, siltsones, and sandstones of Pennsylvanian–Permian age, Colorado, USA: implications for provenance and metamorphic studies. *Lithos* **51**, 181–203.

Cullers, R. L. & Podkovyrov, V. N. (2000). Geochemistry of the Mesoproterozoic Lakhanda shales in southeastern Yakutia, Russia: implications for mineralogical and provenance control, and recycling. *Precambrian Research* **104**, 77–93.

Cullers, R. L., Barrett, T., Carlson, R. & Robinson, B. (1987). Rare-earth element and mineralogic changes in Holocene soil and and stream sediment: a case study in the Wet Mountains, Colorado, USA. *Chemical Geology* **63**, 275–297.

Engi, M., Todd, C. S. & Schmatz, D. R. (1995). Tertiary metamorphic conditions in the eastern Lepontine Alps. *Schweizerische Mineralogische und Petrographische Mitteilungen* **75**, 347–369.

Engi, M., Berger, A. & Roselle, G. (2001). Role of the tectonic accretion channel in collisional orogeny. *Geology* **29**, 1143–1146.

Florence, F. P. & Spear, F. S. (1991). Effects of diffusional modification of garnet growth zoning on *P–T* path calculation. *Contributions to Mineralogy and Petrology* **107**, 487–500.

Florence, F. P. & Spear, F. S. (1993). Influences of reaction history and chemical diffusion on *P–T* calculations for staurolite schists from the Littleton Formation, northwestern New Hampshire. *American Mineralogist* **78**, 345–359.

Frey, M. & Ferreiro Mählmann, R. (1999). Alpine metamorphism of the Central Alps. *Schweizerische Mineralogische und Petrographische Mitteilungen* **79**, 135–154.

Galli, A., Mancktelow, N., Reusser, E. & Caddick, M. (2007). Structural geology and petrography of the Naret region (northern Valle Maggia, N. Ticino, Switzerland). *Swiss Journal of Geoscience* **100**, 53–70.

Gieré, R. & Sorensen, S. S. (2004). Allanite and other REE-rich epidote-group minerals. In: Liebscher, A. & Franz, G. (eds) *Epidotes. Mineralogical Society of America and Geochemical Society, Reviews in Mineralogy and Geochemistry* **56**, 431–493.

Goldschmidt, V. M. & Peters, C. L. (1932*a*). Zur Geochemie des Bors. *Nachrichten von der Gesellschaft der Wissenschaften zu Göttingen, Mathematisch-Physikalische Klasse* **25/27**, 402–407.

Goldschmidt, V. M. & Peters, C. L. (1932*b*). Zur Geochemie des Bors II. *Nachrichten von der Gesellschaft der Wissenschaften zu Göttingen, Mathematisch-Physikalische Klasse* **28/31**, 528–545.

Gratz, R. & Heinrich, W. (1997). Monazite–xenotime thermobarometry: experimental calibration of the miscibility gap in the binary system $CePO_4$–YPO_4. *American Mineralogist* **82**, 772–780.

Griffin, W. L., Shee, S. R., Ryan, C. G., Win, T. T. & Wyatt, B. A. (1999). Harzburgite to lherzolite and back again: Metasomatic processes in ultramafic xenoliths from the Wesselton kimberlite, Kimberley, South Africa. *Contributions to Mineralogy and Petrology* **134**, 232–250.

Grujic, D. & Mancktelow, N. (1996). Structure of the northern Maggia and Lebendun nappes, Central Alps, Switzerland. *Eclogae Geologicae Helvetiae* **89**, 461–504.

Grütter, O. & Preiswerk, H. (1936). Das Gebiet der penninischen Decken östlich des Brenno. In: Niggli, P., Preiswerk, H., Grütter, O., Bossard, L. & Kündig, E. (eds) *Beiträge zur Geologischen Karte der Schweiz* **71**, 73–88.

Gübelin, E. (1939). Die Mineralien im Dolomit von Campolungo (Tessin). *Schweizerische Mineralogische und Petrographische Mitteilungen* **19**, 325–442.

Harder, H. (1970). Boron content of sediments as a tool in facies analysis. *Sedimentary Geology* **4**, 153–175.

Hawthorne, F. C. (1995). Light lithophile elements in metamorphic rock-forming minerals. *European Journal of Mineralogy* **7**, 607–622.

Henry, D. J. & Dutrow, B. L. (1990). Ca substitution in Li-poor aluminous tourmaline. *Canadian Mineralogist* **28**, 111–124.

Henry, D. J. & Dutrow, B. L. (1996). Metamorphic tourmaline and its petrologic applications. In: Grew, E. S. & Anowitz, L. M. (eds) *Boron: Mineralogy, Petrology and Geochemistry. Mineralogial Society of America, Reviews in Mineralogy* **33**, 503–557.

Henry, D. J., Novák, M., Hawthorne, F. C., Ertl, A., Dutrow, B. L., Uher, P. & Pezzotta, F. (2011). Nomenclature of the tourmaline-supergroup minerals. *American Mineralogist* **96**, 895–913.

Herron, M. M. (1988). Geochemical classification of terrigenous sands and shales from core or log data. *Journal of Sedimentary Petrology* **58**, 820–829.

Hickmott, D. D. & Shimizu, N. (1990). Trace element zoning in garnet from the Kwoiek Area, British Columbia: disequilibrium partitioning during garnet growth? *Contributions to Mineralogy and Petrology* **104**, 619–630.

Hickmott, D. & Spear, F. S. (1992). Major- and trace-element zoning in garnets from calcareous pelites in the NW Shelburne Falls Quadrangle, Massachusetts: garnet growth histories in retrograded rocks. *Journal of Petrology* **33**, 965–1005.

Hickmott, D. D., Shimizu, N., Spear, F. S. & Selverstone, J. (1987). Trace-element zoning in a metamorphic garnet. *Geology* **15**, 573–576.

Hickmott, D. D., Sorensen, S. S. & Rogers, P. S. Z. (1992). Metasomatism in a subduction complex: Constraints from microanalysis of trace elements in minerals from garnet amphibolite from the Catalina Schist. *Geology* **20**, 347–350.

Hoal, K. E. O., Hoal, B. G., Erlank, A. J. & Shimizu, N. (1994). Metasomatism of the mantle lithosphere recorded by rare earth elements in garnets. *Earth and Planetary Science Letters* **126**, 303–313.

Hoernes, S. & Friedrichsen, H. (1980). Oxygen and hydrogen isotopic composition of Alpine and pre-Alpine minerals of the Swiss Central Alps. *Contributions to Mineralogy and Petrology* **72**, 19–32.

Hoffbauer, R., Hoernes, S. & Foirentini, E. (1994). Oxygen isotope thermometry based on a refined increment method and its application to granulite-grade rocks from Sri Lanka. *Precambrian Research* **66**, 199–220.

Holland, T. J. B. & Powell, R. (1998). An internally consistent thermodynamic data set for phases of petrological interest. *Journal of Metamorphic Geology* **16**, 309–344.

Janots, E., Engi, M., Berger, A., Allaz, J., Schwarz, J.-O. & Spandler, C. (2008). Prograde metamorphic sequence of REE minerals in pelitic rocks of the Central Alps: implications for allanite–monazite–xenotime phase relations from 250 to 610°C. *Journal of Metamorphic Geology* **26**, 509–526.

Janots, E., Berger, A. & Engi, M. (2011). Physico-chemical control on the REE minerals in chloritoid-grade metasediments from a single outcrop (Central Alps, Switzerland). *Lithos* **121**, 1–11.

Javoy, M. (1977). Stable isotopes and geothermometry. *Journal of the Geological Society of London* **133**, 609–636.

Klapper, D. (2008). Petrographie von Metasedimenten in den Zentralalpen. B.Sc. Research Thesis, Albert-Ludwigs-Universität Freiburg.

Konrad-Schmolke, M., Zack, T., O'Brien, P. J. & Jacob, D. E. (2008). Combined thermodynamic and rare earth element modelling of garnet growth during subduction: Examples from ultrahigh-presssure eclogite of the Western Gneiss Region, Norway. *Earth and Planetary Science Letters* **272**, 488–498.

Köppel, V. (1993). The Lepontine area, a geochronological summary. In: von Raumer, J. F. & Neubauer, F. (eds) *Pre-Mesozoic Geology in the Alps*. Springer: Berlin, pp. 345–348.

Köppel, V., Günthert, A. & Grünenfelder, M. (1981). Patterns of U–Pb zircon and monazite ages in polymetamorphic units of the Swiss Alps. *Schweizerische Mineralogische und Petrographische Mitteilungen* **61**, 97–119.

Kotzer, T. G., Kyser, T. K., King, R. W. & Kerrich, R. (1993). An empirical oxygen- and hydrogen-isotope geothermometer for quartz-tourmaline and tourmaline-water. *Geochimica et Cosmochimica Acta* **57**, 3421–3426.

Lanzirotti, A. (1995). Yttrium zoning in metamorphic garnets. *Geochimica et Cosmochimica Acta* **59**, 4105–4110.

Leeman, W. P. & Sisson, V. B. (1996). Geochemistry of boron and its implications for crustal and mantle processes. In: Grew, E. S. & Anovitz, I. M. (eds) *Boron: Mineralogy, Petrology and Geochemistry. Mineralogical Society of America, Reviews in Mineralogy* **33**, 645–707.

Maxelon, M. & Mancktelow, N. S. (2005). Three-dimensional geometry and tectonostratigraphy of the Pennine zone, central Alps, Switzerland and northern Italy. *Earth-Science Reviews* **71**, 171–227.

McLennan, S. M. (2001). Relationship between the trace element composition of sedimentary rocks and upper continental crust. *Geochemistry, Geophysics, Geosystems* **2**, paper number 2000GC000109.

Mercolli, I. (1982). Le inclusioni fluide nei noduli di quarzo dei marmi dolomitici della regione del Campolungo (Ticino). *Schweizerische Mineralogische und Petrographische Mitteilungen* **62**, 245–312.

Mercolli, I., Skippen, G. & Trommsdorff, V. (1987). The tremolite veins of Campolungo and their genesis. *Schweizerische Mineralogische und Petrographische Mitteilungen* **67**, 75–84.

Mongelli, G., Cullers, R. L. & Muelheisen, S. (1996). Geochemistry of Late Cretaceous–Oligocenic shales from the Varicolori Formation, southern Apennines, Italy: implications for mineralogical, grain-size control and provenance. *European Journal of Mineralogy* **8**, 733–754.

Nesbitt, H. W., Young, G. M., McLennan, S. M. & Keays, R. R. (1996). Effect of chemical weathering and sorting on the petrogenesis of siliciclastic sediments, with implications for provenance studies. *Journal of Geology* **104**, 525–542.

Nyakairu, G. W. A. & Koeberl, C. (2001). Mineralogical and chemical composition and distribution of rare earth elements in clay-rich sediments from central Uganda. *Geochemical Journal* **35**, 13–28.

Pouchou, J. L. & Pichoir, F. (1984). Un nouveau modèle de calcul pour la microanalyse quantitative par spectrométrie de rayons X. Partie I: Application à l'analyse d'échantillons homogènes. *Recherches Aérospatiales* **1984-3**, 167–192.

Preiswerk, H. (1919). Die überkippte Tauchfalte am Campolungopass und ihre frühen Deutungen. *Vierteljahresschrift der Naturforschenden Gesellschaft Zürich* **64**, 1–15.

Pyle, J. M. & Spear, F. S. (1999). Yttrium zoning in garnet: coupling of major and accessory phases during metamorphic reactions. *Geological Materials Research* **1**, 1–49.

Richter, R. & Hoernes, S. (1988). The application of the increment method in comparison with experimentally derived and calculated O-isotope fractionations. *Chemie der Erde* **48**, 1–18.

Rosenbaum, J. M. & Mattey, D. (1995). Equilibrium garnet-calcite oxygen isotope fractionation. *Geochimica et Cosmochimica Acta* **59**, 2839–2842.

Rosenfeld, J. N. (1969). Stress effects around quartz inclusions in almandine and piezothermometry of coexisting aluminium silicates. *American Journal of Science* **267**, 317–351.

Roser, B. P. & Korsch, R. J. (1986). Determination of tectonic setting of sandstone–mudstone suites using SiO_2 content and K_2O/Na_2O ratio. *Journal of Geology* **94**, 635–650.

Roser, B. P. & Korsch, R. J. (1988). Provenance signatures of sandstone–mudstone suites determined using discriminant function analysis of major-element data. *Chemical Geology* **67**, 119–139.

Roser, B. P., Cooper, R. A., Nathan, S. & Tulloch, A. J. (1996). Reconnaissance sandstone geochemistry, provenance, and tectonic setting of the lower Paleozoic terranes of the West Coast and Nelson, New Zealand. *New Zealand Journal of Geology and Geophysics* **39**, 1–16.

Rütti, R., Maxelon, M. & Mancktelow, N. S. (2005). Structure and kinematics of the northern Simano Nappe, Central Alps, Switzerland. *Eclogae Geologicae Helvetiae* **98**, 63–81.

Saleemi, A. A. & Ahmed, Z. (2000). Mineral and chemical composition of Karak mudstone, Kohat Plateau, Pakistan: implications for smectite-illitization and provenance. *Sedimentary Geology* **130**, 229–247.

Schmid, S. M., Fügenschuh, B., Kissling, E. & Schuster, R. (2004). Tectonic map and overall architecture of the Alpine orogen. *Eclogae Geologicae Helvetiae* **97**, 93–117.

Schwandt, C. S., Papike, J. J. & Shearer, C. K. (1996). Trace element zoning in pelitic garnet of the Black Hills, South Dakota. *American Mineralogist* **81**, 1195–1207.

Sektion Geologische Landesaufnahme (SGL). (2005). Tektonische Karte der Schweiz, 1:500 000. Bern-Ittigen: Bundesamt für Wasser und Geologie.

Shao, L., Stattegger, K. & Garbe-Schoenberg, C.-D. (2001). Sandstone petrology and geochemistry of the Turpan basin (NW China): implications for the tectonic evolution of a continental basin. *Journal of Sedimentary Research* **71**, 37–49.

Sharp, Z. D. (1990). A laser-based microanalytical method for the *in situ* determination of oxygen isotope ratios of silicates and oxides. *Geochimica et Cosmochimica Acta* **54**, 1353–1357.

Sharp, Z. D. (1995). Oxygen isotope geochemistry of the Al_2SiO_5 polymorphs. *American Journal of Science* **295**, 1058–1076.

Shimizu, N. (1975). Rare earth elements in garnets and clinopyroxenes from garnet lherzolite nodules in kimberlites. *Earth and Planetary Science Letters* **25**, 26–32.

Shimizu, N. & Richardson, S. H. (1987). Trace element abundance patterns of garnet inclusions in peridotite-suite diamonds. *Geochimica et Cosmochimica Acta* **51**, 755–758.

Skora, S., Baumgartner, L. P., Mahlen, N. J., Johnson, C. M., Pilet, S. & Hellebrand, E. (2006). Diffusion-limited REE uptake by eclogite garnets and its consequences for Lu–Hf and Sm–Nd geochronology. *Contributions to Mineralogy and Petrology* **152**, 703–720.

Slack, J. F. & Stevens, B. P. J. (1994). Clastic metasediments of the Early Proterozoic Broken Hill Group, New South Wales, Australia: Geochemistry, provenance, and metallogenic significance. *Geochimica et Cosmochimica Acta* **58**, 3633–3652.

Smith, H. A. & Barreiro, B. (1990). Monazite U–Pb dating of staurolite grade metamorphism in pelitic schists. *Contributions to Mineralogy and Petrology* **105**, 602–615.

Spear, F. S. (1988). Metamorphic fractional crystallization and internal metasomatism by diffusional homogenization of zoned garnets. *Contributions to Mineralogy and Petrology* **99**, 507–517.

Spear, F. S. & Kohn, M. J. (1996). Trace element zoning in garnet as a monitor of crustal melting. *Geology* **24**, 1099–1102.

Spear, F. S. & Pyle, J. M. (2010). Theoretical modeling of monazite growth in a low-Ca metapelite. *Chemical Geology* **273**, 111–119.

Spear, F. S., Hickmott, D., Crowley, P. & Hodges, K. V. (1984). *P–T* paths from garnet zoning: a new technique for deciphering tectonic processes in crystalline terrains. *Geology* **12**, 87–90.

Sperlich, R., Gieré, R. & Frey, M. (1996). Evolution of compositional polarity and zoning in tourmaline during prograde metamorphism of sedimentary rocks in the Swiss Central Alps. *American Mineralogist* **81**, 1222–1236.

Stachel, T., Viljoen, K. S., Brey, G. & Harris, J. W. (1998). Metasomatic processes in lherzolitic and harzburgitic domains of diamondiferous lithospheric mantle: REE in garnets from xenoliths and inclusions in diamonds. *Earth and Planetary Science Letters* **159**, 1–12.

Stampfli, G. M. (2000). Tethyan oceans. In: Bozkurt, E., Winchester, J. A. & Piper, J. D. A. (eds) *Tectonics and Magmatism in Turkey and the Surrounding Area. Geological Society, London, Special Publications* **173**, 1–23.

Stampfli, G. M., Mosar, J., Favre, P., Pillevuit, A. & Vannay, J.-C. (2001). Permo-Mesozoic evolution of the western Tethys realm: the Neo-Tethys East Mediterranean Basin connection. In: Ziegler, P. A., Cavazza, W., Robertson, A. H. F. & Crasquin-Soleau, S. (eds) *Peri-Tethyan Rift/Wrench Basins and Passive Margins. Peri-Tethys Memoir* **6**, 51–108.

Stüwe, K. (1997). Effective bulk composition changes due to cooling: a model predicting complexities in retrograde reaction textures. *Contributions to Mineralogy and Petrology* **129**, 43–52.

Taylor, L. A., Anand, M., Promprated, P., Floss, C. & Sobolev, N. V. (2003). The significance of mineral inclusions in large diamonds from Yakutia, Russia. *American Mineralogist* **88**, 912–920.

Taylor, S. R. & McLennan, S. M. (1985). *The Continental Crust: its Composition and Evolution*. Oxford: Blackwell.

Teng, F. Z., McDonough, W. F., Rudnick, R. L., Dalpé, C., Tomascak, P. B., Chappell, B. W. & Gao, S. (2004). Lithium isotopic composition and concentration of the upper continental crust. *Geochimica et Cosmochimica Acta* **68**, 4167–4178.

Todd, C. S. & Engi, M. (1997). Metamorphic field gradients in the Central Alps. *Journal of Metamorphic Geology* **15**, 513–530.

Trümpy, R. (1980). *Geology of Switzerland. A Guide Book. Part A: An Outline of the Geology of Switzerland*. Basel: Wepf.

Tuisku, P., Ruosresuo, P. & Häkkinen, A.-M. (1987). The metamorphic behaviour and petrogenetic significance of zinc in amphibolite facies, staurolite-bearing mica schists, Puolankajärvi Formation, Central Finland. *Geochimica et Cosmochimica Acta* **51**, 1639–1650.

Turekian, K. K. & Wedepohl, K. H. (1961). Distribution of the elements in some major units of the Earth's crust. *Geological Society of America Bulletin* **72**, 175–192.

Valley, J. W., Kitchen, N., Kohn, M. J., Niendorf, C. R. & Spicuzza, M. J. (1995). UWG-2, a garnet standard for oxygen isotope ratios: strategies for high precision and accuracy with laser heating. *Geochimica et Cosmochimica Acta* **59**, 5223–5231.

Wing, B. A., Ferry, J. M. & Harrison, T. M. (2003). Prograde destruction and formation of monazite and allanite during contact and regional metamorphism of pelites: petrology and geochronology. *Contributions to Mineralogy and Petrology* **145**, 228–250.

Wronkiewicz, D. J. & Condie, K. C. (1987). Geochemistry of Archean shales from the Witwatersrand Supergroup, South Africa: Source-area weathering and provenance. *Geochimica et Cosmochimica Acta* **51**, 2401–2416.

Yang, P. & Pattison, D. (2006). Genesis of monazite and Y zoning in garnet from the Black Hills, South Dakota. *Lithos* **88**, 233–253.

Yang, P. & Rivers, T. (2002). The origin of Mn and Y annuli in garnet and the thermal dependence of P in garnet and Y in apatite in calc-pelite and pelite, Gagnon terrane, western Labrador. *Geological Materials Research* **4**, 1–35.

Zhang, H.-F., Menzies, M. A. & Mattey, D. (2003). Mixed mantle provenance: diverse garnet compositions in polymict peridotites, Kaapvaal craton, South Africa. *Earth and Planetary Science Letters* **216**, 329–346.

Zheng, Y.-F. (1993*a*). Calculation of oxygen isotope fractionation in anhydrous silicate minerals. *Geochimica et Cosmochimica Acta* **57**, 1079–1091.

Zheng, Y.-F. (1993*b*). Calculation of oxygen isotope fractionation in hydroxyl-bearing silicates. *Earth and Planetary Science Letters* **120**, 247–263.

APPENDIX: ANALYTICAL PROCEDURES

Bulk-rock analysis

Samples were sawn into small pieces (~1 cm^3) using a diamond saw and then milled (the Cr-steel mill may have led to enhanced apparent Cr and Fe contents). The total amount of rock powder varied between 570 g (sample Leit 300a) and 1290 g (sample Leit 900). From the homogenized powders, one or more aliquots were taken and sent to a commercial laboratory for analysis (SGS Canada Inc.). Several analytical methods (see Table 1) were used to determine the bulk chemical composition of the metapelites. Analytical quality was controlled by duplicate analyses and repeat analysis of various rock standards.

Electron probe microanalysis (EPMA)

The composition of both major and accessory minerals (Tables 2, 4, 6 and 8) was determined by EPMA, using a CAMECA SX-50 instrument (at Purdue University) and a JEOL JXA-8800L Superprobe (at the Carnegie Institution of Washington), equipped with four and five wavelength-dispersive spectrometers, respectively. An acceleration potential of 15 kV and beam current of 20–40 nA (major elements) or 100 nA (trace elements in garnet, staurolite, monazite and xenotime) were used. The same polished thin sections studied with the optical microscope were used for EPMA, following addition of a 20 nm carbon coat. Minerals and synthetic oxides were used as standards. On-peak acquisition time was 20 s for major elements and 60–100 s for minor and trace elements, with half as long spent acquiring at background positions on either side of each peak. Raw data were corrected on-line with the PAP correction procedure (Pouchou & Pichoir, 1984).

Element distribution maps were generated at 15 kV and 150 nA (tourmaline), 90 nA (garnet, major elements), or 200 nA (garnet, Y maps). All data were collected in wavelength-dispersive mode. Dwell time was 130 ms per pixel for both tourmaline and garnet.

Laser ablation inductively coupled plasma mass spectrometry (LA-ICP-MS)

The trace element composition of several major and accessory minerals was determined *in situ* by LA-ICP-MS at the Laboratory for Inorganic Chemistry at ETH Zürich. An ELAN 6100 DRC (Perkin–Elmer/Sciex) was coupled to a GeoLas 193 nm ArF excimer laser, which was operated at a frequency of 10 Hz and an energy ranging between 140 and 190 mJ. The NIST 610 synthetic silicate glass was used as an external standard for all analytical runs. All analyses were obtained from thin section Leit 8 g (from sample Leit 8).

Oxygen isotope analysis

One sample (Leit 8), which had been characterized in terms of both its bulk chemical composition and mineral composition, was also selected for oxygen isotope analysis. The sample was crushed and sieved, and pure mineral separates were obtained by using gravimetric and magnetic methods, and final hand-picking from the 160 μm to 200 μm size range. Several zoned tourmaline crystals were sectioned perpendicular to their *c*-axis to

produce double-sided polished thick sections. Chips of core, inner rim and outer rim material were cut out of the optically zoned crystal slices. This procedure was performed with a metal scalpel under a binocular microscope operated with transmitted light. The chips were crushed and any visible inclusions of other phases removed by hand-picking.

Oxygen was extracted from the mineral separates and tourmaline chips with a CO_2 laser fluorination system at the Geophysical Laboratory similar to that of Sharp (1990), but differing in that the O_2 gas is analyzed directly in the mass spectrometer without conversion to CO_2. Samples (1–3 mg) were reacted with BrF_5, and the liberated O_2 gas was purified in several steps before being collected on a molecular sieve. The gas was transferred into the bellows and analyzed by a Thermo-Fisher MAT 252 mass spectrometer. The analyses were compared with the UWG-2 garnet standard (Valley *et al.*, 1995), and all data are reported in delta notation relative to VSMOW. Replicate analyses of standards and samples show that reproducibility is generally 0·1–0·2‰. The accuracy of the measured isotope ratios may be assessed by comparing the results of this study for quartz ($\delta^{18}O = 8{\cdot}86‰$) with those obtained by conventional fluorination for aliquots of the same samples ($\delta^{18}O = 8{\cdot}93‰$, Geochron Laboratories).